Phase Stability and Mechanical Behavior of BCC Refractory High Entropy Alloys

A Dissertation Presented for the

Doctor of Philosophy

Degree

The University of Tennessee, Knoxville

Jeffrey M. Brookins

May 2024

Acknowledgements

The completion of this manuscript represents significantly more than years of work. Instead, it represents the importance of family, friends, and coworkers. The people listed below have had an enormous impact on my UT-Knoxville experience, and even that is putting it lightly.

First, I am deeply indebted to my advisor, Easo George, in a manner that I can only hope to repay by mentoring future students. His genuine care was immediately evident from our first real interaction: waiting for me to tour the UTK and ORNL campuses and ensuring that I enjoyed the area, before formally extending an offer to come study. Without him, this would have, quite literally, been impossible.

My committee, Veerle Keppens, Claudia Rawn, and Ying Yang: thank you for your time and dedication to raising the next generation of researchers. Your commitment to overseeing a PhD student throughout his early career is appreciated, and your individual styles of questioning will professionally remain on my mind for many years.

On more than one occasion, I have recognized that there are many people smarter than I am and this was especially evident when it came to specialized equipment. Michael Koehler provided not only excellent advice and direction, but was also a source of levity during my 6/10/18hr x-ray diffraction binges. Resonant ultrasound spectroscopy (RUS) was a technique that I had never learned, but under the tutelage of Brianna Musico, Candice Kinsler-Fedon, and Rubayet Tanveer; I was taught the intricacies of precise measurements at room- and cryogenic-temperatures.

I've heard over the years that you can pick your friends, but you can't pick your family. Jack Carpenter, Josh Cicotte, Ian Stinson, and Dustin Heidel have proven that wrong. Over the years of sharing an office, lab, pot(s) of coffee, or questionably cooked ramen; a bond has been forged that will truly withstand the test of time.

Speaking of family, without the support of my mother, Christine Brookins, or sister, Brigeth Brookins; these years would have been much different, as their phone calls and curious questions were always a bright spot in the day. Unfortunately, my late father, Clarence Brookins won't be able to celebrate with us; but without him and his stash of engineering books scattered throughout the house, my path in life would have been much different and that's a memory I'll always carry with me.

For all of my unlisted friends, you'll understand my text limitations in a few months, as you prepare for your defenses. Fortunately, you already know that my home is always open for you: there's plenty of food for dinner.

Last, but certainly not least, is my wonderful partner: Jennifer Dunn. Over the past ~11 years, her unwavering support has been a bedrock in my life. From our first date jumping out of a perfectly good airplane at 18,000ft, to our shared graduate school experiences, to moving across the country several times; she has always been there.

This research was supported by the UT-ORNL Governor's Chair program. Experiments at ORNL were sponsored by the U.S. Department of Energy, Basic Energy Sciences, Materials Sciences and Engineering Division.

Abstract

High entropy alloys (HEAs) have become a popular framework for alloy design, due to the multitude of compositional knobs that can be adjusted; in contrast to the dilute solutions of previous generations. Refractory HEAs (RHEAs) have garnered interest due to their potential usage as new structural materials for high-temperature applications, as their high melting temperatures exceed those of nickel-based superalloys. Here, body-centered cubic RHEAs are explored using model alloy systems based on Ti-Zr-Nb-Hf-Ta and V-Nb-Mo-Ta-W.

The first work looks at the equiatomic TiZrNbHfTa and VNbMoTaW, and all the equiatomic quaternaries, ternaries, and binaries that can be formed from their constituent elements, to assess compositional effects on single-phase stability. Three constituent elements in TiZrNbHfTa (Ti, Zr, Hf) have the HCP crystal structure at room temperature while the remaining two (Nb, Ta) are BCC. In contrast, all the elements in VNbMoTaW have the BCC structure. Phase stability was assessed after isothermal aging at 800°C, 1000°C, and 1200°C for times of 72 to 7200 h. It was found that some compositions have an island of instability at lower temperatures, but most can be single-phase above that. From these results, it appears that design of single-phase alloys should take into account the crystal structures of the elements and the mutual solubilities of their constituent binary pairs.

The second work looks at a pseudobinary (TiZrHf) – (NbTa) system, designated as (HCP_{eq}) – (BCC_{eq}), where HCP_{eq} is the sum of the concentrations of elements with HCP crystal structure at room temperature and BCC_{eq} that of the BCC elements. Five

compositions ranging from 0.0 – 0.4 BCC_{eq} were investigated. Three compositions (0.2/0.3/0.4 BCC_{eq}) were able to be cold-rolled to 80% reduction, recrystallized, and tensile-tested. They showed that as the BCC_{eq} increased, so did the yield stress and uniform elongation. This increase in yield strength is attributed to increasing shear modulus with increasing BCC_{eq}.

The final work looks at off-equiatomic TiZrNbHfTa derivatives: a Ti-rich and Zr-rich composition. Mechanical testing was performed at 293 K and 77 K. While the Ti-rich alloy exhibited cryogenic ductility, the Zr-rich elongation was reduced by ~30% and the equiatomic composition was embrittled at 77 K.

Table of Contents

List of Tables

List of Figures

Introduction

Historically, metallic alloy design has been based around dilute additions or subtractions to alloys consisting of a principal element, in order to find new alloys with desirable properties. The addition of tin or arsenic to copper formed a harder bronze and led to the eponymous historic period known as the Bronze Age; the removal of oxygen from copper yielded higher conductivity than commercially pure copper wire, at the cost of tensile strength; and the addition of copper to gold created a rose-colored hue [1-3]. Early research into high entropy alloys (HEAs) had shifted the classical standard of a single principal element with dilute additions, into alloys containing approximately five co-principal elements with equiatomic ratios [4]. However, removing the restriction of equivalent ratios has significantly increased the available design space, allowing for the tuning of specific deformation mechanisms, such as transformation-induced plasticity (TRIP) or twinning-induced plasticity (TWIP) [5-8]. Consequently, the visualization of these alloys has expanded from traditional binary and ternary phase diagrams, to multinary projections either as isopleths or tabulated databases from thermodynamic calculations [5, 9, 10]. As the HEA methodology has advanced, authors have introduced various terms to describe the composition and elemental components: complex concentrated alloys, multi-principal element alloys, high and medium entropy alloys, and baseless alloys [5, 11]. Within this work, high entropy alloys will encompass all these terms, with nonequiatomic compositions represented as atomic percent, unless otherwise noted.

Initially, the first major high entropy alloys were derived from the Cantor alloy CrMnFeCoNi, an equiatomic FCC solid solution alloy [12]. Originally, Yeh et al. believed that these FCC alloys were stabilized by their inherent configurational entropy, suppressing intermetallic formation [4]. Work done by Otto et al. tested the high entropy hypothesis, by substituting comparable elements into the quinary Cantor alloy (Ti for Co, V for Fe, etc.), concluding that enthalpy and non-configurational entropy have more significant effects on the phase stability [13]. The effect of configurational entropy on mechanical properties was explored by Wu et al. in solid solution HEAs, finding no correlation between the number of constituent elements and strength [14]. Various models have been used to predict the single-phase stability of HEAs including the Hume-Rothery rules, which uses simple elemental descriptors, and the CALPHAD method, requiring a reliable database of thermodynamic information [15-21]. In order to understand the individual impact of specific elements in equiatomic alloys, Chen et al. performed high-throughput calculations using density-functional theory (DFT): calculating over 658,000 quinary alloys and identifying groups of elements that strongly favor solid solution formation [22]. This understanding of phase stability at room- and elevated-temperatures is essential for the design of structural materials for high-temperature applications [23].

While the Cantor alloy is not suitable for high-temperature applications beyond Ni-base superalloys due to its low melting temperature (T_m), some of the most exciting discoveries came from this system [24-28]. High cryogenic toughness in the equiatomic

CrMnFeCoNi and CrCoNi alloys, as well as the off-equiatomic $Cr_{18.4}Fe_{57.6}Co_{12}Ni_{12}$, coming from progressive activation of deformation mechanisms was found by Otto et al., Liu et al., and Zhong et al., respectively [29-31]. Deng et al. used the compositional degrees of freedom to introduce the quaternary $Fe_{40}Mn_{40}Co_{10}Cr_{10}$ composition, which would TWIP during room-temperature deformation [7]. Instead of a single-phase microstructure, Li et al. investigated the $Cr_{10}Mn_xFe_{80-x}Co_{10}$ compositional space, showing that decreasing Mn would lead to TWIP at 40 at% Mn, TRIP at 35 at%, and a dual-phase FCC/HCP microstructure that would TRIP (DP-TRIP) at 30 at% [32]. Inspired by this and other metastable DP-TRIP-HEA work, $Cr_{20}Mn_6Fe_{34}Co_{34}Ni_6$ was presented by Chen et al. which would also TRIP from FCC to HCP, yielding higher strength and ductility over the equiatomic Cantor alloy [33-39]. Due to the vastness of the HEA compositional space, the above work showcases a new design philosophy with regards to phase stability and microstructure which can be applied to higher operating temperature alloys containing the refractory elements [23, 40, 41].

Early refractory high entropy alloys (RHEAs), primarily containing Ti, V, Zr, Nb, Mo, Hf, Ta, or W; such as NbMoTaW and VNbMoTaW were shown to have a single-phase, BCC structure by Senkov et al. [42, 43]. However, they had low compressive strains of 2.1% and 1.7%, respectively [42, 43]. Later, the BCC TiZrNbHfTa composition was shown to be compressible to 50% strain, before reaching geometrical sample constraints, without cracking [43]. Further thermomechanical processing showed that TiZrNbHfTa could be cold worked to 86-89% reduction in thickness without cracking and had a

tensile ductility of 9.7% after recrystallization at 1000°C for 2 hours and 18.5% after recrystallization at 1100°C for 1 hour [44, 45]. The Senkov alloy, TiZrNbHfTa, showed that a refractory BCC alloy could be thermomechanically-processed via room-temperature deformation and recrystallized for a controllable grain size [44, 45]. While the phase stability of the Senkov alloy and derivatives will be discussed with more detail in an upcoming chapter, it is worth briefly mentioning here. The equiatomic quinary alloy decomposes into multiple phases between 500-900°C forming a mix of BCC and HCP structures, which are deleterious to the ductility [43, 45-47]. Increasing the Ti content, while retaining a single-phase BCC after homogenization, has shown to have a similar phase decomposition at the same 500-900°C range in the $Ti_{1.5}ZrNb_{0.5}Hf_{0.5}Ta_{0.5}$ composition [48]. For high-temperature applications, single-phase solid solutions are generally not desirable and there is a robust body of literature that explores the more complicated microstructures that are possible in multi-phase RHEAs which include additional refractory elements; however, these are only included for completeness and will not be discussed further [49-75].

Within this body of work, the Ti-Zr-Nb-Hf-Ta system was chosen as a model alloy system to investigate compositional effects on mechanical behavior, due its room temperature tensile ductility. The other model RHEA system V-Nb-Mo-Ta-W is too brittle to be characterized mechanically. However, it is of interest to compare its phase stability with that of the Ti-Zr-Nb-Hf-Ta system since the former (V-Nb-Mo-Ta-W)

consists of only BCC elements whereas the latter (Ti-Zr-Nb-Hf-Ta) has both BCC and HCP elements.

Chapter 1 Phase Stability of Refractory High Entropy Alloys

This chapter is being prepared for publication in a peer-reviewed journal. JM Brookins performed all of the sample preparation, characterization, analysis, and writing of the first draft. Cecil Carmichael arc-melted and heat-treated all specimens. Ian Stinson sectioned each arc-melted button. EP George conceived and supervised the study.

Introduction

Nickel-based superalloys generally melt around 1400°C and rely on various coatings or cooling methods to operate in the 1400-1600°C range of jet engine inlet temperatures [26-28, 76]. Refractory high entropy alloys (RHEAs) such as VNbMoTaW and TiZrNbHfTa, with estimated melting temperatures (T_m) of 2700°C (rule of mixtures) and 2000°C (CALPHAD calculation), respectively, are being explored as potential replacements for nickel-based superalloys at higher operating temperatures.

Since strength generally decreases past 0.5 T_m, increasing the melting point of an alloy can increase strength at any given operating temperature. However, RHEAs must be investigated for phase stability within the expected exposure temperatures of service, lest their mechanical properties degrade due to undesirable phase transformations. The formation of solid solutions has been rationalized using many different metrics: differences in atomic radii, mixing enthalpy and entropy, elemental electronegativity, and the average valence electron concentration of the composition [77]. It is important to note, that for structural applications at high temperatures, additional phases such as B2, Laves, or other intermetallics would be desirable for strengthening [78].

Investigations in the literature have focused mainly on the TiZrNbHfTa quinary alloy, due to its room-temperature formability and ductile tensile behavior [44, 45]. This alloy undergoes multiple phase transformations at intermediate temperatures of 500-900°C forming BCC1 + BCC2, HCP + BCC1 + BCC2, and HCP + BCC structures [43, 45-47]. Senkov showed that the decomposition from a single BCC phase, into a BCC1+BCC2 two-phase structure greatly degrades the ductility [45].

To date, investigations into the phase stability of the Ti-Zr-Hf-Nb-Ta system have been limited in both composition and temperature range, with most of the work having been done on the equiatomic quinary alloy TiZrHfNbTa. For example, Senkov et al., showed that TiZrNbHfTa has a single-phase BCC structure after 2 hours at 1000°C and 3 hours at 1200°C, but transformed into a BCC1+BCC2 structure with ZrHf-enriched and NbTa-enriched phases after 2 hours at 800°C [43, 45].

Additional work on TiZrNbHfTa by Schuh et al., showed that after high-pressure torsion (HPT) at room temperature, the alloy consisted of a single BCC phase and subsequent annealing for 1 hour at 300°C did not produce a phase transformation [46]. However, after annealing at 500°C for 1 and 100 hours, there was a ZrHf-enriched HCP phase and a NbTa-enriched BCC phase; after annealing at 800°C for 1 hour, an additional ZrHf-enriched BCC phase appeared in addition to the existing 500°C phases; after 1 hour at 900°C, the phases reduced to a BCC1 + BCC2 structure; and finally, after 1 hour at 1100°C, the alloy returned to being single-phase BCC [46].

To avoid any influence from the large grain boundary volume present in the nanocrystalline material produced by HPT, annealing was performed by Chen et al., in the range of 550°C to 1000°C on homogenized, cold-rolled and recrystallized TiZrNbHfTa sheets [47]. After 96 hours at 550°C, there was a NbTa-enriched BCC1 phase, a BCC2 phase, and a ZrHf-enriched HCP phase; after a 700°C anneal, the results were roughly the same as after 550°C, except that there was a reduction of the BCC2 peak intensity; 900°C yielded a NbTa-enriched BCC1 and a BCC2 phase; and after a 1000°C anneal there was only a single BCC phase [47]. In addition to the above 96-hour heat treatments, other anneals included 2.5 hours, 96 hours, and 192 hours at 700°C. As the time increased, the microstructure changed from BCC1 + BCC2 at 2.5 hours, to BCC1+BCC2+HCP after 96 hours and 192 hours [47]. From the above works, it is clear that phase stability depends on both time and temperature, as summarized in Figure 1.1.

Maiti and Steurer annealed the quaternary equiatomic alloy ZrNbHfTa at 1800°C from 6 hours to 192 hours, approximately $0.8T_m$ from the rule of mixtures or $0.9T_m$ from CALPHAD calculations [79]. After 48 hours at 1800°C, powder diffraction showed a single-phase BCC structure; at 96 hours, an HCP peak began to appear and continued to grow at 192 hours [79]. Atom probe tomography showed clustering of Zr and Hf atoms beginning at 6 hours, with co-clustering at 96 hours [79]. Maiti and Steurer also suggested that the HCP phase began to form at areas high in Zr and Hf concentration, and that there was a BCC to BCC1+BCC2 decomposition in the 192 hour samples [79].

A second model RHEA of interest is VNbMoTaW [42]. When compared to a common nickel-based superalloy Haynes 282, and TiZrHfNbTa; VNbMoTaW maintains higher yield strength over a larger range of temperatures, Figure 1.2 [43, 80, 81]. Therefore, VNbMoTaW has the potential of superior high-temperature mechanical properties than TiZrHfNbTa. However, its phase stability has not so far been investigated.

One of the objectives of this study was, therefore, to investigate the phase stability of the VNbMoTaW RHEA and compare it with that of TiZrNbHfTa. A salient difference between these two equiatomic quinaries is that the former consists of elements that are all BCC at room temperature whereas the latter contains both BCC and HCP elements. Consequently, Hume-Rothery rules [15, 16] would favor single-phase BCC stability over a wider range of temperatures in VNbMoTaW than in TiZrNbHfTa. Another objective was to investigate how important a role configurational entropy plays in stabilizing single-phase solid solutions, which was one of the founding principles of the HEA field [4]. To systematically vary the configurational entropy, the constituent elements in the V-Nb-Mo-Ta-W and Ti-Zr-Nb-Hf-Ta alloy systems were systematically decreased by considering all their equiatomic quaternary, ternary, and binary subsystems. The resulting 52 alloys were then annealed for times up to 300 days to promote thermodynamic equilibrium and their microstructures analyzed to determine whether phase decomposition had occurred.

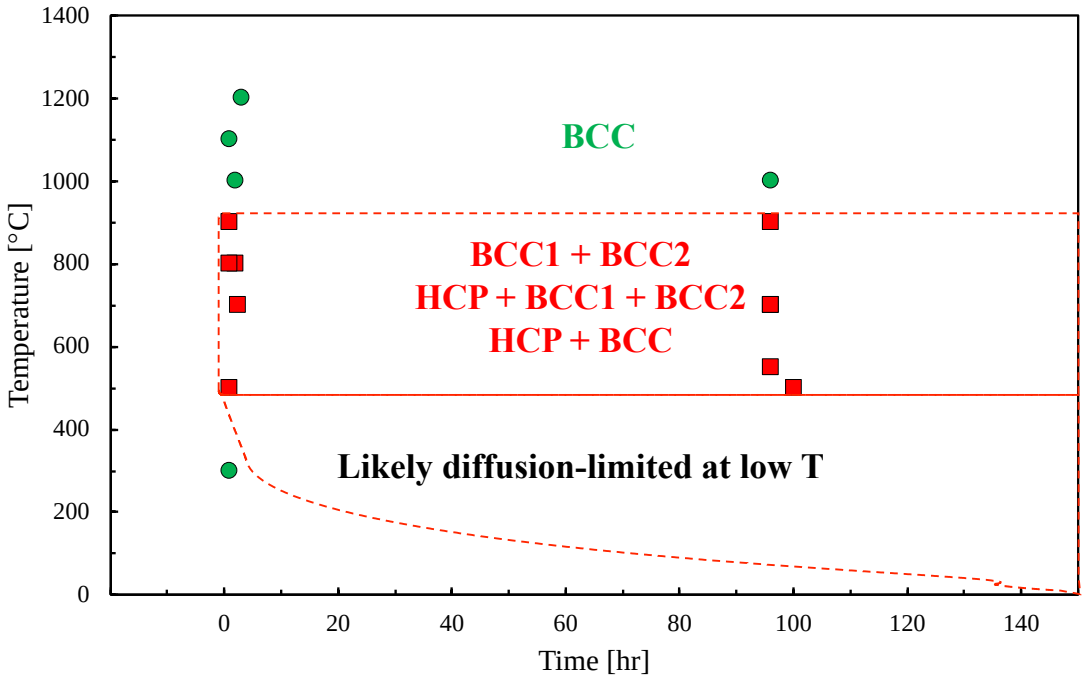

Figure 1.1. At intermediate temperatures, TiZrNbHfTa shows an island of instability: leading to the single-phase BCC decomposing into BCC1, BCC2, and HCP phases [43, 45-47].

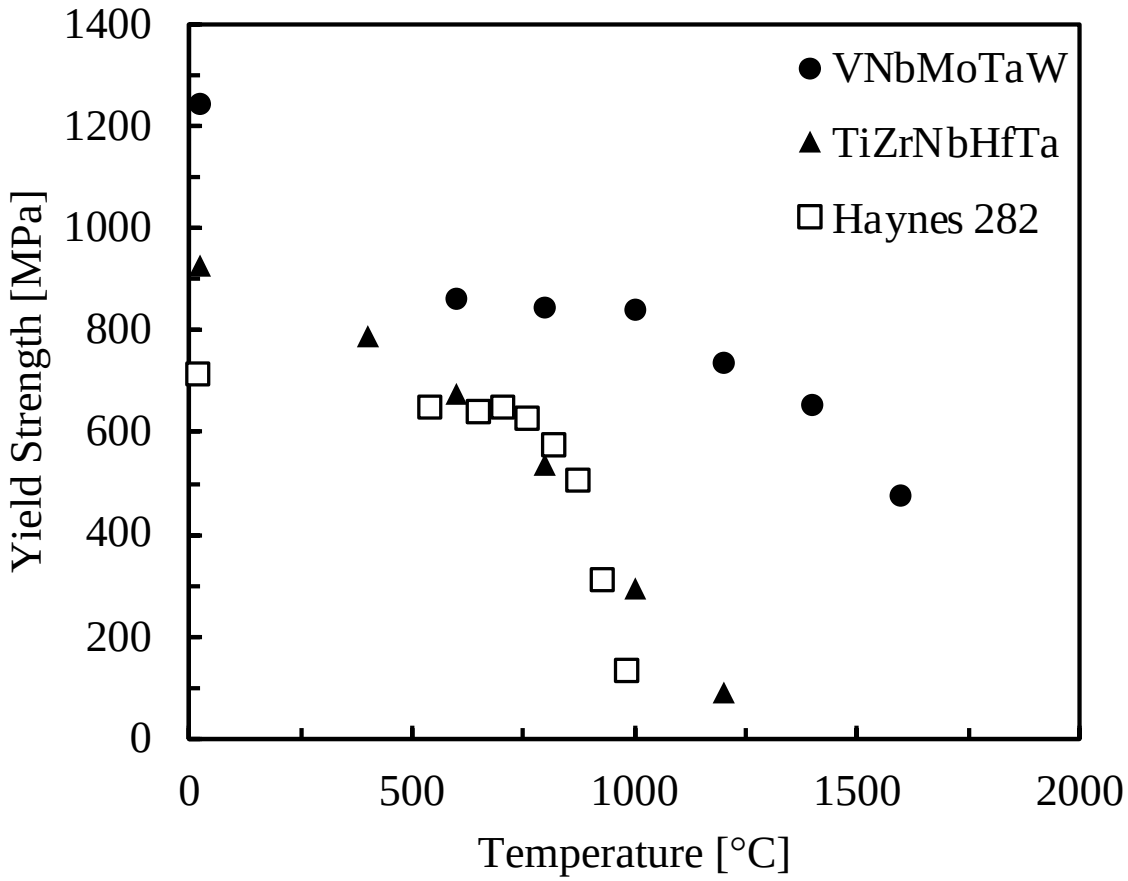

Figure 1.2. Yield strength as a function of temperature for the VNbMoTaW and TiZrNbHfTa RHEAs (compressive) and Haynes 282 nickel-based superalloy (tensile) [43, 80, 81].

Experimental Methods

The equiatomic alloys of the Ti-Zr-Nb-Hf-Ta and V-Nb-Mo-Ta-W systems investigated in the present study are shown in Figure 1.3. Semi-hemispherical buttons of each alloy were produced by arc-melting under an argon atmosphere. Before melting of the investigated alloys, the chamber was evacuated to between 10^{-4} and 10^{-5} Pa, backfilled with argon, and then a small Ti button was melted and solidified to getter any residual oxygen. In order to obtain a homogenous sample, the alloy buttons were flipped and remelted, at least five times.

Wire-EDM was used to cut four slices from near the mid-section of each button and each slice was ground to remove the EDM damage; an example slice is shown in Figure 1.4. These slices were separated into four groups per alloy system: as-cast, 800°C for 7200 hours, 1000°C for 720 hours, and 1200°C for 72 hours. The latter three conditions were chosen to promote phase equilibration at the chosen temperatures. Before encapsulation in quartz for annealing, the samples were homogenized for 48 hours in a vacuum furnace at 1800°C (VNbMoTaW) or 1200°C (TiZrNbHfTa). The samples were then sealed in quartz, after repeated flushing and purging with argon to minimize the amount of residual oxygen and nitrogen, and heat-treated. Following heat-treatment, each quartz capsule was transferred as quickly as possible, within seconds, into a water bath and the capsule immediately broken under water to minimize air contact and maximize the quench rate. Each individual specimen was then mounted in epoxy with a label detailing composition

Ti-Zr-Nb-Hf-Ta			V-Nb-Mo-Ta-W		
Ti-Zr-Hf-Ta Ti-Zr-Nb-Hf	Ti-Zr-Nb-Ta	Ti-Hf-Nb-Ta Zr-Hf-Nb-Ta	V-Nb-Mo-Ta V-Mo-Ta-W	V-Nb-Mo-W	V-Nb-Ta-W Nb-Mo-Ta-W
Ti-Zr-Nb	Ti-Zr-Hf	Ti-Zr-Ta	V-Nb-Mo	V-Nb-Ta	V-Nb-W
Ti-Nb-Hf	Ti-Hf-Ta	Ti-Nb-Ta	V-Mo-Ta	V-Mo-W	V-Ta-W
Zr-Hf-Nb	Zr-Hf-Ta	Zr-Nb-Ta	Nb-Mo-Ta	Nb-Mo-W	Nb-Ta-W
	Nb-Hf-Ta			Mo-Ta-W	
Ti-Zr	Ti-Hf	Ti-Nb	V-Nb	V-Mo	V-Ta
Ti-Ta	Zr-Hf	Zr-Nb	V-W	Nb-Mo	Nb-Ta
Zr-Ta	Nb-Hf	Hf-Ta	Nb-W	Mo-Ta	Mo-W
	Nb-Ta			Ta-W	

HCP **BCC**

Figure 1.3. Equiatomic, lower-order sub-systems of the Ti-Zr-Nb-Hf-Ta and V-Nb-Mo-Ta-W alloy families. Elements having the HCP and BCC structure at room temperature are highlighted in red and green, respectively.

and processing conditions, ground, and polished in steps following standard metallographic practice and ending with 0.05 μm diamond. The final polish ensured a smooth surface for electron microscopy and minimal peak broadening during XRD. Characterization was performed using x-ray diffraction (XRD) for crystal structure determinations and SEM/EDS for compositional analysis, as shown in Figure 1.4.

For XRD, a copper radiation source was used with a spinning stage to include the maximum number of diffracting crystallites. Each measurement had a scan range from 30° to 130°, with a total count time of 30 minutes for each of the alloys in the Ti-Zr-Nb-Hf-Ta system and 15 minutes for the V-Nb-Mo-Ta-W alloys. These parameters were chosen to allow a sufficient number of peaks to be included, while ensuring that a strong enough signal could be seen over the background. Phase fractions were determined by Rietveld refinement using the HighScore software package. Each individual pattern was converted from total counts to relative intensities, by dividing by the maximum intensity of the scan, and each normalized pattern was then identified by its alloy designation and annealing temperature. Due to the large number of XRD plots, they are included in the Appendix, with only selected plots being shown in the main text. For compositional analysis, a TESCAN SEM equipped with an Oxford Instruments EDS system was used at 15 kV for collecting backscattered electron images, as well as line scans, to show microstructural evolution and phase composition. Due to the number of samples being tested, comprehensive data were not collected; instead, the focus was identifying between single- and multi-phase samples.

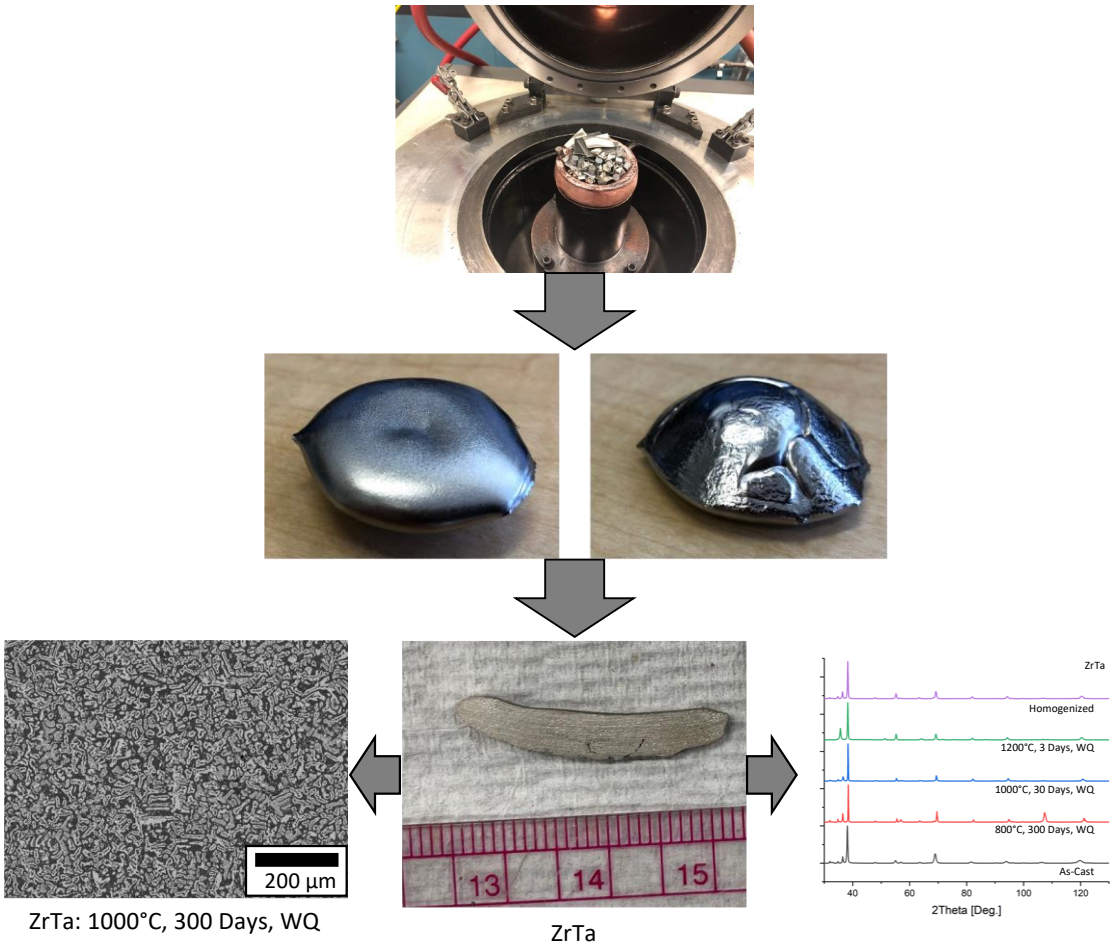

Figure 1.4. Workflow example for the Zr-Ta alloy showing arc-melting (top), the finished button (middle), and characterization of the sliced specimen (bottom, middle): electron backscatter imaging (bottom, left) with line-scan EDS (not shown), and x-ray diffraction patterns (bottom, right) for crystal structure identification.

Results and Discussion

From the overall results shown in Table 1.1 and Table 1.2, certain broad trends are evident. In general, there are more green areas in the V-Nb-Mo-Ta-W system than in the Ti-Zr-Nb-Hf-Ta system, especially after annealing. This indicates that single-phase BCC stability is favored over a broader range of temperatures in the former, which consists of only BCC elements than the latter which has a mix of BCC and HCP elements. However, the large number of results shown in Table 1.1 and Table 1.2 make detailed understanding difficult. Therefore, some simplification is warranted. One such simplification is to take into account only the aged samples and remove the as-cast and the homogenized samples from consideration because the latter two were not quenched rapidly from high temperature calling into question their 'equilibration' condition during continuous cooling. Second, the data can be grouped into binary, ternary, quaternary, and quinary alloys to evaluate the effect of temperature, as shown in Table 1.3. From these reduced data sets two additional trends become clearer. First, at the lowest annealing temperature, there is no correlation between single-phase stability and the number of constituent elements (i.e., configurational entropy). While the increasing insignificance of entropy with decreasing temperature is not surprising, what the present data additionally show is that increasing the configurational entropy does not suppress enthalpic contributions to the total free energy at lower temperatures. The second trend is that, in

Table 1.1. From EDS, the alloys were categorized as single-phase (green) or multiphase (red).

	As-Cast	Homogenized	800°C	1000°C	1200°C
TiZrNbHfTa	Multi	Single	Multi	Single	Single
TiZrNbHf	Single	Single	Single	Single	Single
TiZrHfTa	Multi	Single	Multi	Single	Single
TiZrNbTa	Multi	Single	Multi	Multi	Single
TiNbHfTa	Multi	Single	Single	Single	Single
ZrNbHfTa	Multi	Single	Multi	Multi	Single
TiZrHf	Single	Single	Multi	Single	Single
TiZrNb	Single	Single	Single	Single	Single
TiZrTa	Multi	Multi	Multi	Multi	Single
TiNbHf	Single	Single	Single	Single	Single
TiHfTa	Single	Single	Single	Single	Single
TiNbTa	Multi	Multi	Multi	Multi	Multi
ZrNbHf	Single	Single	Single	Single	Single
ZrHfTa	Single	Multi	Multi	Multi	Multi
ZrNbTa	Multi	Multi	Multi	Multi	Multi
NbHfTa	Multi	Single	Multi	Single	Single
TiZr	Single	Single	Single	Single	Single
TiHf	Single	Single	Multi	Multi	Single
TiNb	Single	Single	Single	Single	Single
TiTa	Multi	Single	Multi	Single	Single
ZrHf	Single	Single	Single	Single	Single
ZrNb	Single	Single	Multi	Single	Single
ZrTa	Multi	Multi	Multi	Multi	Multi
NbHf	Single	Multi	Multi	Multi	Single
HfTa	Single	Multi	Multi	Multi	Multi
NbTa	Multi	Multi	Multi	Multi	Single

	As-Cast	Homogenized	800°C	1000°C	1200°C
VNbMoTaW	Multi	Single	Single	Single	Single
VNbMoTa	Multi	Single	Single	Single	Single
VNbMoW	Multi	Single	Single	Single	Single
VNbTaW	Multi	Single	Single	Single	Single
VMoTaW	Multi	Multi	Single	Single	Single
NbMoTaW	Multi	Multi	Multi	Multi	Multi
VNbMo	Multi	Single	Single	Single	Single
VNbTa	Multi	Single	Single	Single	Single
VNbW	Multi	Single	Single	Single	Single
VTaW	Multi	Single	Multi	Multi	Multi
VMoTa	Multi	Single	Single	Single	Single
VMoW	Multi	Multi	Multi	Multi	Multi
NbMoTa	Multi	Single	Single	Single	Single
NbMoW	Multi	Multi	Multi	Multi	Multi
NbTaW	Multi	Single	Single	Single	Single
MoTaW	Single	Single	Single	Single	Single
VNb	Multi	Single	Single	Single	Single
VMo	Multi	Single	Single	Single	Single
VTa	Multi	Single	Single	Single	Single
VW	Multi	Multi	Multi	Multi	Multi
NbMo	Single	Single	Single	Single	Single
NbTa	Multi	Single	Single	Single	Single
NbW	Multi	Multi	Multi	Multi	Multi
MoTa	Single	Single	Single	Single	Single
MoW	Multi	Multi	Multi	Multi	Multi
TaW	Single	Single	Single	Single	Single

Table 1.2. From XRD, the alloys were categorized as single-phase BCC (green), or multiphase (red).

	As-Cast	Homogenized	800°C	1000°C	1200°C
TiZrNbHfTa	BCC	BCC	BCC1+BCC2	BCC	BCC
TiZrNbHf	BCC	BCC	BCC	BCC	BCC
TiZrHfTa	HCP+BCC	HCP+BCC	HCP+BCC	-	-
TiZrNbTa	BCC1+BCC2	BCC	BCC1+BCC2	BCC1+BCC2	BCC1+BCC2
TiNbHfTa	BCC	BCC	BCC1+BCC2	BCC	BCC
ZrNbHfTa	BCC	BCC	BCC+HCP	BCC1+BCC2+HCP	BCC
TiZrHf	HCP	HCP	HCP	BCC+HCP	BCC+HCP
TiZrNb	BCC	BCC	BCC	BCC	BCC
TiZrTa	BCC1+BCC2+HCP	BCC+HCP	BCC1+BCC2+HCP	BCC1+BCC2	BCC
TiNbHf	BCC	BCC	BCC	BCC	BCC
TiHfTa	BCC	BCC	BCC	BCC	BCC
TiNbTa	BCC	BCC	BCC	BCC	BCC
ZrNbHf	BCC	BCC	BCC+HCP	BCC	BCC
ZrHfTa	BCC+HCP	BCC+HCP	BCC+HCP	BCC+HCP	BCC1+BCC2
ZrNbTa	BCC1+BCC2	BCC1+BCC2+HCP	BCC1+BCC2+HCP	BCC1+BCC2	BCC1+BCC2
NbHfTa	BCC	BCC	BCC+HCP	BCC	BCC
TiZr	HCP	HCP	HCP	HCP	HCP
TiHf	HCP1+HCP2	HCP	HCP	BCC+HCP	BCC+HCP
TiNb	BCC	BCC	BCC	BCC	BCC
TiTa	BCC	BCC	BCC	BCC	BCC
ZrHf	HCP	HCP	HCP	HCP	HCP
ZrNb	BCC	BCC	BCC1+BCC2	BCC	BCC
ZrTa	BCC+HCP	BCC+HCP	BCC+HCP	BCC+HCP	BCC1+BCC2
NbHf	BCC	BCC	BCC+HCP	BCC+HCP	BCC
HfTa	BCC	BCC+HCP	BCC+HCP	BCC+HCP	BCC+HCP
NbTa	BCC	BCC	BCC	BCC	BCC

	As-Cast	Homogenized	800°C	1000°C	1200°C
VNbMoTaW	BCC	BCC	BCC	BCC	BCC
VNbMoTa	BCC1+BCC2	BCC1+BCC2	BCC	BCC	BCC
VNbMoW	BCC1+BCC2	BCC1+BCC2	BCC	BCC	BCC
VNbTaW	BCC1+BCC2	BCC	BCC	BCC	BCC
VMoTaW	BCC1+BCC2	BCC1+BCC2	BCC	BCC	BCC
NbMoTaW	BCC	BCC	BCC	BCC	BCC
VNbMo	BCC1+BCC2	BCC1+BCC2	BCC	BCC	BCC
VNbTa	BCC1+BCC2	BCC	BCC1+BCC2	BCC1+BCC2	BCC
VNbW	BCC	BCC	BCC	BCC	BCC
VTaW	BCC	BCC	BCC+HCP	BCC+HCP	BCC
VMoTa	BCC1+BCC2	BCC1+BCC2	BCC	BCC	BCC
VMoW	BCC1+BCC2	BCC	BCC	BCC	BCC
NbMoTa	BCC	BCC	BCC	BCC	BCC
NbMoW	BCC	BCC	BCC	BCC	BCC
NbTaW	BCC	BCC	BCC	BCC	BCC
MoTaW	BCC	BCC	BCC	BCC	BCC
VNb	BCC	BCC	BCC	BCC	BCC
VMo	BCC1+BCC2	BCC	BCC	BCC	BCC
VTa	BCC	BCC	BCC+FCC	BCC+FCC	BCC+FCC
VW	BCC	BCC1+BCC2	BCC1+BCC2	BCC1+BCC2	BCC1+BCC2
NbMo	BCC	BCC	BCC	BCC	BCC
NbTa	BCC	BCC	BCC	BCC	BCC
NbW	BCC	BCC	BCC	BCC	BCC
MoTa	BCC	BCC	BCC	BCC	BCC
MoW	BCC	BCC	BCC	BCC	BCC
TaW	BCC	BCC	BCC	BCC	BCC

Table 1.3. This table shows condensed versions of Table 1.1 and Table 1.2. The percentages shown represent how many alloys within a particular grouping (binary, ternary, etc.) comprise a single BCC phase (based on SEM microstructure or XRD crystal structure). For example, of the total 10 binaries in Table 1.1 and Table 1.2, only 3 (or 30%) consist of a single BCC phase after the 800°C anneal, and so on.

TiZrNbHfTa Microstructure	800°C	1000°C	1200°C
Binary	30%	50%	80%
Ternary	40%	50%	70%
Quarternary	40%	60%	100%
Quinary	0%	100%	100%

TiZrNbHfTa Crystal Structure	800°C	1000°C	1200°C
Binary	30%	40%	50%
Ternary	40%	60%	80%
Quarternary	40%	50%	100%
Quinary	0%	100%	100%

VNbMoTaW Microstructure	800°C	1000°C	1200°C
Binary	78%	70%	70%
Ternary	70%	70%	70%
Quarternary	80%	80%	80%
Quinary	100%	100%	100%

VNbMoTaW Crystal Structure	800°C	1000°C	1200°C
Binary	80%	80%	80%
Ternary	80%	80%	90%
Quarternary	100%	100%	100%
Quinary	100%	100%	100%

all cases, the alloys tend to become more single phase as the temperature increases, which is due to the increasing contribution of entropy.

The qualitative trends discussed above can be quantified to gain better understanding, as shown in Figure 1.5. In the case of the V-Nb-Mo-Ta-W system, single phase BCC stability increases with increasing number of elements, with little influence of temperature when the number of constituents is fixed. In contrast, in the case of the Ti-Zr-Nb-Hf-Ta system, both temperature and configurational entropy have different effects, as summarized below. (a) Increasing the temperature from 800°C to 1200°C uniformly increases BCC single-phase stability, (b) at the highest temperature of 1200°C, increasing the configurational entropy increases BCC phase stability, and (c) at the lower temperature of 800°C, BCC stability first increases with increasing number of constituent elements, reaches a peak around 3 or 4 elements, and then decreases when there are 5 constituent elements. The Ti-Zr-Hf-Nb-Ta RHEA system is more akin to the FCC Cr-Mn-Fe-Co-Ni HEA system, in which Otto et al. replaced one element at a time (so that configurational entropy was kept constant) and showed that of all the resulting alloys only the base alloy (CrMnFeCoNi) had the FCC single-phase structure; they concluded that configurational entropy is not the main driving force behind phase stability, and that enthalpy and non-configurational entropy have stronger influences [29]. For purposes of the present study, it is worth noting that only one of the constituent elements in the Cr-Mn-Fe-Co-Ni system has the FCC structure at room temperature and only two of the elements in the Ti-Zr-Hf-Nb-Ta system have the BCC structure. Therefore, it is likely

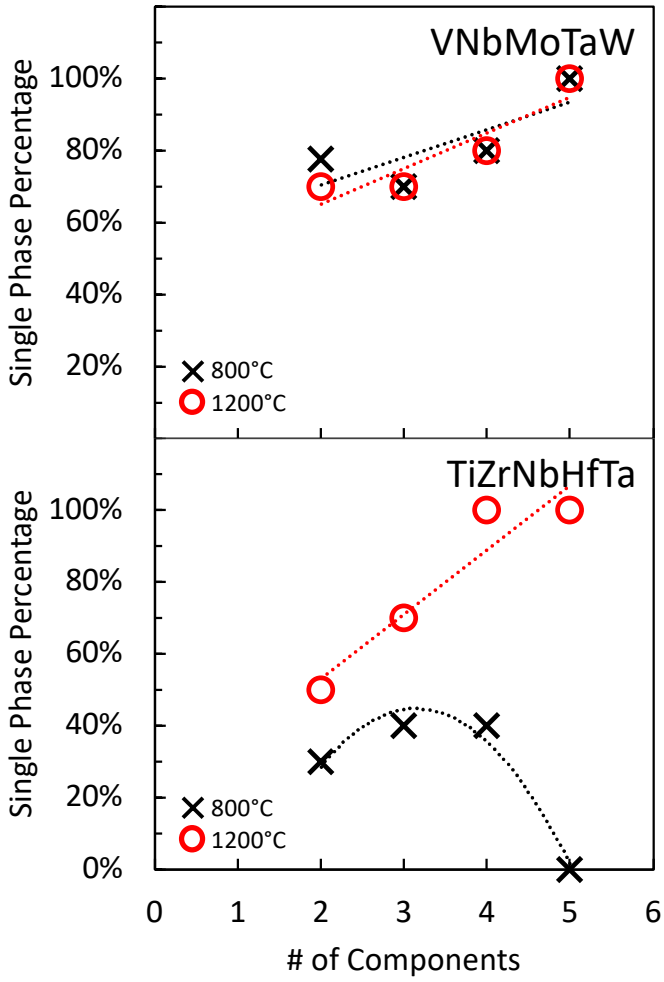

Figure 1.5. A plot of the data in Table 1.3 showing single-phase BCC percentage as a function of the number of components at two different temperatures

that in both systems the presence of competing crystal structures may outweigh the effects of configurational entropy.

In light of the above, the results for the Ti-Zr-Nb-Hf-Ta system are re-plotted as shown in Figure 1.6 where the BCC phase percentage of a given alloy (be it binary, ternary, quaternary or quinary) is plotted as a function of the fraction of elements in that alloy that are BCC at room temperature. From the lines bracketing the data points in the top and bottom figures, it appears that the BCC phase percentage increases with increasing fraction of BCC elements in the alloys. However, additional work is needed to confirm how real this trend is. For that, off-equiatomic alloys will need to be produced and analyzed because equiatomic alloys are limited to those in the present study and they appear to be insufficient to draw firm conclusions.

With the single-phase BCC stability of the alloys in the V-Nb-Mo-Ta-W system being generally higher for all conditions investigated, we can compare it to those in the Ti-Zr-Nb-Hf-Ta system. This stability appears to show good correlation with one of the Hume-Rothery rules for solid solution formation, namely extensive mutual solubilities of the constituent binaries, as shown in Figure 1.7. Therefore, good mutual solubility of the constituent binaries (which can be easily deduced by examining published phase diagrams) may be a first rule of thumb that needs to be satisfied when designing single-phase RHEAs.

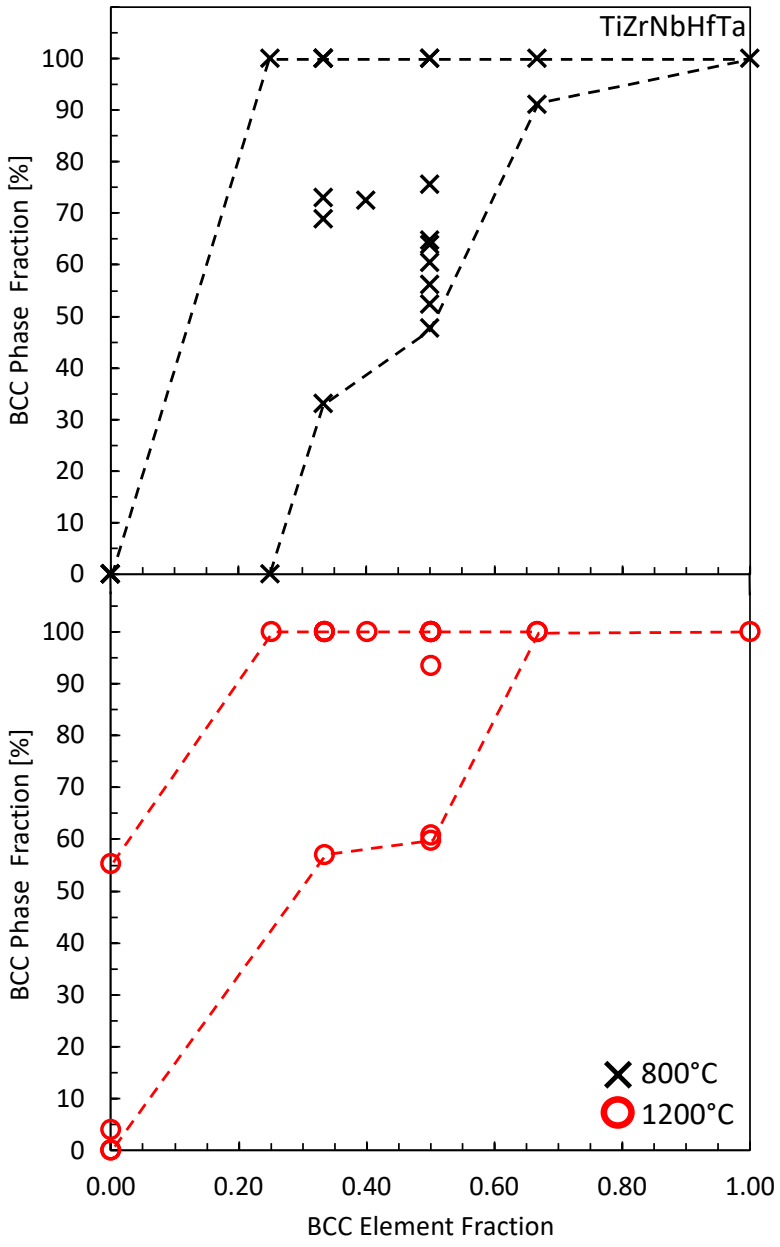

Figure 1.6. BCC phase percentage in the various alloys as a function of BCC element fraction in each alloy. The lines bounding the data at the top and bottom are merely to guide the eye.

Structure	Ti	Zr	Nb	Hf	Ta
Ti	Yes	Yes	No	Yes	No
Zr		Yes	No	Yes	No
Nb			Yes	No	Yes
Hf				Yes	No
Ta					Yes

Structure	V	Nb	Mo	Ta	W
V	Yes	Yes	Yes	Yes	Yes
Nb		Yes	Yes	Yes	Yes
Mo			Yes	Yes	Yes
Ta				Yes	Yes
W					Yes

Binary Solution	Ti	Zr	Nb	Hf	Ta
Ti	Yes	Yes	No	Yes	No
Zr		Yes	No	Yes	No
Nb			Yes	No	Yes
Hf				Yes	No
Ta					Yes

Binary Solution	V	Nb	Mo	Ta	W
V	Yes	Yes	Yes	No	Yes
Nb		Yes	Yes	Yes	Yes
Mo			Yes	Yes	Yes
Ta				Yes	Yes
W					Yes

Figure 1.7. Pairwise comparison of the binary constituents of the Ti-Zr-Nb-Hf-Ta and V-Nb-Mo-Ta-W systems. Crystal structures of the constituent pairs are shown at the top and mutual solid solubility at the bottom. Both criteria favor the formation of more single-phase BCC solid solutions in V-Nb-Mo-Ta-W than in Ti-Zr-Nb-Hf-Ta [82].

Summary

In accordance with the Hume-Rothery rules for solid solution formation, the VNbMoTaW system had a higher overall single-phase BCC percentage at all temperatures than the TiZrNbHfTa system. In both systems, single-phase solid solutions were favored at high temperatures. At low temperatures, Hume-Rothery rules may be applicable to other systems if solid solutions are desirable, especially if alloying elements with the same crystal structure and extended mutual solubility are chosen after considering all possible binary combinations of the constituent elements.

Chapter 2 Mechanical Properties of Pseudobinary Ti-Zr-Nb-Hf-Ta

This chapter is being prepared for publication in a peer-reviewed journal. JM Brookins performed all of the experimental work and wrote the initial draft. Ian Stinson assisted with the sample machining. BL Musico, C Kinsler-Fedon, and R Tanveer assisted with the collection and analysis of RUS data. Y Yang developed the CALPHAD database and performed the thermodynamics calculations. EP George conceived and supervised the study.

Introduction

As originally shown by Senkov et al., the equiatomic TiZrNbHfTa quinary alloy displays ductility in tension at room temperature [43]. It can be cold-worked to a thickness reduction of 86-89%, can be compressed to strains of at least 50%, and has been reported to display a tensile ductility of 18.5% [43, 45, 83]. Lilensten et al. showed by XRD that an off-equiatomic composition, $Ti_{35}Zr_{27.5}Nb_5Hf_{27.5}Ta_5$ (at%) in the as-cast condition had an orthorhombic crystal structure, identified as α'' orthorhombic martensite, which relaxed into a twinned hexagonal α' structure during TEM sample preparation [84]. They further explored the tensile properties of this alloy by cold-rolling and recrystallizing samples to a 40 μm grain size with a single-phase BCC structure: the alloy displayed a yield strength of 540 MPa with an ultimate tensile strength of 995 MPa, and a tensile ductility of 23% [8]. Interrupted tensile testing with XRD showed that transformation-induced plasticity (TRIP) involving a BCC to orthorhombic phase transformation was responsible for the tensile properties [8].

In order to study the effect of BCC phase stabilization, Huang et al. used an as-cast quaternary $TiZrHfTa_x$ system, with Ta acting as a BCC-stabilizer, for Ta concentrations of 25%, 16.7%, 14.3%, and 11.8 at% [85]. At the equiatomic composition ($Ti_{25}Zr_{25}Hf_{25}Ta_{25}$), there was a single BCC phase; at $Ti_{27.8}Zr_{27.8}Hf_{27.8}Ta_{16.7}$, HCP was detected by EBSD, but not XRD, suggesting a low volume fraction; at $Ti_{28.6}Zr_{28.6}Hf_{28.6}Ta_{14.3}$ and $Ti_{29.4}Zr_{29.4}Hf_{29.4}Ta_{11.8}$, the microstructure was lamellar HCP plates in a BCC matrix [85]. Interestingly, the tensile stress-strain curve of the $Ti_{29.4}Zr_{29.4}Hf_{29.4}Ta_{11.8}$ composition clearly showed dual-yield points, indicative of a phase transformation and this was proven with *in situ* diffraction data showing a change in relative intensities between the decreasing BCC and increasing HCP phases [85].

By replacing Ta with V, Fazakas et al. showed that TiZrHfNbV could develop a single-phase BCC structure after 10 min heat-treatments at 300°C, 500°C, or 700°C; with compressive strains of 30%, 38%, and 29.7%, respectively [86]. Wider work has been done within the greater Cr-Mo-W-V-Nb-Ta-Ti-Zr-Hf-Al system, in order to computationally identify likely alloys possessing both single-phase stability and room-temperature ductility [87]. In this study, several equiatomic, quinary, candidate alloys were derived from the quaternary Hf-Mo-Nb-Ti system and were shown to have good compressive ductility; unfortunately, these alloys were tested using a dendritic, as-cast microstructure [87].

Until now, little work has been done on two fundamental aspects of the Ti-Zr-Nb-Hf-Ta system: the effect of compositional changes on the intrinsic ductility of the BCC phase and a systematic approach to the exploration of such changes. If the intrinsic ductility of the single-phase BCC structure is affected by BCC-HCP phase transformations and shear modulus changes, then their effects can be more easily investigated with the help of pseudobinary phase diagrams that simplify the otherwise vast compositional space that would need to be probed. Suitable examples would include A-B pseudobinaries where the "A" elements all have the HCP crystal structure at room temperature and the "B" elements are BCC.

Experimental Methods

Pseudobinary subsets of the Ti-Zr-Nb-Hf-Ta system consisting of grouped BCC- and HCP-elements were envisioned as follows. Since Ti, Zr, and Hf are HCP at room temperature while Nb and Ta are BCC at room temperature, the terms HCP_{eq} and BCC_{eq} were defined as follows.

$$HCP_{eq} = Ti + Zr + Hf\ (at\%) \qquad \textbf{Eqn 2.1}$$

$$BCC_{eq} = Ta + Nb\ (at\%) \qquad \textbf{Eqn 2.2}$$

CALPHAD was then used to calculate the pseudobinary phase diagram in terms of BCC_{eq} (Figure 2.1**)** using CompuTherm's Pandat software package and a database developed by **Y Yang** specifically for Ti-Zr-Nb-Hf-Ta, in order to identify regions of compositional interest based on the following criteria:

- Melting temperature, due to arc-melting limitations

- Avoid areas of spinodal decomposition, to best maintain a single BCC phase
- Compositions that can be heat-treated and recrystallized within a single-phase region, for the best chances at maintaining a single BCC phase post-quenching

From this, five compositions were chosen to establish the effects of the BCC-elements on mechanical properties:

1. TiZrHf (BCC_{eq} = 0.0),
2. $Ti_{30}Zr_{30}Nb_5Hf_{30}Ta_5$ (BCC_{eq} = 0.1)
3. $Ti_{26.7}Zr_{26.7}Nb_{10}Hf_{26.7}Ta_{10}$ (BCC_{eq} = 0.2)
4. $Ti_{23.3}Zr_{23.3}Nb_{15}Hf_{23.3}Ta_{15}$ (BCC_{eq} = 0.3)
5. $Ti_{20}Zr_{20}Nb_{20}Hf_{20}Ta_{20}$ (BCC_{eq} = 0.4)

Buttons of each alloy were produced by arc-melting under an argon atmosphere (Figure 2.2). Before melting, the chamber was evacuated to, at least, 2.5 x 10^{-5} Pa, then backfilled with argon. This purge and backfill was repeated for a total of three times, and then a Ti-getter was melted and solidified to remove any residual oxygen. In order to obtain a homogenous sample, each button was flipped and remelted, at least five times. Ingots were produced by drop-casting the molten alloy into a square cross-section copper mold, with charges sized appropriately to leave a substantial hot-top (Figure 2.3). The hot-tops were removed from the casting and the ingots were then encapsulated in argon-filled quartz, as previously described, for homogenization at 1200°C for 24 hours. This workflow is shown in Figure 2.4.

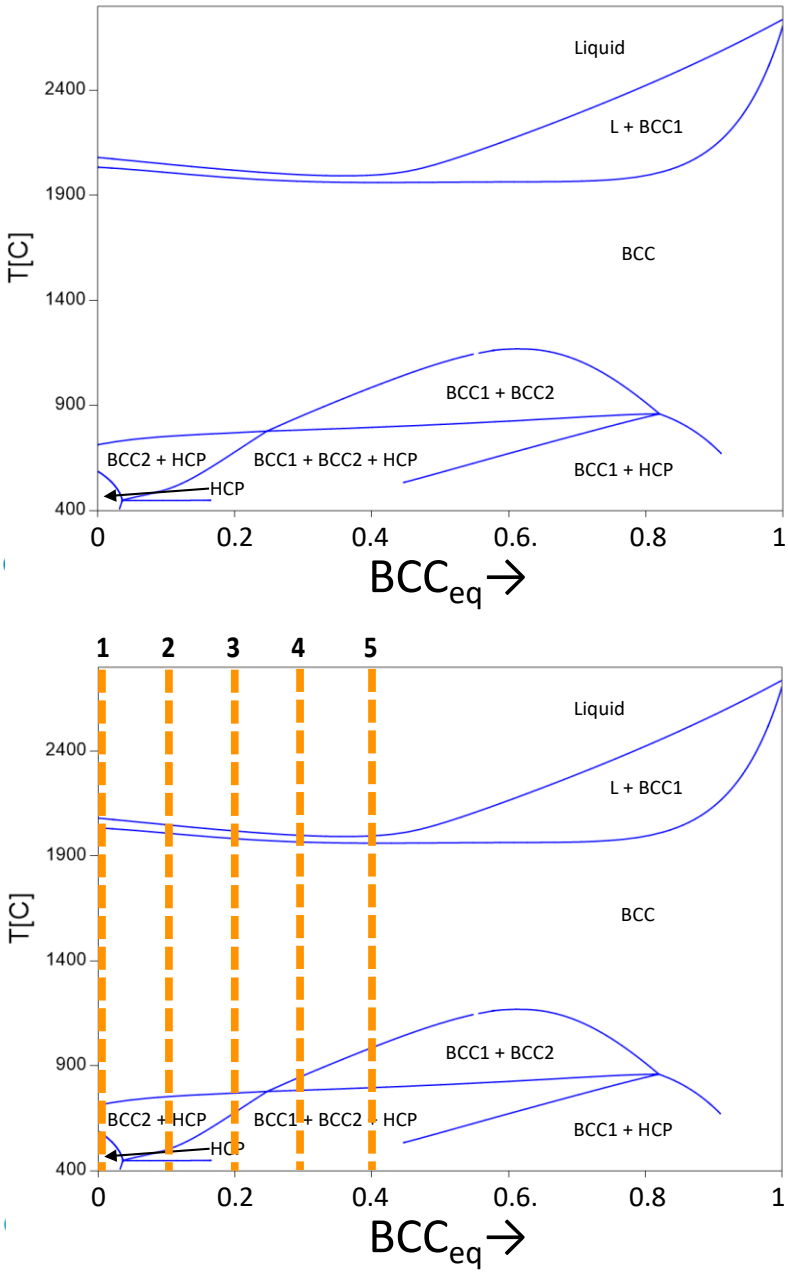

Figure 2.1. The pseudo-binary phase diagram (top) calculated based on BCC_{eq} (note that BCC_{eq} + HCP_{eq} = 1, that is, HCP_{eq} = 1 - BCC_{eq}). In this figure, the X-axis represents the equiatomic BCC_{eq}, that is, the Ta and Nb concentrations are equal and BCC_{eq} is their sum. In the bottom figure, dashed lines show the five compositions of interest: $BCC_{eq}0.0$, $BCC_{eq}0.1$, $BCC_{eq}0.2$, $BCC_{eq}0.3$, and the equiatomic $BCC_{eq}0.4$.

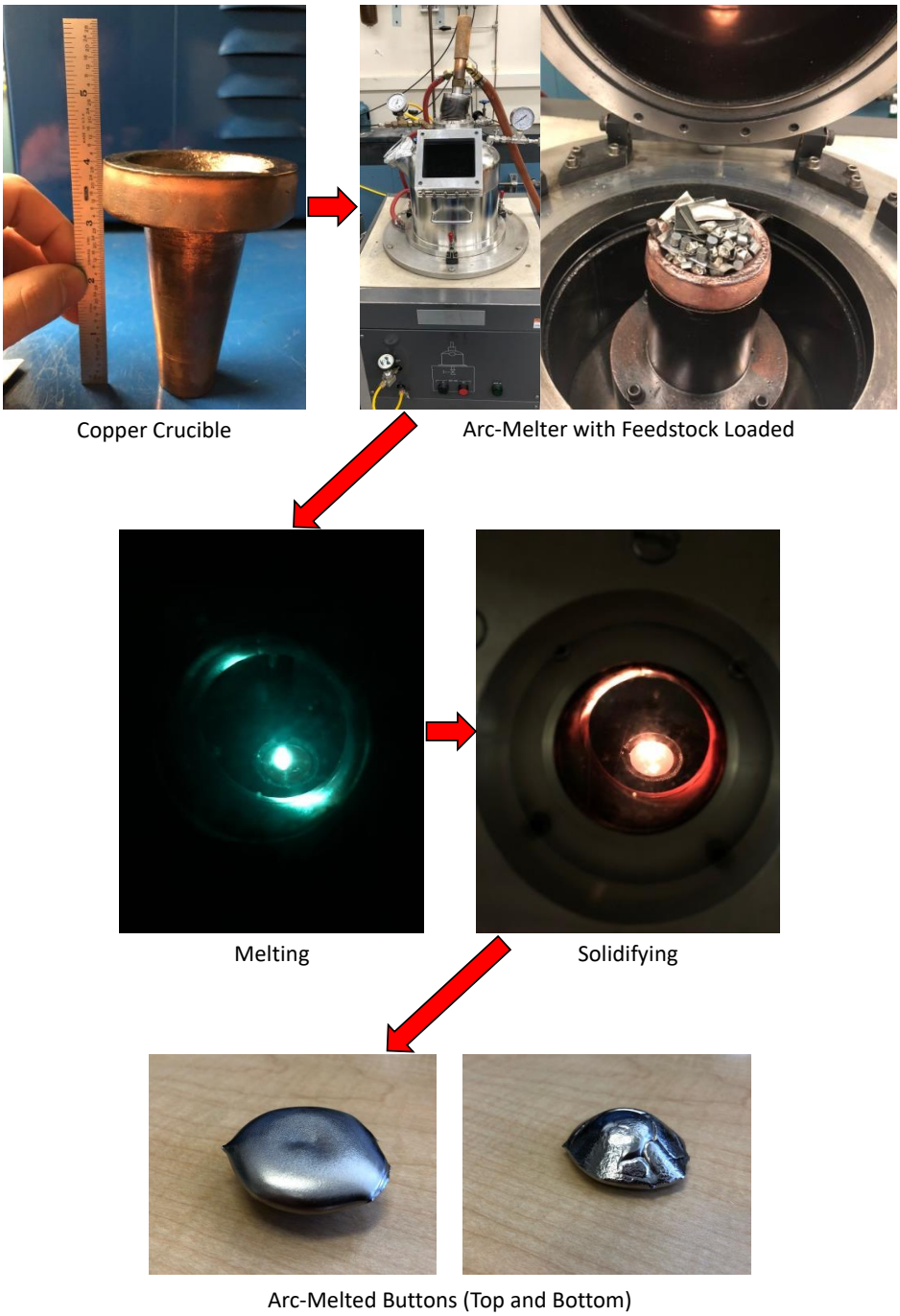

Figure 2.2. Arc melting begins with loading the water-cooled copper crucible with the charge (top row), then after a vacuum-and-purge cycle to minimize the residual oxygen and nitrogen, the charge is melted and solidified (middle), before being removed (bottom) prior to casting.

Ideal Casting

Crucible Melt Damage

Incomplete Casting

Copper Bonding

Figure 2.3. The ideal casting is shown at the top. However, problems can arise during arc-melting. Crucible damage (bottom left) occurs when the copper mold is unable to dissipate enough heat before the alloyed button goes molten. An incomplete casting (bottom top right) can happen for several reasons, the alloyed button may not go completely molten fast enough, leading to drips; or the molten alloy may touch the sides of the mold and freeze prior to filling the bottom first, leading to a cold shut. Finally, the button may bond to the copper (bottom right) if there is minimal surface contact, leading to hot spots against the mold.

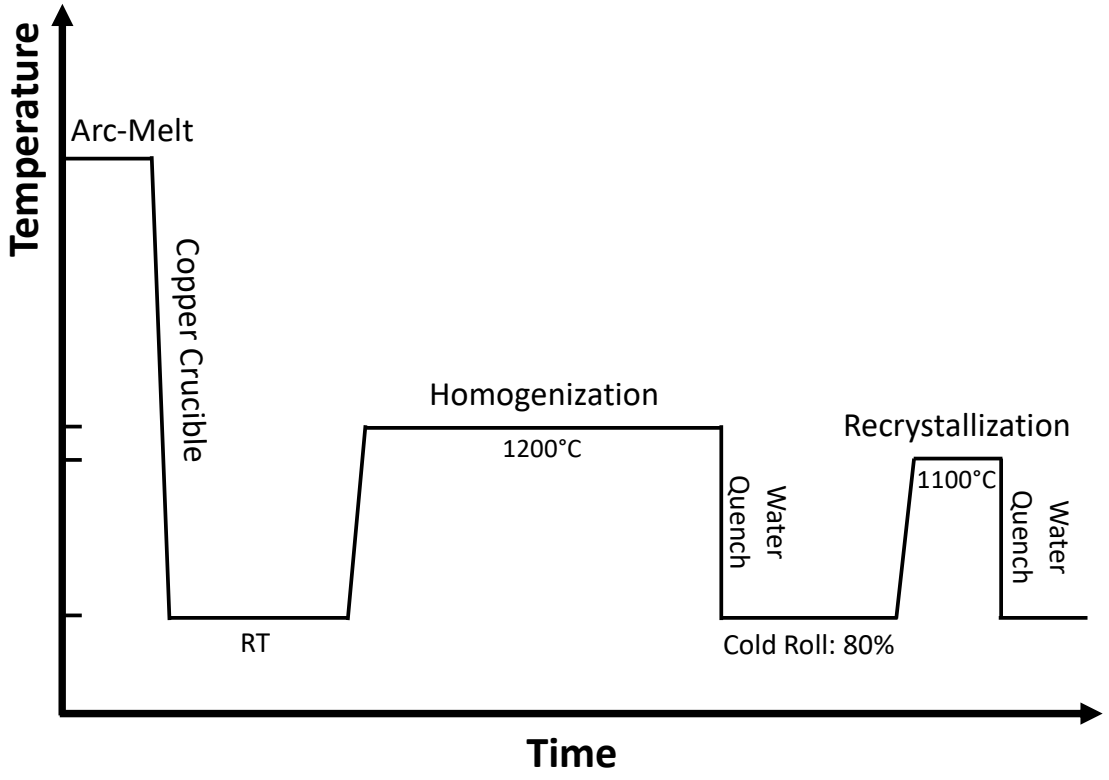

Figure 2.4. The processing of the pseudobinary alloys begins with arc-melting in a water-cooled copper crucible, followed by homogenization at 1200°C for 24 hours. The homogenized ingot is then cold-rolled to an 80% reduction in thickness, then recrystallized at 1100°C to obtain the desired grain size.

Once homogenized, SEM/EDS was used to verify chemical homogeneity in a prepared section of ingot, while XRD was used to verify its single-phase BCC structure. After that, the ingots were split lengthwise to identify areas of internal porosity. If porosity was shallow and broad, then surface grinding was performed to evenly remove a minimal amount of thickness; for deeper, more concentrated porosity, small sections were cut from the bulk avoiding these locations to maintain maximum thickness using wire-EDM. Prior to cold-rolling, all surfaces were ground to 1200 grit and all sharp edges were rounded to prevent any stress concentrations leading to cracking. Cold-rolling was done with 2-5% reductions per pass, until 80% reduction in thickness was achieved; cross-rolling was only performed to remove curvature, not for reduction.

For recrystallization, test coupons and appropriately sized tensile blanks were cut parallel to the rolling direction, cleaned, and then encapsulated in quartz using the prior procedure. Based on prior experience, a temperature of 1100°C was chosen with intervals from 15-30 minutes. Grain size was measured from backscatter SEM images and crystal structure was determined using x-ray diffraction.

Tensile tests (n = 3) were performed on an Intron 5900R, using a constant crosshead speed corresponding to an initial strain rate of 10^{-3} s^{-1}. Strain was tracked using two methods: fracture elongation was determined from gauge markers on the initial gauge length and measuring their change in spacing after fracture, while digital image correlation (DIC) was used to track the tensile strain throughout testing using a speckle

pattern on the tensile bar using a camera and Correlated Solution's VIC-2D software package (Figure 2.5).

Resonant ultrasound spectroscopy (RUS) was used to determine the shear modulus of each alloy. Rectangular parallelepiped RUS specimens of approximate dimensions 2 x 3 x 4 mm were prepared by wire-EDM and their surfaces carefully ground to preserve the right-angle corners and parallel faces. The RUS set-up and specimen can be seen in Figure 2.6. Once resonant frequencies were measured from 100 kHz to 1.5 MHz, the patterns were fitted using the software package provided by RUS Alamo Creek, with an RMS error for each fit of less than 0.5%.

In order to determine any post-fracture phase transformation, x-ray diffraction was performed using an x-ray mirror to solely interrogate the deformed gauge length. Fracture surfaces were imaged using a benchtop SEM operating at 5 kV.

Results and Discussion

After homogenization, XRD showed that the TiZrHf alloy ($BCC_{eq}0.0$), which contained no BCC elements, did not have a single-phase BCC structure. The other four alloys exhibited only BCC peaks (Figure 2.7). Upon rolling after homogenization, the alloys displayed varying degrees of deformability as seen in Figure 2.8 and summarized below.

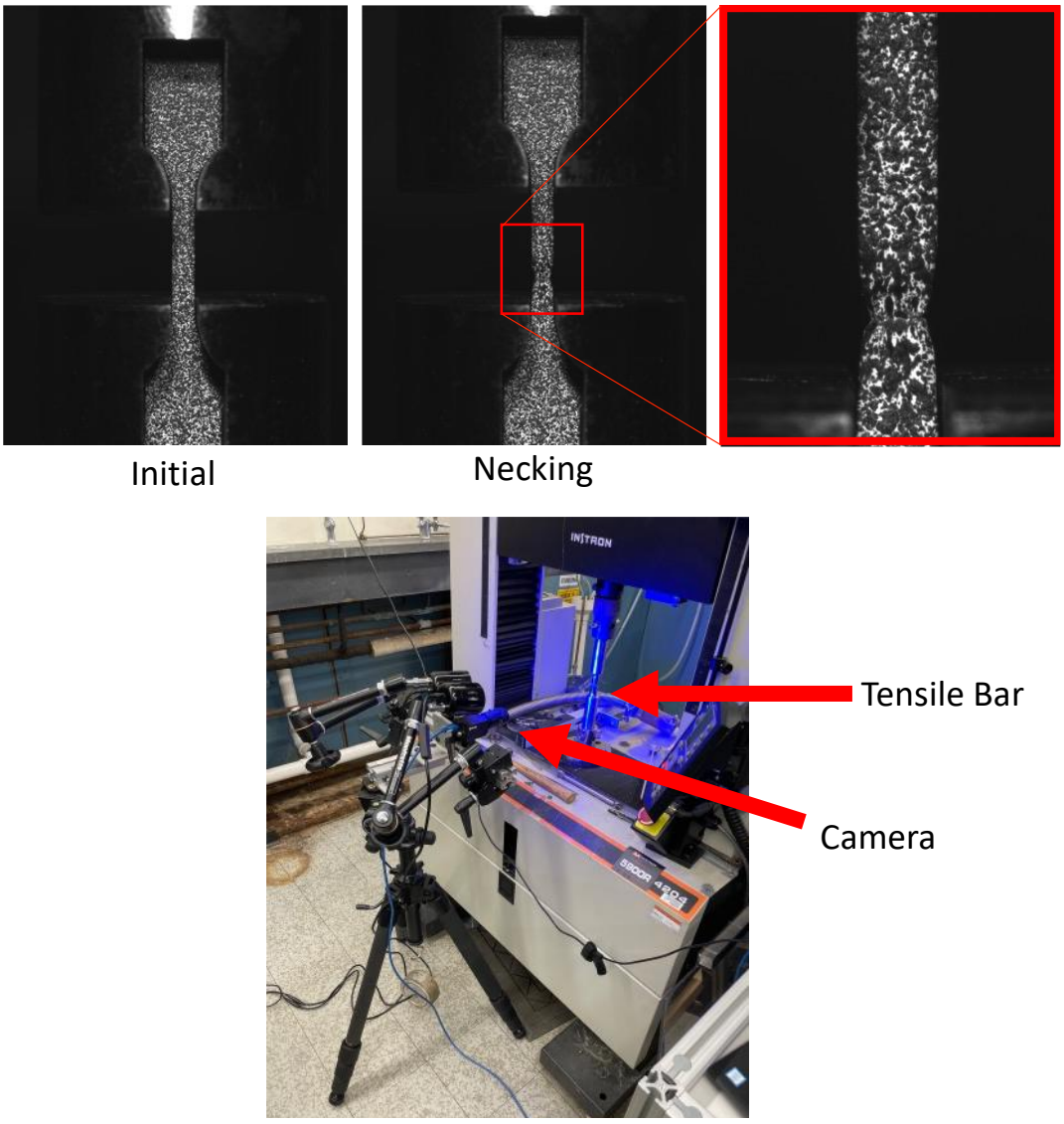

Figure 2.5. The digital image correlation (DIC) set-up showing an example of the collected images (top), and the equipment set-up (bottom). As shown in the zoomed inset of the necked region (top right), resolution is sufficient even with small tensile bars.

- $BCC_{eq}0.0$
    - Cracking began at 15-20% cold work (CW).

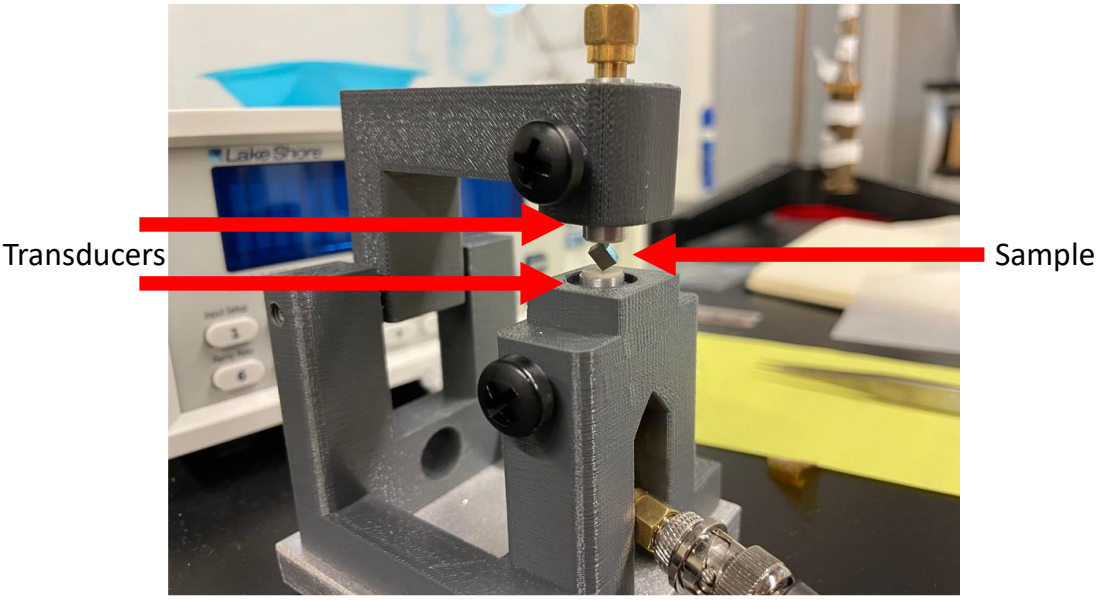

Figure 2.6. The digital RUS stage from RUS Alamo Creek shows the two transducers holding the specimen. The driving amplifier is not shown in this example.

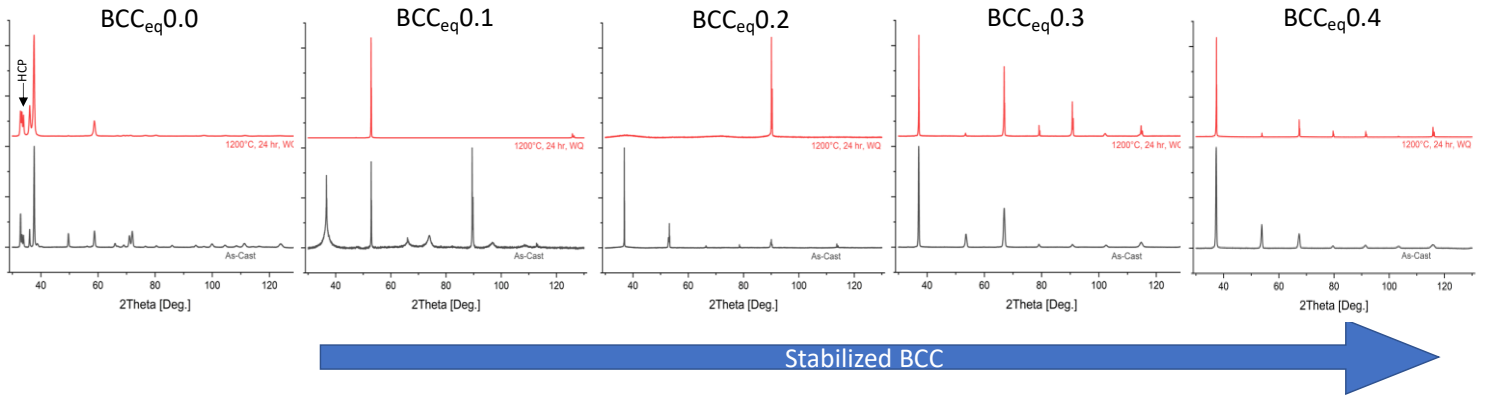

Figure 2.7. XRD patterns of the investigated alloys, both in the as-cast state and after homogenization at 1200°C for 24 h followed by water-quenching. In all alloys except BCC$_{eq}$0.0, only peaks corresponding to the BCC crystal structure are present.

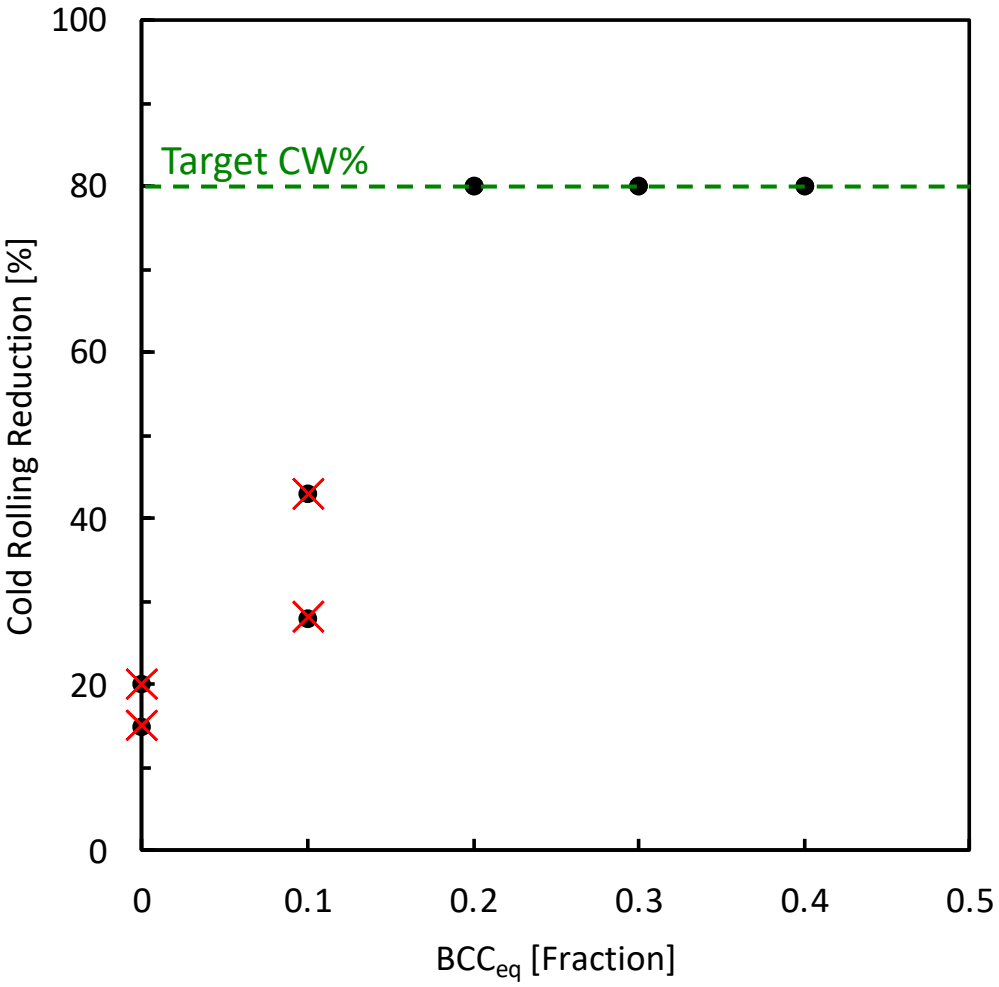

Figure 2.8. During cold-rolling, only three compositions reached the 80% thickness reduction target without cracking: $BCC_{eq}0.2$, $BCC_{eq}0.3$, and $BCC_{eq}0.4$.

- $BCC_{eq}0.1$
    - Cracking began at 28-43% CW.
- $BCC_{eq}0.2$
    - 80% CW down to final thickness, no visible edge cracking.
- $BCC_{eq}0.3$
    - 80% CW down to final thickness, no visible edge cracking.
- $BCC_{eq}0.4$
    - 80% CW down to final thickness, no visible edge cracking

After cold-rolling, a metallographic specimen from the $BCC_{eq}0.1$ alloy was investigated and found to have a deformation-induced HCP phase, which likely caused the cracking (Figure 2.9). Together, the above results suggest that the HCP phase is detrimental to deformability (regardless of whether it is present before the start of cold rolling, in $BCC_{eq}0.0$, or generated during cold rolling, in $BCC_{eq}0.1$).

After recrystallization, $BCC_{eq}0.2$, $BCC_{eq}0.3$ and $BCC_{eq}0.4$ were found to have nominally similar grain sizes and a single-phase BCC structure (Figure 2.10). Representative tensile stress-strain curves for these three alloys are shown in Figure 2.11. The engineering stress-strain curves show that yield strength increases with increasing BCC_{eq}, with the largest increase occurring between $BCC_{eq}0.3$ and $BCC_{eq}0.4$. After yielding, the alloys show little to no work hardening. The elongation to fracture increases as the BCC_{eq} increases from 0.2 to 0.3 and then slightly decreases when the BCC_{eq} increases to 0.4. In

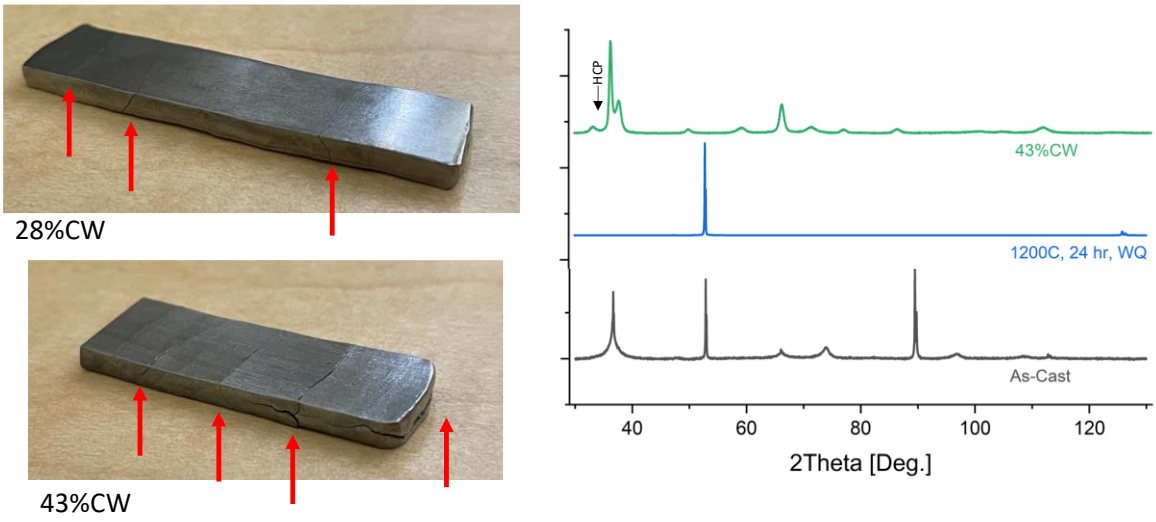

Figure 2.9. After cracking during cold-rolling (red arrows, left), the $BCC_{eq}0.1$ composition was found by XRD to have a deformation-induced HCP phase (right).

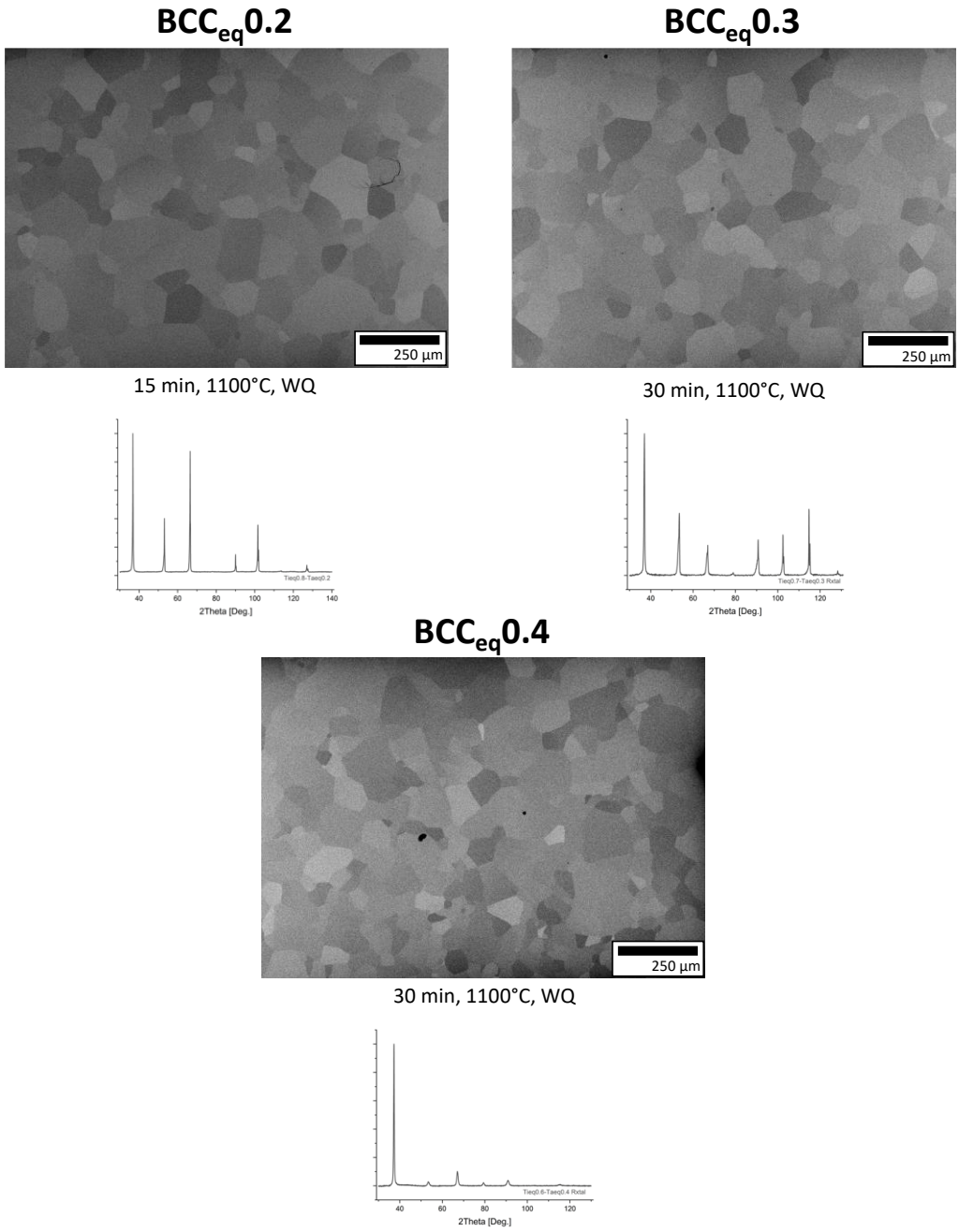

Figure 2.10. SEM backscatter images and XRD patterns of the recrystallized $BCC_{eq}0.2$, $BCC_{eq}0.3$ and $BCC_{eq}0.4$ alloys. The alloys have similar grain sizes and the BCC crystal structure.

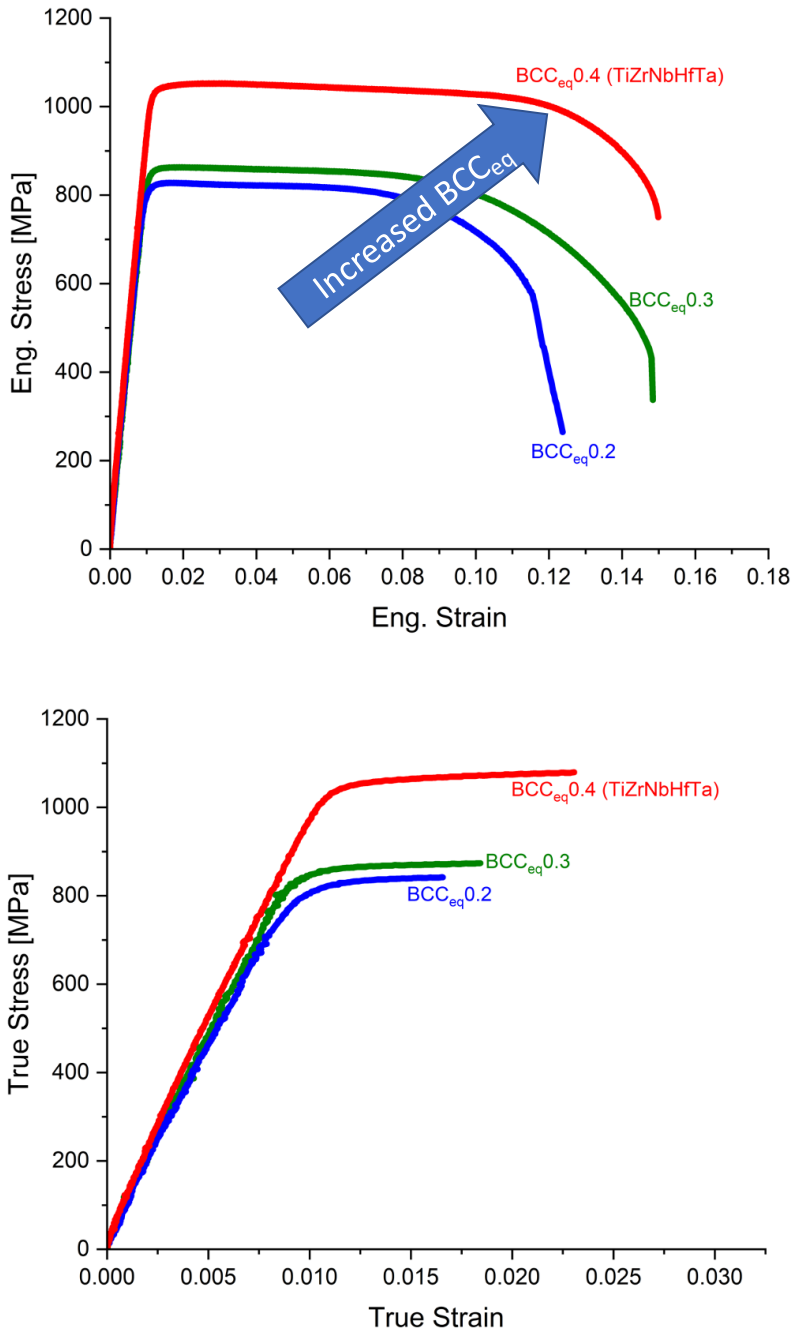

Figure 2.11. Representative tensile stress-strain curves of the three compositions showing engineering stress-strain (top) and true stress-strain (bottom). Loads were from load cells and displacements from DIC. The true stress-strain curve shows data only up to the point where necking starts.

addition, uniform elongation was also determined for each alloy, which is defined here as the tensile strain to reach the maximum in the engineering stress strain curves. Beyond that strain, the gauge sections started to neck, initially slowly but towards the end more rapidly. The average mechanical properties (from three tests on each composition) are tabulated below:

- $BCC_{eq}0.4$
    - σ_{yield}: 1033 ± 6 MPa
    - $\varepsilon_{uniform}$: 2.4 ± 0.3%
    - $\varepsilon_{fracture}$: 15 ± 3%
    - E: 95 ± 2 GPa
- $BCC_{eq}0.3$
    - σ_{yield}: 843 ± 8 MPa
    - $\varepsilon_{uniform}$: 1.9 ± 0.1%
    - $\varepsilon_{fracture}$: 20 ± 1%
    - E: 87 ± 3 GPa
- $BCC_{eq}0.2$
    - σ_{yield}: 796 ± 15 MPa
    - $\varepsilon_{uniform}$: 1.6 ± 0.1%
    - $\varepsilon_{fracture}$: 16 ± 2%
    - E: 81 ± 5 GPa

From RUS, shear moduli of the $BCC_{eq}0.4$, $BCC_{eq}0.3$, and $BCC_{eq}0.2$ compositions were determined to be 36.2 GPa, 29.3 GPa, and 28.8 GPa, respectively. Additionally, Young's modulus was calculated from RUS and was found to be 90 GPa, 76 GPa, and 76 GPa, respectively; in agreement with the equiatomic spread found in literature [88]. The RUS shear moduli were used to normalize the yield strengths, and the results are plotted in Figure 2.12, along with the un-normalized yield strengths. It appears that most of the effect of composition on yield strength can be explained by the composition dependence of shear modulus (more on this later).

As shown in Figure 2.13, post-fracture XRD showed no deformation-induced phase transformations. Additionally, the solidus temperatures for the compositions of interest here are relatively flat (Figure 2.1). Therefore, it appears that the shear modulus difference is largely responsible for the yield strength differences.

The engineering stress-strain curves (Figure 2.11) and fracture surfaces (Figure 2.14) indicate ductile failure in each alloy. Valence electron concentration (VEC) has been used a predictor of ductility with a VEC of less than 4.4 considered to be intrinsically ductile, whereas a VEC of over 4.6 is considered brittle [89]. Based on these criteria, the explored compositions fall within the ductile region; with the most uniformly ductile composition at the border of predicted ductility, as seen in Figure 2.15. Other predictors of ductility involving the effect of elastic moduli can be seen in Figure 2.16, where the studied compositions meet the ductility criterion based on Pugh's ratio [90] and Cauchy

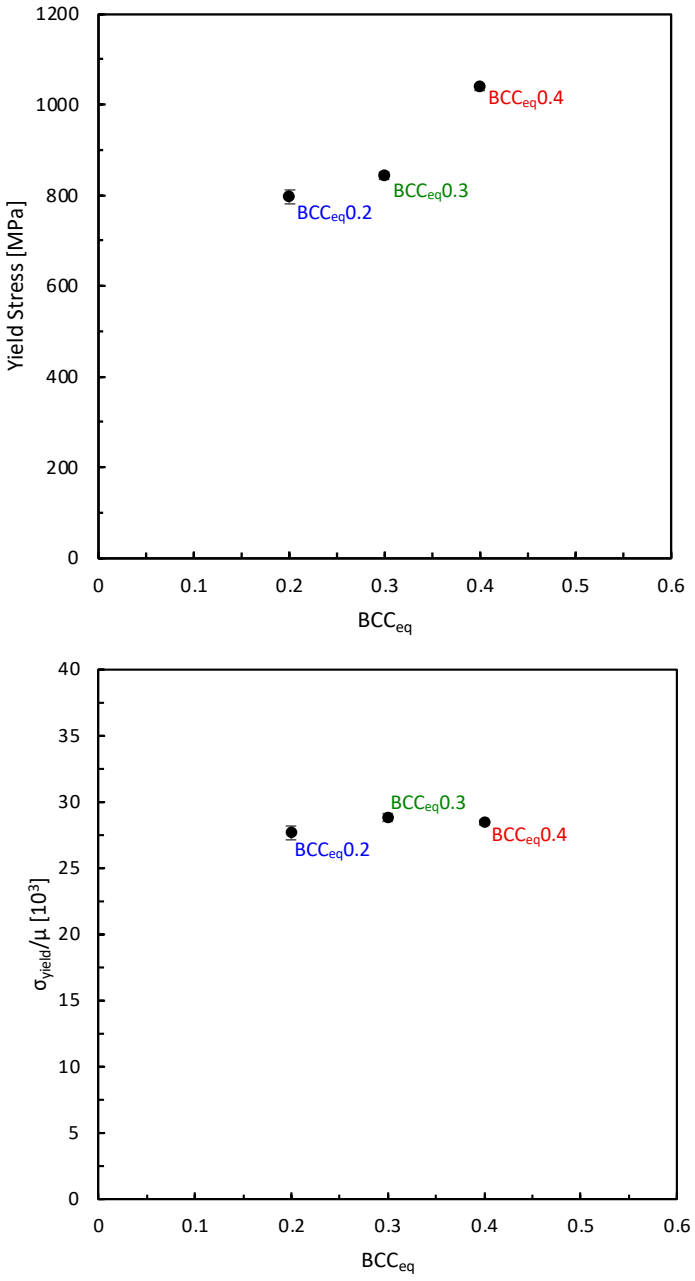

Figure 2.12. When plotted against BCC_{eq}, the yield strengths show a positive trend (top). Shear-modulus normalized yield strengths (bottom) show a roughly flat trend across the measured BCC_{eq} compositions.

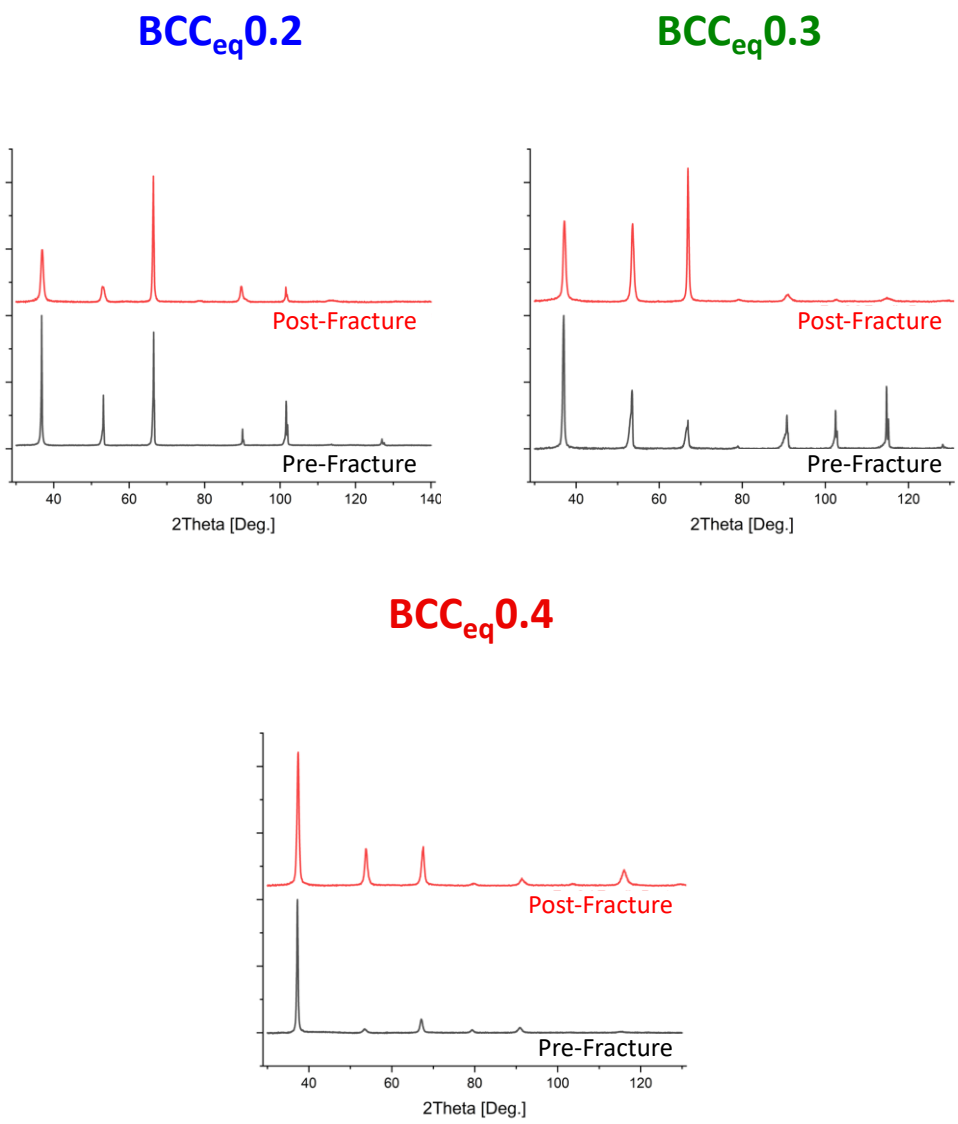

Figure 2.13. Post-fracture XRD shows no detectable, deformation-induced secondary phase formation in any of the investigated compositions.

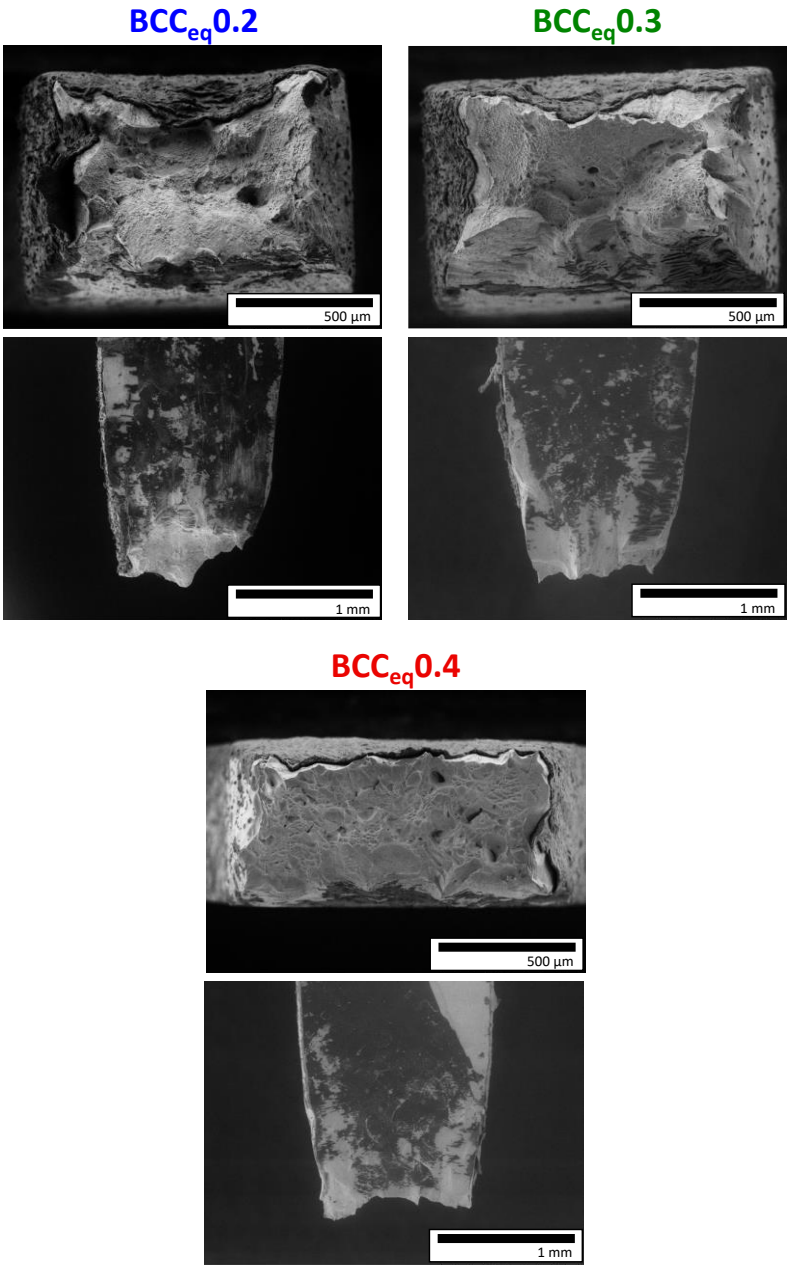

Figure 2.14. Fracture surfaces of each composition show features of ductile failure, including void formation and necking.

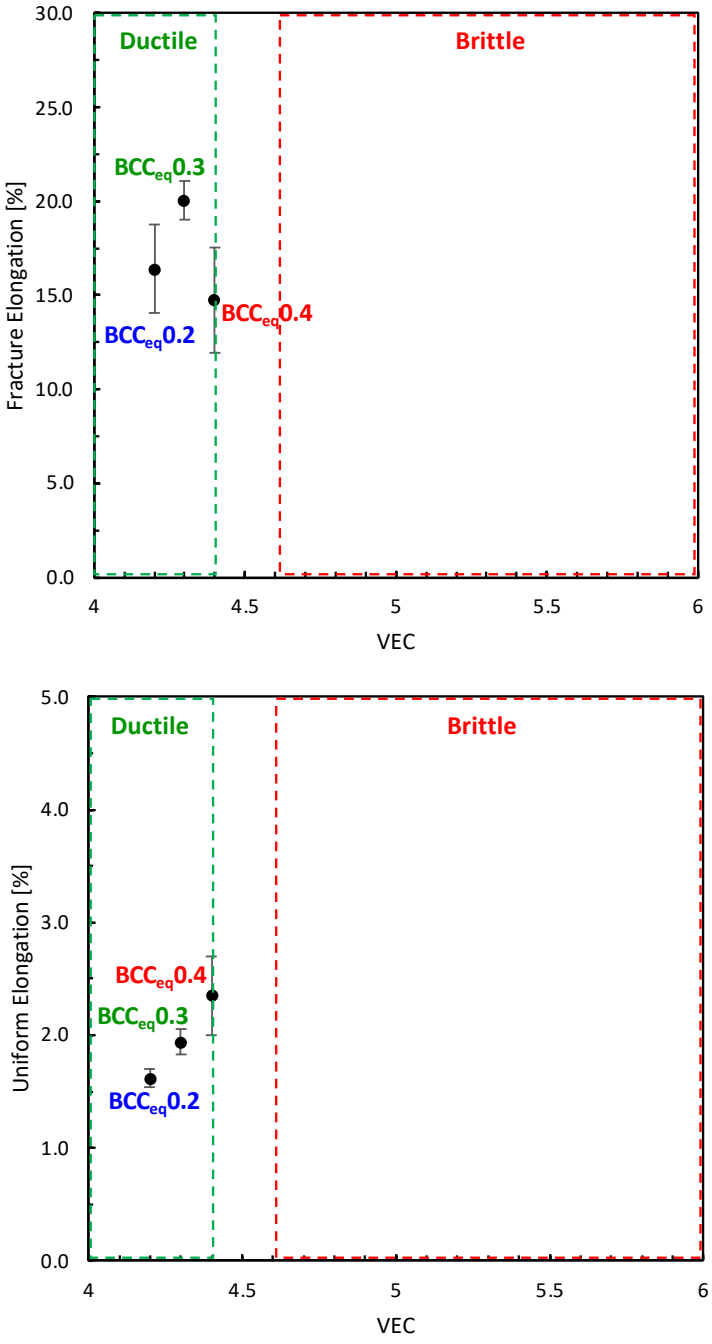

Figure 2.15. The calculated VEC of the studied compositions plotted against their fracture (top) and uniform (bottom) elongations. Ductile and brittle areas are <4.4 and >4.6, respectively [89].

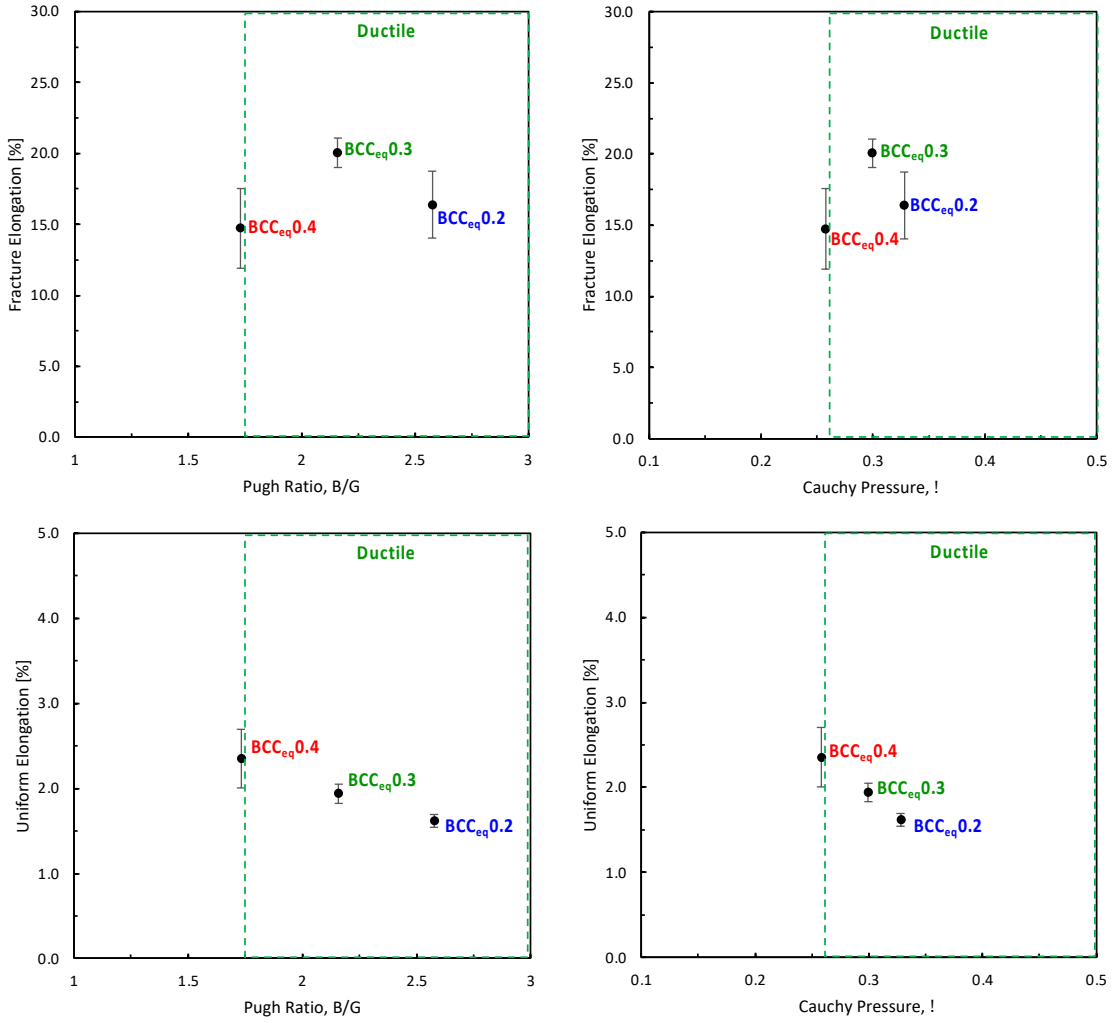

Figure 2.16. Comparisons of the fracture (top) and uniform (bottom) elongations to two additional ductility criteria. The Pugh ratio ductility criterion is > 1.75 for a ductile material [90]; the Cauchy pressure criterion (bottom) can be simplified to a Poisson's ratio of >0.26 [91].

pressure [91]. Once again, in each instance, the composition with the highest uniform elongation is at the border of ductility.

While the focus of this work looked at the influence of composition on ductility, it is worth exploring the mechanistic explanations of strengthening on these alloy systems. Due to the dislocation core structure within a BCC metal, strengthening theories are often based on the movement of screw dislocations. However, as shown in other BCC RHEAs, edge dislocations may be influenced by the complicated atomic landscape (lattice distortion) and play a role in strengthening, as well [92-94]. Follow on work by Baruffi et al. contributed a theory that BCC alloys having a large atomic misfit could transition from primarily screw dislocations to edge dislocations contributing a dominant strengthening effect [95]. While this work did not directly investigate ductility, dislocation movement nevertheless plays a pivotal role in the plastic deformation of a metal [96].

Summary

Five compositions were identified in the (TiZrHf) – (NbTa) pseudobinary phase diagram based on several criteria for workability. Three of them were able to be processed for mechanical testing. They were the lower melting temperature alloys that were higher in TiZrHf, which are all HCP elements. The equiatomic TiZrNbHfTa alloy ($BCC_{eq}0.4$) was shown to have the highest uniform elongation. No composition displayed any evidence of transformation-induced plasticity after tensile testing. Three ductility criteria proposed in

the literature were considered, and the above alloy was found to lie at the ductile-brittle border predicted by the criteria.

Chapter 3 Temperature-Dependent Properties of Ti- and Zr-rich Ti-Zr-Nb-Hf-Ta Derivatives

This chapter is being prepared for publication in a peer-reviewed journal. JM Brookins performed all of the experimental work and wrote the initial draft. Ian Stinson assisted with the sample machining. BL Musico, C Kinsler-Fedon, and R Tanveer assisted with the collection and analysis of RUS data. EP George conceived and supervised the study.

Introduction

The Cantor alloy, a quinary FCC high entropy alloy, was previously shown to have had an extraordinarily high cryogenic fracture toughness due to a combination of activated deformation mechanisms [12, 97]. While most BCC RHEAs have shown limited room temperature ductility, let alone ductility at 77 K, some display cryogenic ductility by either a lack of a ductile-to-brittle transformation or by new activation of multiple deformation mechanisms [98-100].

Within the well-known Senkov alloy, Tanaka et al. tensile tested the equiatomic TiZrNbHfTa alloy and showed that its yield stress increased with decreasing temperature in the range 77-750 K [101]. Additionally, they showed that intergranular fracture reduces the ductility of TiZrNbHfTa below 296 K (23 °C) with the material becoming fully brittle at 77 K [101].

In this work, two TiZrNbHfTa-derivative alloys were investigated: the equiweight composition, $Ti_{39}Zr_{20.5}Nb_{20}Hf_{10.5}Ta_{10}$, and a related Zr-rich composition, $Ti_{20.5}Zr_{39}Nb_{20}Hf_{10.5}Ta_{10}$. The second alloy swaps the Ti- and Zr-percentages of the first alloy, while maintaining an equivalent HCP_{eq}:BCC_{eq} ratio. Since zirconium has a shear modulus that is ~25% lower than that of titanium the above exchange facilitates further understanding of the role of shear modulus that was introduced in Chapter 2.

Experimental Methods

Three refractory high entropy alloy compositions were prepared: the equiatomic $Ti_{20}Zr_{20}Nb_{20}Hf_{20}Ta_{20}$, a titanium-rich $Ti_{39}Zr_{20.5}Nb_{20}Hf_{10.5}Ta_{10}$, and a zirconium-rich $Ti_{20.5}Zr_{39}Nb_{20}Hf_{10.5}Ta_{10}$. Each composition was arc-melted under a protective argon atmosphere; where, prior to melting, a Ti-getter was melted and allowed to solidify, in order to remove any residual oxygen from the chamber. The constituent alloying components were then melted and allowed to solidify, before the button was flipped and remelted approximately five times, in order to ensure homogeneity and complete melting of all components. Each alloy was then drop-cast into a 1” x 2” copper mold placed under the arc-melting hearth within the Ar-filled melting and casting chamber. In order to ensure compositional and structural homogeneity, a phase diagram was calculated to help in the selection of homogenization and recrystallization temperatures (Figure 3.1). Homogenization was carried out in the single-phase BCC region at 1200°C for 24 h, in sealed argon-filled quartz capsules followed by water quenching. Subsequently, the ingots were split to remove any casting porosity, and ground to remove any scale or

surface oxide. Each ingot was then cold-rolled to ~80% thickness reduction, and re-encapsulated in quartz, under argon. Recrystallization was done at 1100°C, for 15 minutes, based on prior experience.

Samples for microstructural characterization were mounted in epoxy, then metallographically ground and polished using standard techniques. Crystal structure and phase identification was performed using X-ray diffraction with Cu-Kα radiation on a

Malvern Panalytical Empyrean; analysis of this data used Malvern Panalytical's HighScore software suite. Scanning electron microscopy and energy dispersive X-ray spectroscopy (EDS) were used to determine the chemical homogeneity of each sample with a 20 kV accelerating voltage, as well as to identify any phases that might be below the XRD detection limits.

Room temperature elastic constants were determined using resonant ultrasound spectroscopy, shown in Figure 3.2, using a frequency range of 100 to 1500 kHz. Temperature-dependent measurements were made using an RUS-transducer probe inserted into a PPMS Versalab, across a similar frequency range. Analysis was done using the RPR geometry Labview program from Alamo Creek Engineering, with a RMS error for each fit of less than 0.5%.

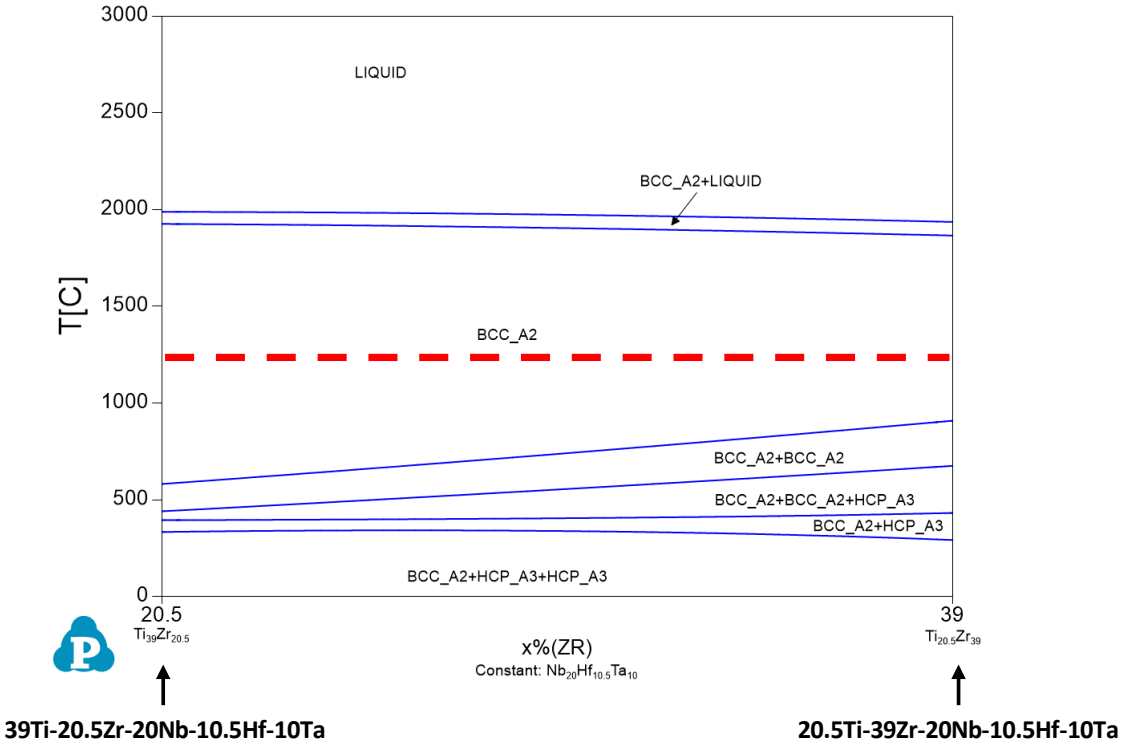

Figure 3.1. The calculated phase diagram for the Ti-Zr-Hf-Nb-Ta system between the compositions of 39Ti-20.5Zr-20Nb-10.5Hf-10Ta and 20.5Ti-39Zr-20Nb-10.5Hf-10Ta. Along the x-axis, the at% of Zr increases from left to right following the expression (39- x)Ti-(20.5+x)Zr-20Nb-10.5Hf-10Ta. The dashed red line represents the chosen homogenization temperature of 1200°C.

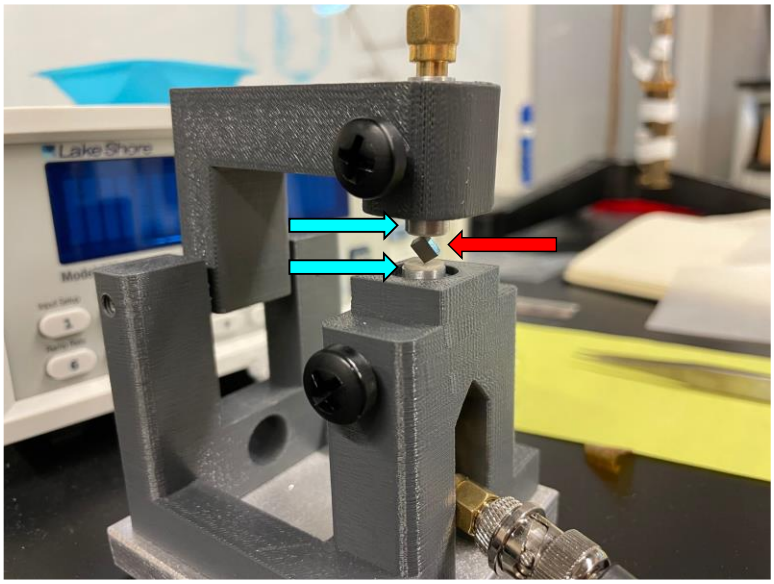

Figure 3.2. Room-temperature resonant ultrasound spectroscopy instrument. The rectangular parallelepiped sample (red arrow) can be seen balanced on two, opposing corners between the transducers (blue arrows).

Mechanical property specimens were cut using wire-EDM, with the rolling direction parallel to the length of the dog bone tensile bar. Tensile testing (n=3) was performed at an initial strain rate of 10^{-3} s^{-1} on an Instron 5900R, at two different temperatures: ~293 K (room temperature), and 77 K (liquid nitrogen bath). Strain was measured by correcting the crosshead displacement with gauge markers on individual tensile bars, in order to remove machine compliance.

Results and Discussion

In order to minimize the effect of grain size and crystal structure on the mechanical properties of the recrystallized tensile bars, grain sizes were kept nominally the same and the alloys all had a single-phase BCC crystal structure, as shown in Figure 3.3. Representative engineering stress-strain curves of the three alloys at the two test temperatures are shown in Figure 3.4. All of them showed little to no work hardening and their yield strengths increased as the test temperature decreased from 293 K to 77 K. At both temperatures, the equiatomic alloy was stronger than the two off-equiatomic alloys. Relative to their concentrations in the equiatomic alloy, an increase in the Ti concentration decreased the strength of the off-equiatomic alloys more than the same increase in the Zr concentration. Broadly speaking, elongations to fracture decreased as the yield strength increased, with the following exceptions: (a) the two off-equiatomic alloys (Ti-rich and Zr-rich) had comparable elongations to fracture at room temperature despite their different strengths, and (b) the Ti-rich composition maintained similar

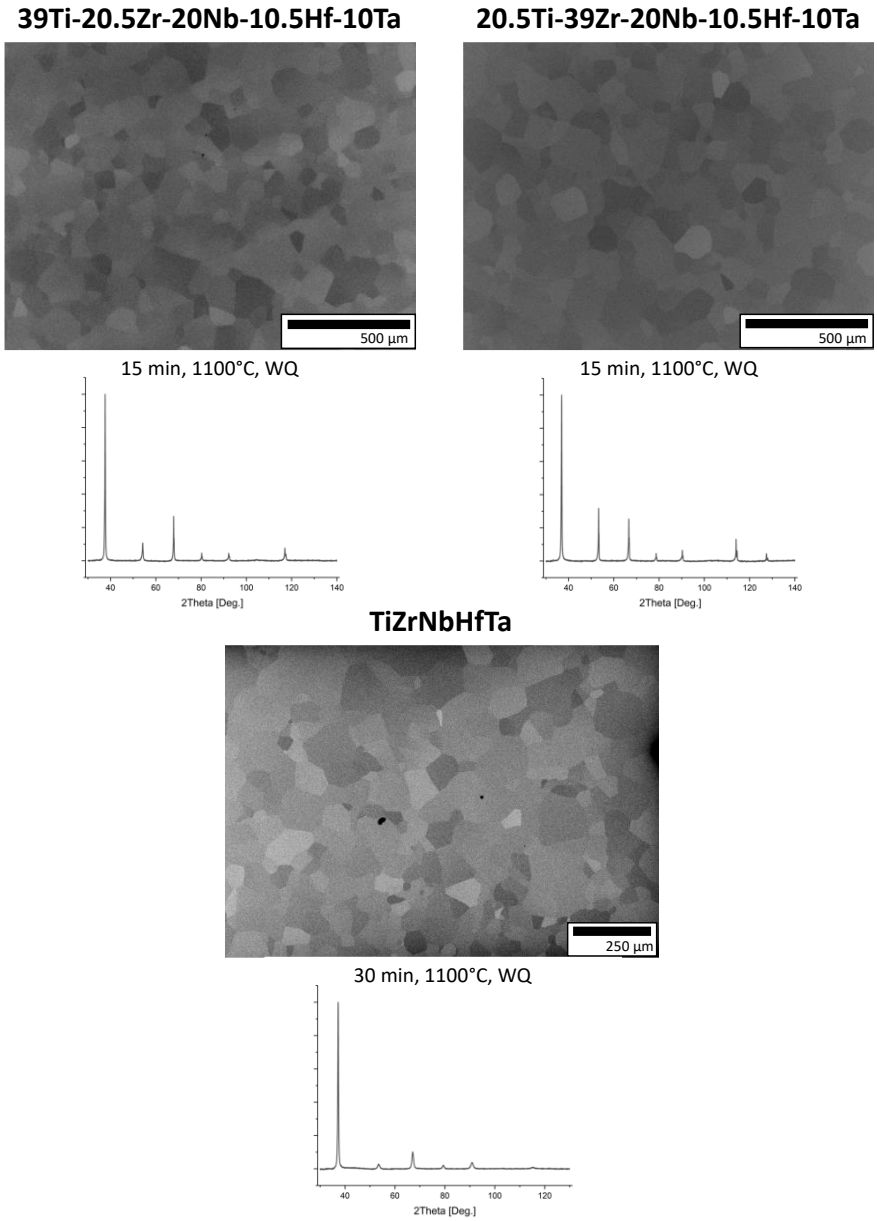

Figure 3.3. SEM backscatter images and XRD patterns of the recrystallized alloys. Grain sizes are nominally the same and XRD indicates a single-phase BCC crystal structure. For ease of comparison, the microstructure and XRD pattern of the equiatomic alloy previously seen in Figure 2.10 is shown again here.

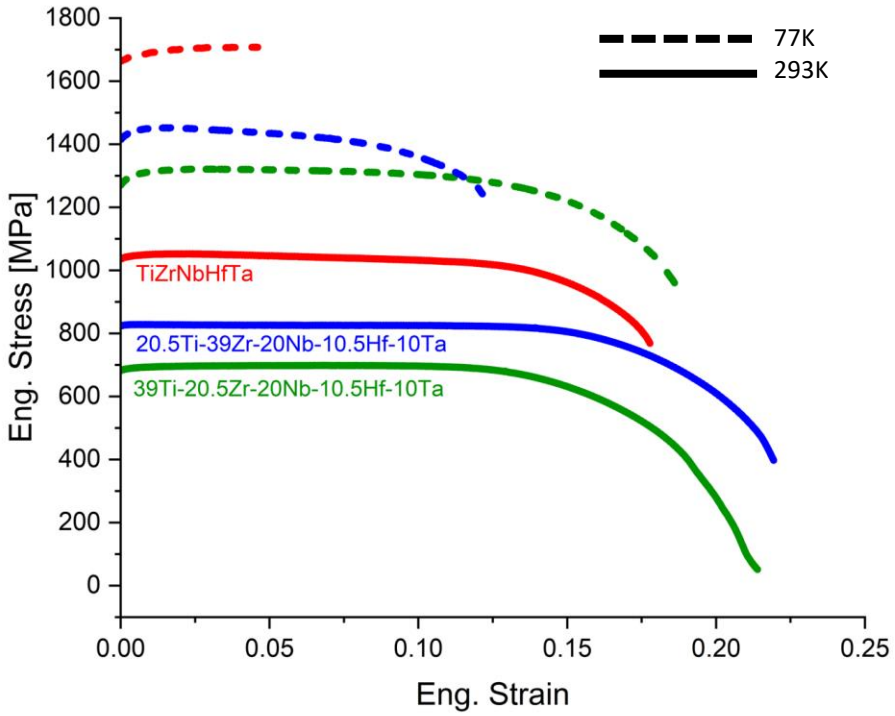

Figure 3.4. Representative engineering stress-strain curves of the Ti-rich, Zr-rich and equiatomic compositions tested at room-temperature (293 K) and liquid nitrogen temperature (77 K).

.

fracture elongations at 77 K and 293K: 18.1% ± 1.6% and 20.2% ± 1.3%. These results are summarized in **Error! Not a valid bookmark self-reference.**.

After normalizing the room-temperature yield strengths, the 39Ti composition had a lower normalized strength due to its lower yield strength and shear modulus (Figure 3.5).

XRD patterns from the gauge sections of the fractured tensile bars, Figure 3.6, showed no evidence of phase transformation. The fracture surfaces, shown in Figure 3.7 and Figure 3.8, are consistent with the tensile behavior of the three alloys: the Ti- and Zr-rich compositions displayed macroscopic necking and void formation at 77 K and 293 K, while the equiatomic alloy displayed more brittle features at 77 K.

Considering the ductility criteria introduced in Chapter 2, we see opposite trends in Figure 3.9 and Figure 3.10. Whereas previously, the highest ductility was seen at the border of the ductile and brittle region, that is not the case here. This suggests that these predictors may be better at screening for whether an alloy is ductile or brittle, rather than for the magnitude of ductility.

Summary

The tensile behavior of two off-equiatomic alloys (Ti-rich and Zr-rich) were compared to the equiatomic TiZrHfNbTa alloy at 293 K and 77 K. While some results were expected, such as increased shear moduli and yield stress with decreased temperature; the low temperature ductility of the Ti-rich, equiweight, composition was unexpected.

Table 3.1. The tabulated mechanical properties for the three tested compositions, with an emphasis placed on the ductility of the Ti-rich alloy at cryogenic- and room-temperatures.

	σ_{yield} [MPa]		$\varepsilon_{fracture}$ [%]	
	77K	**293K**	**77K**	**293K**
TiZrNbHfTa	1651 ± 9	1033 ± 6	6.0 ± 1.3	14.7 ± 2.8
20.5Ti-39Zr-20Nb-10.5Hf-10Ta	1407 ± 8	831 ± 7	12.9 ± 0.5	19.7 ± 3.6
39Ti-20.5Zr-20Nb-10.5Hf-10Ta	1274 ± 8	677 ± 7	18.1 ± 1.6	20.2 ± 1.3

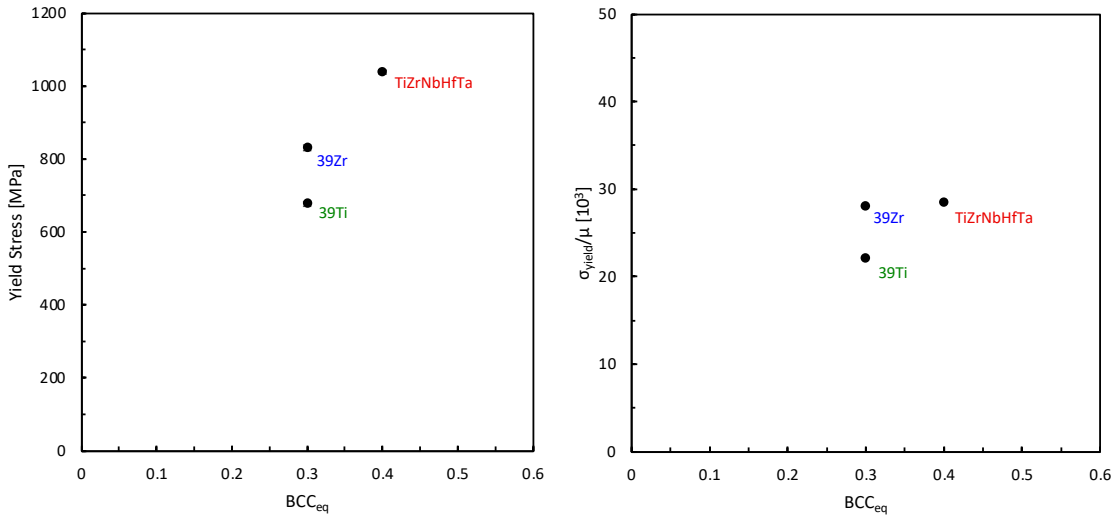

Figure 3.5. When yield strength is plotted against the BCC_{eq} (left), the same general trend occurs with increasing BCC_{eq} leading to a higher yield strength. When the yield stress is normalized by the shear modulus (right), the equiatomic and 39Zr compositions are roughly equal; the 39Ti composition is slightly lower due to its low yield stress, while having a similar shear modulus to the 39Zr composition.

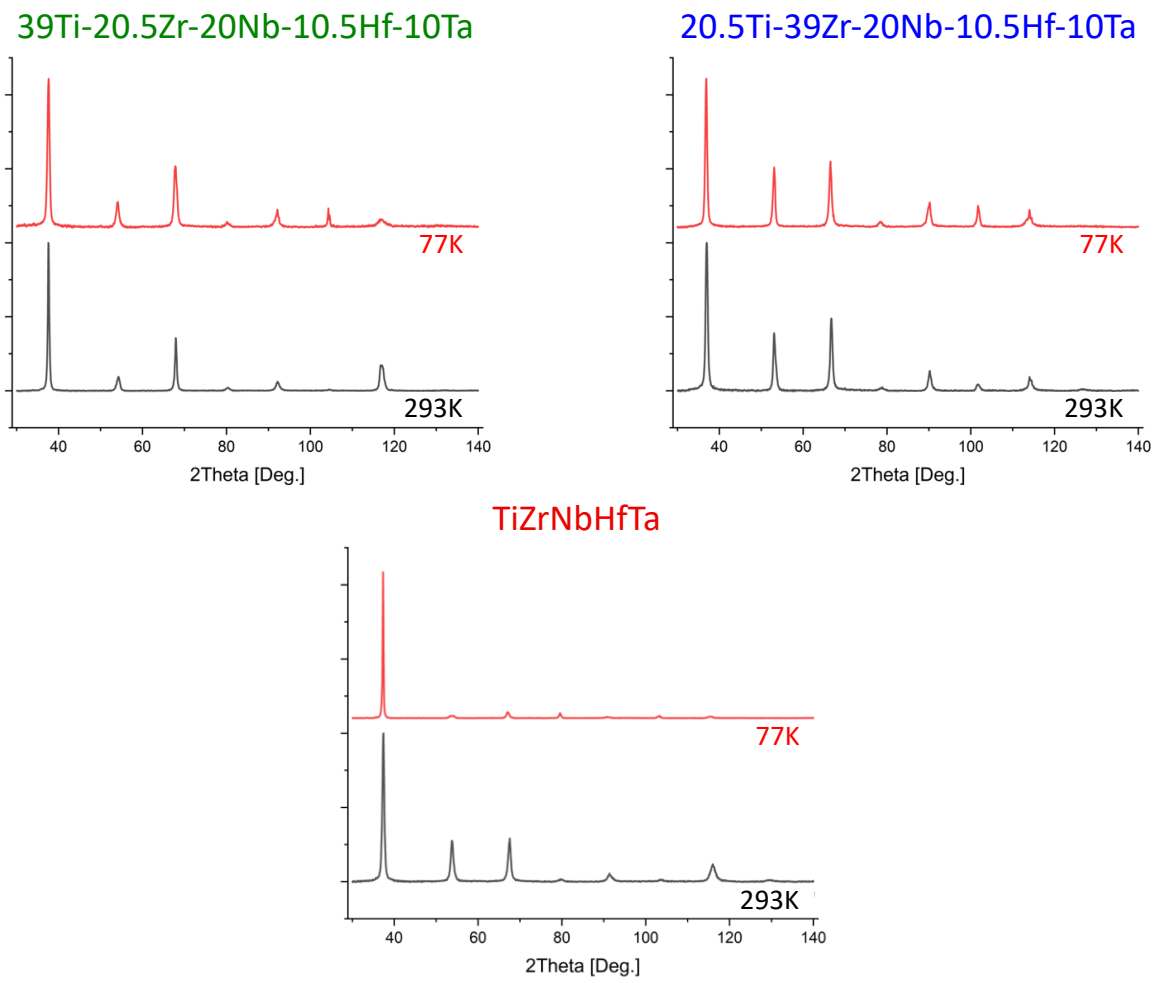

Figure 3.6. Post-fracture XRD shows no deformation- or temperature-induced phase transformation within the gauge section of the tensile bar.

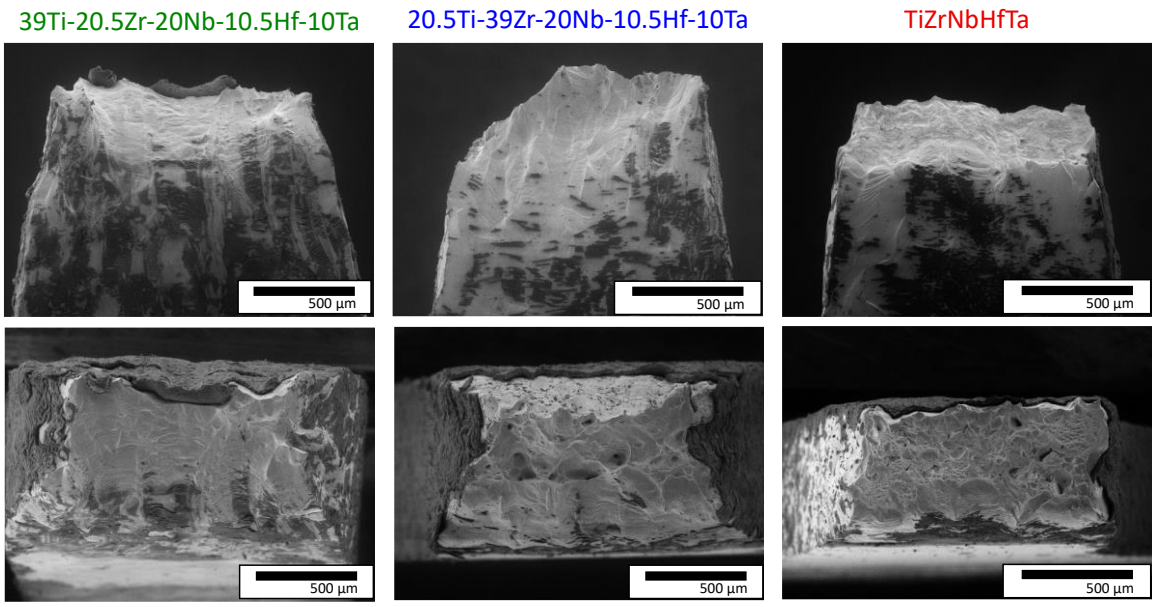

Figure 3.7. Fracture surfaces of the investigated alloys at 293K show ductile features such as necking and void formation.

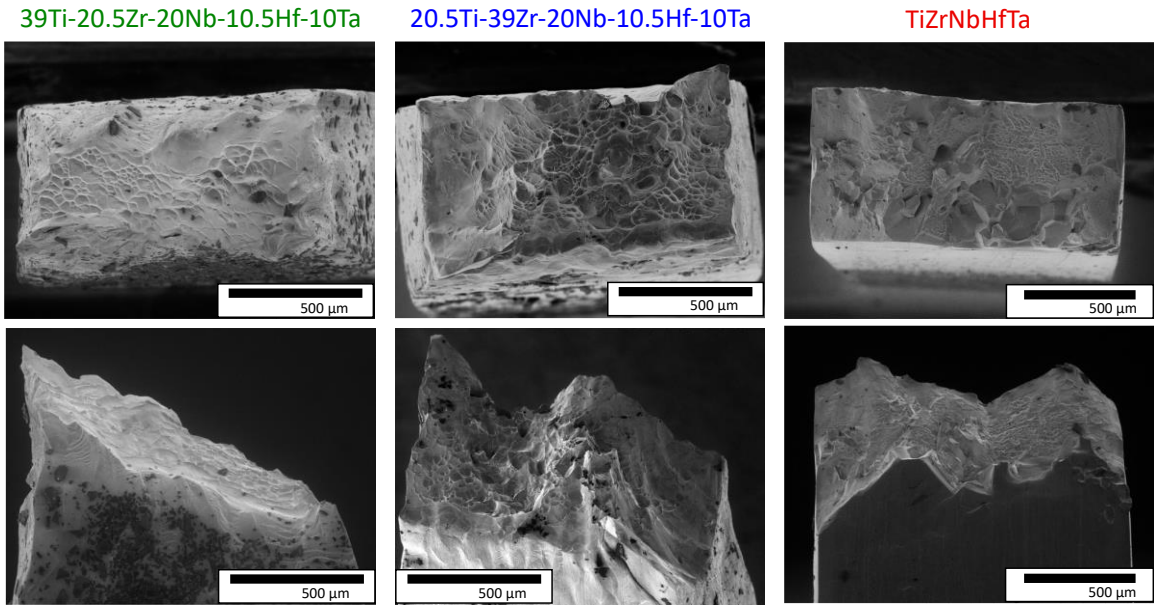

Figure 3.8. Fracture surfaces of the investigated alloys at 77 K show that the Ti- and Zr-rich alloys retain ductile features, while the equiatomic alloy loses its macroscopic necking and displays some cleavage, consistent with its tensile behavior.

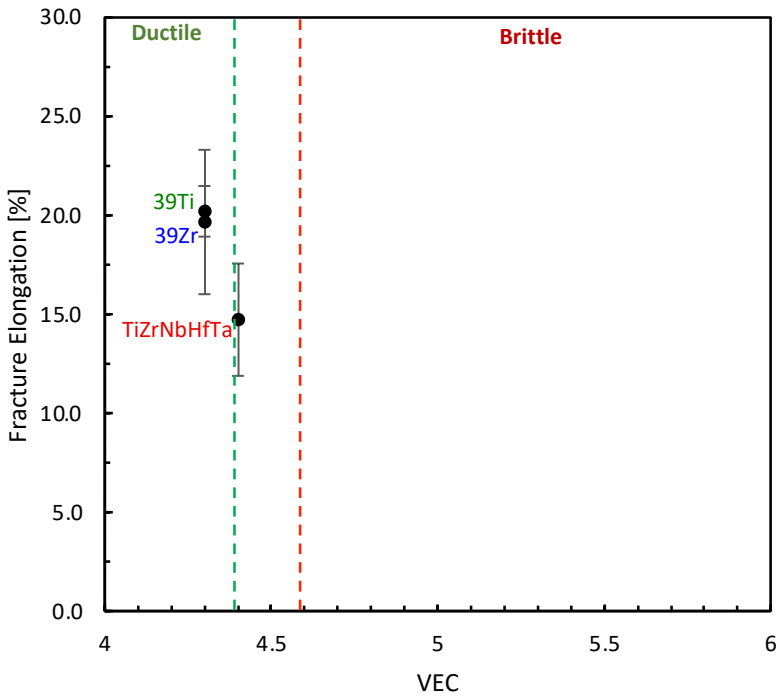

Figure 3.9. The calculated VEC of the studied compositions plotted against their fracture elongation, showing a different trend than seen in Figure 2.15.

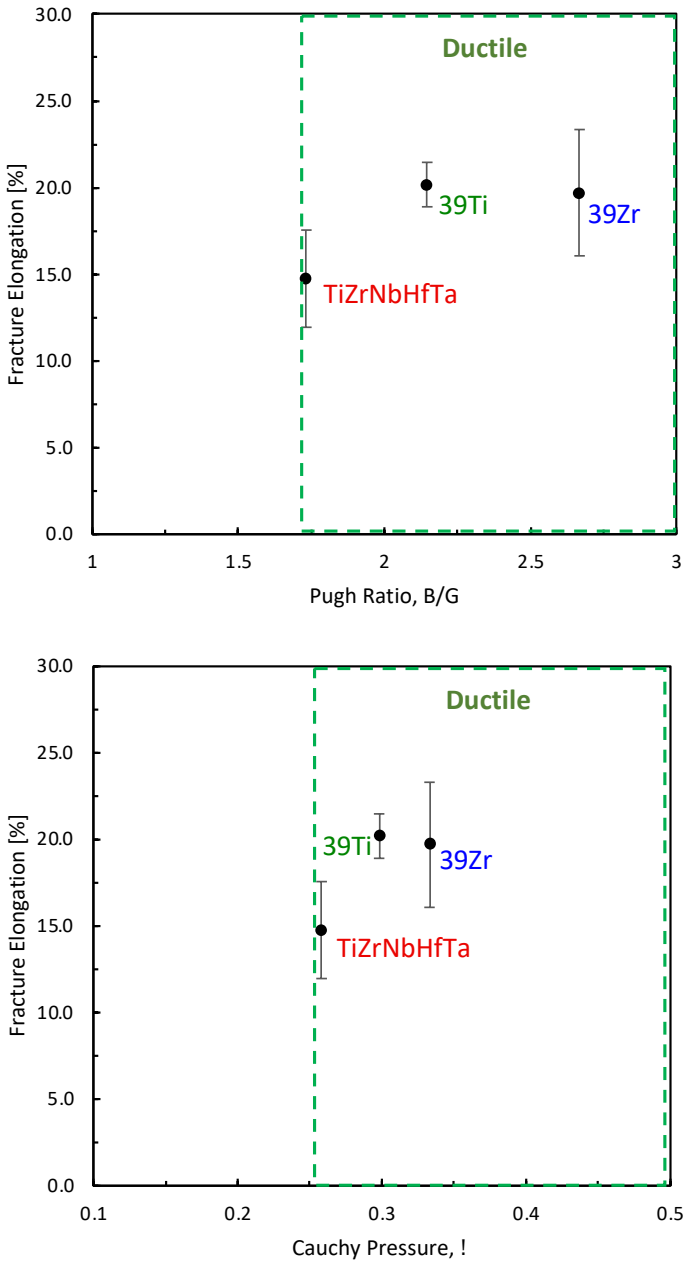

Figure 3.10. The Pugh ratio (top) and Cauchy pressure criteria (bottom) for each of the investigated alloys show that the highest ductility composition falls between the other two, showing that these criteria might predict ductile/brittle, but not magnitude.

Chapter 4

Recommendations for Future Work

Chapter 1

Pushing the limits on time-temperature

In this work, the lower temperatures were allowed a significant amount of time to reach equilibrium, due to the expected low driving force for growth. However, at higher temperatures, there is an expectedly low nucleation rate when considering Figure 1.1 as a TTT diagram. Therefore, longer times at higher temperatures would be necessary to rule out high temperature phase transformations.

Enhanced characterization for lower volume fraction detection and refinement

Given the prevalence of beamline mail-in programs, robotic sample changers, and high-resolution pattern collection; an excellent follow-up study would be to powder each specimen and collect high-resolution diffraction data. This could not only help separate overlapping peaks, but could also shine a light on other difficult to detect phases, especially ordered ones such as B2.

Exploration into higher T_m alloys

As investigators look to replace the current generation of superalloys, refractory high entropy alloys appear to be a promising choice. However, as shown by Gadelmeier et al., the equiatomic TiZrNbHfTa lacks the creep strength and phase stability to be a perfect candidate [68]. Therefore, since the leading asset of RHEAs are their comparatively

higher melting temperatures, pushing the T_m to the limit could be a technically-challenging project to design a suitable BCC matrix, prior to precipitation-strengthening.

Chapter 2

Investigation into the NbTa-rich side of the pseudobinary

Several trends were shown with increased Ta_{eq} fraction, especially in the areas of ductility criteria. While investigating higher T_m compositions is not a trivial task, it is important to see if they are able to break the trend lines shown, while remaining ductile.

Advanced processing for TRIP-likely compositions

In this work, an 80% reduction in thickness was held as a metric of workability for grain size control, via cold-rolling. Therefore, when the $Ta_{eq}0.1$ composition cracked at roughly half of that, it was excluded from further processing. However, work separately done by Lilensten and Wang show that TRIP can occur in $Ti_{35}Zr_{27.5}Nb_5Hf_{27.5}Ta_5$ and $Ti_{50}Zr_{30}Hf_{10}Nb_{10}$ compositions; following the $Ta_{eq}0.1$ cutoff [8, 102]. They additionally showed that the TRIP can take different crystallographic pathways, BCC – Orthorhombic and BCC – HCP [8, 102]. Investigations into hot-rolling or other non-ambient temperature processing techniques, could be valuable for researchers looking to thermomechanically process their specimens. Additionally, this work may help bridge the gap between lab-scale research and commercially-viable alloys. Therefore, this could be an exciting possibility to not only explore the relative elemental effects on TRIP, but also

gives an opportunity to optimize ductility and toughness using a combined series of structural transformations.

Chapter 3

Investigation into the ductility mechanism for the Ti-rich composition

Despite the lack of work-hardening, EBSD and/or TEM should be used to investigate the post-fracture microstructure for twinning. As previously reported, at 77K, titanium has a higher twined volume fraction when compared to zirconium [103]. Otherwise, it is possible that the ductile-to-brittle transition temperature is below 77K for this composition.

Optimization of the Ti-rich composition using factorial design

Given the number of components in the alloy compositions, it is likely that ductility has not been maximized. Therefore, to explore this with the minimum number of cast alloys, I propose a screening design of experiments (DoE) investigating variations around the Ti-rich composition. By choosing to fix certain parameters, either BCC_{eq} or fixing elemental percentages, a DoE can be created to guide the experiments towards a local or global maximum.

Identification of local and global maximums and minimums

Given the number of components and potential combinations, it is unlikely that a desired property, be it yield stress or ductility, can be reached at the first compositional stab in

the dark. Therefore, careful experimental design can be used to identify critical interactions between factors, such as ratios between elements. The collection of this data could then be used to either simplify the experimental space, or to develop a “slope” of sorts to guide the next compositional choices. Ideally, given the size of the high entropy alloy space, a large factorial-style design could be created and split between research teams; provided that care is taken to collect data of similar quality. Better yet, would be to split groups into their greatest strengths: synthesis, thermomechanical processing, mechanical properties, etc, to ensure all conditions remain relatively equivalent.

List of References

1. Cretu, C. and E. van der Lingen, *Coloured gold alloys.* Gold Bulletin, 1999. **32**(4): p. 115-126.
2. Radivojevic, M., et al., *Tainted ores and the rise of tin bronzes in Eurasia, c. 6500 years ago.* Antiquity, 2013. **87**(338): p. 1030-1045.
3. Kato, M., *The Production of Ultrahigh-Purity Copper for Advanced Applications.* Journal of the Minerals Metals & Materials Society, 1995. **47**(12): p. 44-46.
4. Yeh, J.W., et al., *Nanostructured high-entropy alloys with multiple principal elements: Novel alloy design concepts and outcomes.* Advanced Engineering Materials, 2004. **6**(5): p. 299-303.
5. Miracle, D.B. and O.N. Senkov, *A critical review of high entropy alloys and related concepts.* Acta Materialia, 2017. **122**: p. 448-511.
6. Yao, M.J., et al., *A novel, single phase, non-equiatomic FeMnNiCoCr high-entropy alloy with exceptional phase stability and tensile ductility.* Scripta Materialia, 2014. **72-73**: p. 5-8.
7. Deng, Y., et al., *Design of a twinning-induced plasticity high entropy alloy.* Acta Materialia, 2015. **94**: p. 124-133.
8. Lilensten, L., et al., *Design and tensile properties of a bcc Ti-rich high-entropy alloy with transformation-induced plasticity.* Materials Research Letters, 2017. **5**(2): p. 110-116.

9. Ranganathan, S., *Alloyed pleasures: Multimetallic cocktails.* Current Science, 2003. **85**(10): p. 1404-1406.

10. Zhang, C., et al., *Computational Thermodynamics Aided High-Entropy Alloy Design.* Jom, 2012. **64**(7): p. 839-845.

11. Gali, A. and E.P. George, *Tensile properties of high- and medium-entropy alloys.* Intermetallics, 2013. **39**: p. 74-78.

12. Cantor, B., et al., *Microstructural development in equiatomic multicomponent alloys.* Materials Science and Engineering a-Structural Materials Properties Microstructure and Processing, 2004. **375**: p. 213-218.

13. Otto, F., et al., *Relative effects of enthalpy and entropy on the phase stability of equiatomic high-entropy alloys.* Acta Materialia, 2013. **61**(7): p. 2628-2638.

14. Wu, Z., et al., *Temperature dependence of the mechanical properties of equiatomic solid solution alloys with face-centered cubic crystal structures.* Acta Materialia, 2014. **81**: p. 428-441.

15. Hume-Rothery, W. and H.M. Powell, *On the theory of super-lattice structures in alloys.* Zeitschrift Fur Kristallographie, 1935. **91**(1): p. 23-47.

16. Hume-Rothery, W., *Atomic Theory for Students of Metallurgy*. 1969, London: The Institute of Metals.

17. Yang, X. and Y. Zhang, *Prediction of high-entropy stabilized solid-solution in multi-component alloys.* Materials Chemistry and Physics, 2012. **132**(2-3): p. 233-238.

18. Guo, S., et al., *More than entropy in high-entropy alloys: Forming solid solutions or amorphous phase.* Intermetallics, 2013. **41**: p. 96-103.

19. Wang, Z.J., et al., *Atomic-size effect and solid solubility of multicomponent alloys.* Scripta Materialia, 2015. **94**: p. 28-31.

20. Gao, M.C., et al., *Thermodynamics of concentrated solid solution alloys.* Current Opinion in Solid State & Materials Science, 2017. **21**(5): p. 238-251.

21. Gorsse, S. and F. Tancret, *Current and emerging practices of CALPHAD toward the development of high entropy alloys and complex concentrated alloys.* Journal of Materials Research, 2018. **33**(19): p. 2899-2923.

22. Chen, W., et al., *A map of single-phase high-entropy alloys.* Nature Communications, 2023. **14**(1):2856.

23. Dewangan, S.K., et al., *A review on High-Temperature Applicability: A milestone for high entropy alloys.* Engineering Science and Technology-an International Journal-Jestech, 2022. **35**:101211.

24. Vaidya, M., et al., *Ni tracer diffusion in CoCrFeNi and CoCrFeMnNi high entropy alloys.* Journal of Alloys and Compounds, 2016. **688**: p. 994-1001.

25. Balyakin, I.A. and A.A. Rempel, *Atomistic Calculation of the Melting Point of the High-Entropy Cantor Alloy CoCrFeMnNi.* Doklady Physical Chemistry, 2022. **502**(1): p. 11-17.

26. Naik, S., *Basic Aspects of Gas Turbine Heat Transfer*, in *Heat Exchangers: Design, Experiment and Simulation*, S.M.S.L. Murshed, Manuel Matos, Editor. 2017, InTech: Croatia. p. 111-142.

27. Xu, L., et al., *Development Trend of Cooling Technology for Turbine Blades at Super-High Temperature of above 2000 K.* Energies, 2023. **16**(2):668.

28. Szczotok, A., R. Przeliorz, and Iop. *Phase transformations in CMSX-4 nickel-base superalloy*. in *Conference on Technologies and Properties of Modern Utilised Materials (TPMUM)*. 2012. Katowice, Poland: Iop Publishing Ltd.

29. Otto, F., et al., *The influences of temperature and microstructure on the tensile properties of a CoCrFeMnNi high-entropy alloy.* Acta Materialia, 2013. **61**(15): p. 5743-5755.

30. Liu, D., et al., *Exceptional fracture toughness of CrCoNi-based medium- and high-entropy alloys at 20 kelvin.* Science, 2022. **378**(6623): p. 978-983.

31. Zhong, W.C., et al., *Deciphering the multiple deformation mechanisms responsible for sustained work hardening in a FeCrCoNi medium entropy alloy.* International Journal of Plasticity, 2023. **167**:103663.

32. Li, Z.M., et al., *Metastable high-entropy dual-phase alloys overcome the strength-ductility trade-off.* Nature, 2016. **534**(7606): p. 227-230.

33. Chen, S.J., et al., *Real-time observations of TRIP-induced ultrahigh strain hardening in a dual-phase CrMnFeCoNi high-entropy alloy.* Nature Communications, 2020. **11**(1):826.

34. Bönisch, M., Y. Wu, and H. Sehitoglu, *Twinning-induced strain hardening in dual-phase FeCoCrNi$Al_{0.5}$ at room and cryogenic temperature.* Scientific Reports, 2018. **8**: p. 9:10663.

35. Niu, C.N., et al., *Magnetically-driven phase transformation strengthening in high entropy alloys.* Nature Communications, 2018. **9**:1363.

36. Su, J., et al., *Deformation-driven bidirectional transformation promotes bulk nanostructure formation in a metastable interstitial high entropy alloy.* Acta Materialia, 2019. **167**: p. 23-39.

37. Lu, W.J., et al., *Bidirectional Transformation Enables Hierarchical Nanolaminate Dual-Phase High-Entropy Alloys.* Advanced Materials, 2018. **30**(44):1804727.

38. Li, J., et al., *Transformation induced softening and plasticity in high entropy alloys.* Acta Materialia, 2018. **147**: p. 35-41.

39. Feng, R., et al., *Phase stability and transformation in a light-weight high-entropy alloy.* Acta Materialia, 2018. **146**: p. 280-293.

40. George, E.P., D. Raabe, and R.O. Ritchie, *High-entropy alloys.* Nature Reviews Materials, 2019. **4**(8): p. 515-534.

41. Yan, D.L., et al., *Microstructures, Mechanical Properties, and Corrosion Behaviors of Refractory High-Entropy ReTaWNbMo Alloys.* Journal of Materials Engineering and Performance: p. 399-409.

42. Senkov, O.N., et al., *Refractory high-entropy alloys.* Intermetallics, 2010. **18**(9): p. 1758-1765.

43. Senkov, O.N., et al., *Microstructure and room temperature properties of a high-entropy TaNbHfZrTi alloy.* Journal of Alloys and Compounds, 2011. **509**(20): p. 6043-6048.

44. Senkov, O.N., et al., *Development and exploration of refractory high entropy alloys-A review.* Journal of Materials Research, 2018. **33**(19): p. 3092-3128.

45. Senkov, O.N. and S.L. Semiatin, *Microstructure and properties of a refractory high-entropy alloy after cold working.* Journal of Alloys and Compounds, 2015. **649**: p. 1110-1123.

46. Schuh, B., et al., *Thermodynamic instability of a nanocrystalline, single-phase TiZrNbHfTa alloy and its impact on the mechanical properties.* Acta Materialia, 2018. **142**: p. 201-212.

47. Chen, S.Y., et al., *Grain growth and Hall-Petch relationship in a refractory HfNbTaZrTi high-entropy alloy.* Journal of Alloys and Compounds, 2019. **795**: p. 19-26.

48. Yao, J.Q., et al., *Phase stability of a ductile single-phase BCC Hf0.5Nb0.5Ta0.5Ti1.5Zr refractory high-entropy alloy.* Intermetallics, 2018. **98**: p. 79-88.

49. Senkov, O.N., P. Tsakiropoulos, and J.P. Couzinié, *Special Issue "Advanced Refractory Alloys": Metals, MDPI.* Metals, 2022. **12**(2):333.

50. Vellios, N., P. Keating, and P. Tsakiropoulos, *On the Microstructure and Properties of the Nb-23Ti-5Si-5Al-5Hf-5V-2Cr-2Sn (at.%) Silicide-Based Alloy-RM(Nb)IC.* Metals, 2021. **11**(11):1868.

51. Lin, C.M., et al., *Effect of Al addition on mechanical properties and microstructure of refractory AlxHfNbTaTiZr alloys.* Journal of Alloys and Compounds, 2015. **624**: p. 100-107.

52. Han, Z.D., et al., *Effect of Ti additions on mechanical properties of NbMoTaW and VNbMoTaW refractory high entropy alloys.* Intermetallics, 2017. **84**: p. 153-157.

53. Liu, Y., et al., *Microstructure and mechanical properties of refractory HfMo0.5NbTiV0.5Six high-entropy composites.* Journal of Alloys and Compounds, 2017. **694**: p. 869-876.

54. Kang, B., et al., *Ultra-high strength WNbMoTaV high-entropy alloys with fine grain structure fabricated by powder metallurgical process.* Materials Science and Engineering a-Structural Materials Properties Microstructure and Processing, 2018. **712**: p. 616-624.

55. Soni, V., et al., *Microstructural Design for Improving Ductility of An Initially Brittle Refractory High Entropy Alloy.* Scientific Reports, 2018. **8**:8816.

56. Chang, S.H., P.T. Lin, and C.W. Tsai, *High-temperature martensitic transformation of CuNiHfTiZr high-entropy alloys.* Scientific Reports, 2019. **9**:19598.

57. Guo, Z.M., et al., *Effect of Si additions on microstructure and mechanical properties of refractory NbTaWMo high-entropy alloys (vol 54, pg 5844, 2019).* Journal of Materials Science, 2019. **54**(13): p. 10077-10077.

58. Senkov, O.N., S. Gorsse, and D.B. Miracle, *High temperature strength of refractory complex concentrated alloys.* Acta Materialia, 2019. **175**: p. 394-405.

59. Wang, M., et al., *y Microstructures and mechanical properties of HfNbTaTiZrW and HfNbTaTiZrMoW refractory high-entropy alloys.* Journal of Alloys and Compounds, 2019. **803**: p. 778-785.

60. Cao, Y.K., et al., *Precipitation behavior and mechanical properties of a hot-worked TiNbTa0.5ZrAl0.5 refractory high entropy alloy.* International Journal of Refractory Metals & Hard Materials, 2020. **86**:105132.

61. Dong, F.Y., et al., *Hot deformation behavior and processing maps of an equiatomic MoNbHfZrTi refractory high entropy alloy.* Intermetallics, 2020. **126**:106921.

62. Gorr, B., et al., *A new strategy to intrinsically protect refractory metal based alloys at ultra high temperatures.* Corrosion Science, 2020. **166**:108475.

63. Manzoni, A.M., et al., *Temperature evolution of lattice misfit in Hf and Mo variations of the Al10Co25Cr8Fe15Ni36Ti6 compositionally complex alloy.* Scripta Materialia, 2020. **188**: p. 74-79.

64. Nguyen, V.T., et al., *Cuboid-like nanostructure strengthened equiatomic Ti-Zr-Nb-Ta medium entropy alloy.* Materials Science and Engineering a-Structural Materials Properties Microstructure and Processing, 2020. **798**:140169.

65. Senkov, O.N., et al., *Microstructure and properties of Nb-Mo-Zr based refractory alloys.* International Journal of Refractory Metals & Hard Materials, 2020. **92**:105321.

66. Tong, Y., et al., *Severe local lattice distortion in Zr- and/or Hf-containing refractory multi-principal element alloys.* Acta Materialia, 2020. **183**: p. 172-181.

67. Wei, Q.Q., et al., *Effect of raw material forms on the microstructure and mechanical properties of MoNbRe0.5TaW high-entropy alloy.* Materials Science and Engineering a-Structural Materials Properties Microstructure and Processing, 2020. **794**:139632.

68. Gadelmeier, C., et al., *Creep strength of refractory high-entropy alloy TiZrHfNbTa and comparison with Ni-base superalloy CMSX-4.* Cell Reports Physical Science, 2022. **3**(8):100991.

69. Pang, J.Y., et al., *High-temperature structural and mechanical stability of refractory high-entropy alloy Nb40Ti25Al15V10Ta5Hf3W2.* Materials Characterization, 2023. **205**:113321.

70. Gao, K., et al., *Phase inversion in a lightweight high Al content refractory high-entropy alloy.* Journal of Materials Science & Technology, 2023. **150**: p. 124-137.

71. Wang, H., et al., *Microstructural evolution and mechanical behavior of novel $Ti_{1.6}ZrNbAl_x$ lightweight refractory high-entropy alloys containing BCC/B2 phases.* Materials Science and Engineering a-Structural Materials Properties Microstructure and Processing, 2023. **885**:145661.

72. Gao, F., et al., *Microstructure and strengthening mechanisms of novel lightweight TiAlV0.5CrMo refractory high-entropy alloy fabricated by mechanical alloying and spark plasma sintering.* Journal of Alloys and Compounds, 2023. **932**:167659.

73. Guo, Z.H., et al., *Microstructure and mechanical properties of Alx(TiZrTa0.7NbMo) refractory high-entropy alloys.* Journal of Alloys and Compounds, 2023. **960**:170739.

74. Xu, T., et al., *Thermal stability and oxidation resistance of non-equimolar ratio AlTiVCrNb refractory high-entropy alloys.* Intermetallics, 2023. **160**:107942.

75. He, H., et al., *Carbide-reinforced Re0.1Hf0.25NbTaW0.4 refractory high-entropy alloy with excellent room and elevated temperature mechanical properties.* International Journal of Refractory Metals & Hard Materials, 2023. **116**:106349.

76. Erickson, G.L., *The development and application of CMSX (R)-10.* Superalloys 1996, 1996: p. 35-44.

77. Guo, S. and C.T. Liu, *Phase stability in high entropy alloys: Formation of solid-solution phase or amorphous phase.* Progress in Natural Science-Materials International, 2011. **21**(6): p. 433-446.

78. Coury, F.G., et al., *Phase equilibria, mechanical properties and design of quaternary refractory high entropy alloys.* Materials & Design, 2018. **155**: p. 244-256.

79. Maiti, S. and W. Steurer, *Structural-disorder and its effect on mechanical properties in single-phase TaNbHfZr high-entropy alloy.* Acta Materialia, 2016. **106**: p. 87-97.

80. *Properties of Haynes 282 Alloy*. [Website] [cited 2022; Available from: https://www.haynesintl.com/alloys/alloy-portfolio_/High-temperature-Alloys/HAYNES282alloy/tensile-properties.aspx.

81. Senkov, O.N., et al., *Microstructure and elevated temperature properties of a refractory TaNbHfZrTi alloy.* Journal of Materials Science, 2012. **47**(9): p. 4062-4074.

82. Villars, P., H. Okamoto, and K. Cenzual, *ASM Alloy Phase Diagram Database*. 2023, ASM International: Materials Park, OH.

83. Senkov, O.N., A.L. Pilchak, and S.L. Semiatin, *Effect of Cold Deformation and Annealing on the Microstructure and Tensile Properties of a HfNbTaTiZr Refractory High Entropy Alloy.* Metallurgical and Materials Transactions a-Physical Metallurgy and Materials Science, 2018. **49A**(7): p. 2876-2892.

84. Lilensten, L., et al., *New structure in refractory high-entropy alloys.* Materials Letters, 2014. **132**: p. 123-125.

85. Huang, H.L., et al., *Phase-Transformation Ductilization of Brittle High-Entropy Alloys via Metastability Engineering.* Advanced Materials, 2017. **29**(30):1701678.

86. Fazakas, E., et al., *Experimental and theoretical study of Ti20Zr20Hf20Nb20X20 (X = V or Cr) refractory high-entropy alloys.* International Journal of Refractory Metals & Hard Materials, 2014. **47**: p. 131-138.

87. Rao, Y., et al., *Theory-guided design of high-strength, high-melting point, ductile, low-density, single-phase BCC high entropy alloys.* Acta Materialia, 2022. **237**: p. 118132.

88. Laplanche, G., et al., *Temperature dependence of elastic moduli in a refractory HfNbTaTiZr high-entropy alloy.* Journal of Alloys and Compounds, 2019. **799**: p. 538-545.

89. Sheikh, S., et al., *Alloy design for intrinsically ductile refractory high-entropy alloys.* Journal of Applied Physics, 2016. **120**(16):164902.

90. Pugh, S.F., *Relations between the elastic moduli and the plastic properties of polycrystalline pure metals.* Philosophical Magazine, 1954. **45**(367): p. 823-843.

91. Pettifor, D.G., *Theoretical predictions of structure and related properties of intermetallics.* Materials Science and Technology, 1992. **8**(4): p. 345-349.

92. Maresca, F. and W.A. Curtin, *Mechanistic origin of high strength in refractory BCC high entropy alloys up to 1900K.* Acta Materialia, 2020. **182**: p. 235-249.

93. Yao, H.W., et al., *Mechanical properties of refractory high-entropy alloys: Experiments and modeling.* Journal of Alloys and Compounds, 2017. **696**: p. 1139-1150.

94. Chen, H., et al., *Contribution of Lattice Distortion to Solid Solution Strengthening in a Series of Refractory High Entropy Alloys.* Metallurgical and Materials Transactions A, 2018. **49**(3): p. 772-781.

95. Baruffi, C., F. Maresca, and W.A. Curtin, *Screw vs. edge dislocation strengthening in body-centered-cubic high entropy alloys and implications for guided alloy design.* MRS Communications, 2022. **12**(6): p. 1111-1118.

96. Koehler, J.S., *On the Dislocation Theory of Plastic Deformation.* Physical Review, 1941. **60**(5): p. 397-410.

97. Gludovatz, B., et al., *A fracture-resistant high-entropy alloy for cryogenic applications.* Science, 2014. **345**(6201): p. 1153-1158.

98. Wen, X., et al., *Strong work-hardenable body-centered-cubic high-entropy alloys at cryogenic temperature.* Scripta Materialia, 2023. **231**: p. 115434.

99. Gao, X., et al., *High-entropy alloys: a review of mechanical properties and deformation mechanisms at cryogenic temperatures.* Journal of Materials Science, 2022. **57**(12): p. 6573-6606.

100. Zhang, Y., X. Yang, and P.K. Liaw, *Alloy Design and Properties Optimization of High-Entropy Alloys.* JOM, 2012. **64**(7): p. 830-838.

101. Tanaka, M., S. Yamasaki, and T. Morikawa, *Temperature dependence of the yield stress in TiZrNbHfTa body-centred cubic high-entropy alloy.* Materials Science and Engineering a-Structural Materials Properties Microstructure and Processing, 2023. **871**:144917.

102. Wang, S.B., et al., *Decreasing Zr content to improve tensile properties of non-equiatomic TiZrHfNb medium entropy alloys with transformation-induced plasticity.* Materials Science and Engineering a-Structural Materials Properties Microstructure and Processing, 2022. **832**:142476.

103. Garde, A.M., E. Aigeltinger, and R. E. Reed-Hill, *Relationship between deformation twinning and the stress-strain behavior of polycrystalline titanium and zirconium at 77 K.* Metallurgical Transactions, 1973(4): p. 2461-2468.

Appendix

Appendix One: Observed Compositional Information from SEM/EDS for Chapter One

TiZrNbHfTa Series

- TiZrNbHfTa
  - As-Cast: Ta-rich, Zr-poor particles in a Zr-rich matrix
  - Homogenized: Single phase
  - 800°C, 300 Days, WQ: Ta-rich precipitates at grain boundaries and in grains
  - 1000°C, 30 Days, WQ: Single phase
  - 1200°C, 3 Days, WQ: Single phase

- TiZrHfNb
  - As-Cast: Single phase
  - Homogenized: Single phase
  - 800°C, 300 Days, WQ: Single phase
  - 1000°C, 30 Days, WQ: Single phase
  - 1200°C, 3 Days, WQ: Single phase

- TiZrHfTa
  - As-Cast: Ta-poor plates
  - Homogenized: Single phase
  - 800°C, 300 Days, WQ: Ta-rich precipitates at grain boundaries and in grains
  - 1000°C, 30 Days, WQ: Single phase
  - 1200°C, 3 Days, WQ: Single phase

- TiZrNbTa
  - As-Cast: Ta-rich dendrites
  - Homogenized: Single phase
  - 800°C, 300 Days, WQ: Ta-rich and Nb-rich phases with depletion zone
  - 1000°C, 30 Days, WQ: ZrNb-rich precipitates at grain boundaries

    - 1200°C, 3 Days, WQ: Single phase

- TiHfNbTa
    - As-Cast: Ta-poor and Ti-rich phase separation
    - Homogenized: Single phase
    - 800°C, 300 Days, WQ: Single phase
    - 1000°C, 30 Days, WQ: Single phase
    - 1200°C, 3 Days, WQ: Single phase

- ZrHfNbTa
    - As-Cast: Ta-poor particles, matrix separation in Ta-rich/Zr-poor areas
    - Homogenized: Single phase
    - 800°C, 300 Days, WQ: TaNb-rich precipitates in ZrHf-rich matrix
    - 1000°C, 30 Days, WQ: Ta-rich precipitates at grain boundaries
    - 1200°C, 3 Days, WQ: Single phase

- TiZrHf
    - As-Cast: Single phase
    - Homogenized: Single phase
    - 800°C, 300 Days, WQ: Angular TiZr-rich precipitates
    - 1000°C, 30 Days, WQ: Single phase
    - 1200°C, 3 Days, WQ: Single phase

- TiZrNb
    - As-Cast: Single phase
    - Homogenized: Single phase
    - 800°C, 300 Days, WQ: Single phase
    - 1000°C, 30 Days, WQ: Single phase
    - 1200°C, 3 Days, WQ: Single phase

- TiZrTa
    - As-Cast: Ta-rich dendrites in TiZr-rich matrix
    - Homogenized: Ta-rich precipitates at grain boundaries
    - 800°C, 300 Days, WQ: Large Ta-rich precipitates at grain boundaries surrounded by a Ta-poor depletion zone, with small Ta-rich clusters

    - 1000°C, 30 Days, WQ: Large Ta-rich precipitates at grain boundaries surrounded by a Ta-poor depletion zone, with small Ta-rich clusters
    - 1200°C, 3 Days, WQ: Single phase

- TiHfNb
    - As-Cast: Single phase
    - Homogenized: Single phase
    - 800°C, 300 Days, WQ: Single phase
    - 1000°C, 30 Days, WQ: Single phase
    - 1200°C, 3 Days, WQ: Single phase

- TiHfTa
    - As-Cast: Single phase
    - Homogenized: Single phase
    - 800°C, 300 Days, WQ: Single phase
    - 1000°C, 30 Days, WQ: Single phase
    - 1200°C, 3 Days, WQ: Single phase

- TiNbTa
    - As-Cast: Ta-rich dendrites in TiNb-rich matrix
    - Homogenized: Ta-rich dendrites in TiNb-rich matrix
    - 800°C, 300 Days, WQ: Ta-rich dendrites in TiNb-rich matrix
    - 1000°C, 30 Days, WQ: Ta-rich dendrites in TiNb-rich matrix
    - 1200°C, 3 Days, WQ: Ta-rich dendrites in TiNb-rich matrix

- ZrHfNb
    - As-Cast: Single phase
    - Homogenized: Single phase
    - 800°C, 300 Days, WQ: Single phase
    - 1000°C, 30 Days, WQ: Single phase
    - 1200°C, 3 Days, WQ: Single phase

- ZrHfTa
    - As-Cast: Single phase
    - Homogenized: Ta-rich precipitates

- 800°C, 300 Days, WQ: Ta-rich precipitates at grain boundaries and in grains
- 1000°C, 30 Days, WQ: Ta-rich precipitates at grains boundaries and in grains
- 1200°C, 3 Days, WQ: Ta-rich precipitates at grain boundaries and in grains

- ZrNbTa
  - As-Cast: Ta-rich dendrites in ZrNb-rich matrix
  - Homogenized: Ta-rich dendrites in ZrNb-rich matrix
  - 800°C, 300 Days, WQ: Ta-rich dendrites in ZrNb-rich matrix
  - 1000°C, 30 Days, WQ: Ta-rich dendrites in ZrNb-rich matrix
  - 1200°C, 3 Days, WQ: Ta-rich dendrites in ZrNb-rich matrix

- HfNbTa
  - As-Cast: Ta-poor particles
  - Homogenized: Single phase
  - 800°C, 300 Days, WQ: Contrast at grain boundaries
  - 1000°C, 30 Days, WQ: Single phase
    1200°C, 3 Days, WQ: Single phase

- TiZr
  - As-Cast: Single phase
  - Homogenized: Single phase
  - 800°C, 300 Days, WQ: Single phase
  - 1000°C, 30 Days, WQ: Single phase
  - 1200°C, 3 Days, WQ: Single phase

- TiHf
  - As-Cast: Single phase
  - Homogenized: Single phase
  - 800°C, 300 Days, WQ: Ti-rich precipitates
  - 1000°C, 30 Days, WQ: Line of Ti-poor precipitates
  - 1200°C, 3 Days, WQ: Single phase

- TiNb

    - As-Cast: Single phase
    - Homogenized: Single phase
    - 800°C, 300 Days, WQ: Ti-rich precipitates at grain boundaries
    - 1000°C, 30 Days, WQ: Single phase
    - 1200°C, 3 Days, WQ: Single phase

- TiTa
    - As-Cast: Ti-rich borders surrounding Ta-rich grains
    - Homogenized: Single phase
    - 800°C, 300 Days, WQ: Single phase
    - 1000°C, 30 Days, WQ: Single phase
    - 1200°C, 3 Days, WQ: Single phase

- ZrHf
    - As-Cast: Single phase
    - Homogenized: Single phase
    - 800°C, 300 Days, WQ: Single phase
    - 1000°C, 30 Days, WQ: Single phase
    - 1200°C, 3 Days, WQ: Single phase

- ZrNb
    - As-Cast: Single phase
    - Homogenized: Single phase
    - 800°C, 300 Days, WQ: Nb-rich precipitates
    - 1000°C, 30 Days, WQ: Single phase
    - 1200°C, 3 Days, WQ: Single phase

- ZrTa
    - As-Cast: Ta-rich dendrites in Zr-rich matrix
    - Homogenized: Ta-rich dendrites with spinodal decomposition
    - 800°C, 300 Days, WQ: Ta-rich dendrites with spinodal decomposition
    - 1000°C, 30 Days, WQ: Ta-rich dendrites with spinodal decomposition
    - 1200°C, 3 Days, WQ: Ta-rich dendrites with spinodal decomposition

- HfNb
    - As-Cast: Single phase

- Homogenized: Hf-rich precipitates at grain boundaries
- 800°C, 300 Days, WQ: Hf-rich precipitates at grain boundaries and in grains
- 1000°C, 30 Days, WQ: Hf-rich precipitates at grain boundaries and in grains
- 1200°C, 3 Days, WQ: Hf-rich precipitates at grain boundaries and in grains

- HfTa
  - As-Cast: Single phase
  - Homogenized: Hf-rich precipitates at grain boundaries
  - 800°C, 300 Days, WQ: Hf-rich precipitates
  - 1000°C, 30 Days, WQ: Hf-rich precipitates
  - 1200°C, 3 Days, WQ: Hf-rich precipitates

- NbTa
  - As-Cast: Ta-rich dendrites in Nb-rich matrix
  - Homogenized: Ta-rich dendrites in Nb-rich matrix
  - 800°C, 300 Days, WQ: Ta-rich dendrites in Nb-rich matrix
  - 1000°C, 30 Days, WQ: Ta-rich dendrites in Nb-rich matrix
  - 1200°C, 3 Days, WQ: Single phase

VNbMoTaW Series

- VNbMoTaW
  - As-Cast: V-rich at grain boundaries and precipitates
  - Homogenized: Single phase
  - 800°C, 300 Days, WQ: Single phase
  - 1000°C, 30 Days, WQ: Single phase
  - 1200°C, 3 Days, WQ: Single phase

- VNbMoTa
  - As-Cast: V-rich/Ta-poor inner dendrite spacing
  - Homogenized: Single phase
  - 800°C, 300 Days, WQ: Single phase
  - 1000°C, 30 Days, WQ: Single phase
  - 1200°C, 3 Days, WQ: Single phase

- VNbMoW
    - As-Cast: V-rich/W-poor inner dendrite spacing
    - Homogenized: Single phase
    - 800°C, 300 Days, WQ: Single phase
    - 1000°C, 30 Days, WQ: Single phase
    - 1200°C, 3 Days, WQ: Single phase

- VNbTaW
    - As-Cast: V-rich/TaW-poor inner dendrite spacing
    - Homogenized: Single phase
    - 800°C, 300 Days, WQ: Single phase
    - 1000°C, 30 Days, WQ: Single phase
    - 1200°C, 3 Days, WQ: Single phase

- VMoTaW
    - As-Cast: TaW-rich dendrites in V-rich matrix
    - Homogenized: TaW-rich dendrites in V-rich matrix
    - 800°C, 300 Days, WQ: Single phase
    - 1000°C, 30 Days, WQ: Single phase
    - 1200°C, 3 Days, WQ: Single phase

- NbMoTaW
    - As-Cast: TaW-rich dendrites in Nb-rich matrix
    - Homogenized: TaW-rich dendrites in Nb-rich matrix
    - 800°C, 300 Days, WQ: Single phase
    - 1000°C, 30 Days, WQ: Mo-rich areas
    - 1200°C, 3 Days, WQ: TaW-rich dendrites in NbMo-rich matrix

- VNbMo
    - As-Cast: V-rich inner dendrite spacing
    - Homogenized: Single phase
    - 800°C, 300 Days, WQ: Single phase
    - 1000°C, 30 Days, WQ: Single phase
    - 1200°C, 3 Days, WQ: Single phase

- VNbTa
    - As-Cast: V-rich/Ta-poor inner dendrite spacing
    - Homogenized: Single phase
    - 800°C, 300 Days, WQ: Single phase
    - 1000°C, 30 Days, WQ: Single phase
    - 1200°C, 3 Days, WQ: Single phase

- VNbW
    - As-Cast: V-rich/W-poor inner dendrite spacing
    - Homogenized: Single phase
    - 800°C, 300 Days, WQ: Single phase
    - 1000°C, 30 Days, WQ: Single phase
    - 1200°C, 3 Days, WQ: Single phase

- VMoTa
    - As-Cast: V-rich/Ta-poor inner dendrite spacing
    - Homogenized: Single phase
    - 800°C, 300 Days, WQ: Single phase
    - 1000°C, 30 Days, WQ: Single phase
    - 1200°C, 3 Days, WQ: Single phase

- VMoW
    - As-Cast: W-rich dendrites in V-rich matrix
    - Homogenized: W-rich dendrites in V-rich matrix
    - 800°C, 300 Days, WQ: Multiphase
    - 1000°C, 30 Days, WQ: W-rich dendrites in V-rich matrix
    - 1200°C, 3 Days, WQ: W-depletion at grain boundaries

- NbMoTa
    - As-Cast: Ta-poor borders around NbMo-rich grains
    - Homogenized: Single phase
    - 800°C, 300 Days, WQ: Single phase
    - 1000°C, 30 Days, WQ: Single phase
    - 1200°C, 3 Days, WQ: Single phase

- NbMoW
    - As-Cast: W-rich dendrites in NbMo-rich matrix

    - Homogenized: W-rich dendrites in NbMo-rich matrix
    - 800°C, 300 Days, WQ: W-rich dendrites in NbMo-rich matrix
    - 1000°C, 30 Days, WQ: W-rich dendrites in NbMo-rich matrix
    - 1200°C, 3 Days, WQ: W-rich dendrites in NbMo-rich matrix

- NbTaW
    - As-Cast: W-poor borders around NbTa-rich grains
    - Homogenized: Single phase
    - 800°C, 300 Days, WQ: Single phase
    - 1000°C, 30 Days, WQ: Single phase
    - 1200°C, 3 Days, WQ: Single phase

- MoTaW
    - As-Cast: Single phase
    - Homogenized: Single phase
    - 800°C, 300 Days, WQ: Single phase
    - 1000°C, 30 Days, WQ: Single phase
    - 1200°C, 3 Days, WQ: Single phase

- VNb
    - As-Cast: Nb-rich dendrites in V-rich matrix
    - Homogenized: Single phase
    - 800°C, 300 Days, WQ: Single phase
    - 1000°C, 30 Days, WQ: Single phase
      1200°C, 3 Days, WQ: Single phase

- VMo
    - As-Cast: Mo-rich dendrites in V-rich matrix
    - Homogenized: Single phase
    - 800°C, 300 Days, WQ: Single phase
    - 1000°C, 30 Days, WQ: Single phase
    - 1200°C, 3 Days, WQ: Single phase

- VTa
    - As-Cast: Ta-rich dendrites in V-rich matrix
    - Homogenized: Single phase

- 800°C, 300 Days, WQ: Single phase
- 1000°C, 30 Days, WQ: Single phase
- 1200°C, 3 Days, WQ: Single phase

- VW
  - As-Cast: W-rich dendrites in V-rich matrix
  - Homogenized: W-rich dendrites in V-rich matrix
  - 800°C, 300 Days, WQ: W-rich areas and V-depleted areas from oxide formation
  - 1000°C, 30 Days, WQ: W-rich and V-rich areas
  - 1200°C, 3 Days, WQ: W-rich and V-rich areas

- NbMo
  - As-Cast: Single phase
  - Homogenized: NbO at grain boundaries- Single phase
  - 800°C, 300 Days, WQ: Single phase
  - 1000°C, 30 Days, WQ: NbO at grain boundaries- Single phase
  - 1200°C, 3 Days, WQ: NbO at grain boundaries - Single phase

- NbTa
  - As-Cast: Ta-rich dendrites in Nb-rich matrix
  - Homogenized: Single phase
  - 800°C, 300 Days, WQ: Single phase
  - 1000°C, 30 Days, WQ: Single phase
  - 1200°C, 3 Days, WQ: Single phase

- NbW
  - As-Cast: W-rich dendrites in Nb-rich matrix
  - Homogenized: W-rich dendrites in Nb-rich matrix
  - 800°C, 300 Days, WQ: Single phase
  - 1000°C, 30 Days, WQ: W-rich dendrites in Nb-rich matrix
  - 1200°C, 3 Days, WQ: W-rich dendrites in Nb-rich matrix

- MoTa
  - As-Cast: Single phase
  - Homogenized: Single phase

    - 800°C, 300 Days, WQ: Ta-oxide at grain boundaries
    - 1000°C, 30 Days, WQ: Single phase
    - 1200°C, 3 Days, WQ: Single phase

- MoW
    - As-Cast: Single phase
    - Homogenized: W-rich dendrites in Mo-rich matrix
    - 800°C, 300 Days, WQ: W-rich dendrites in Mo-rich matrix
    - 1000°C, 30 Days, WQ: W-rich dendrites in Mo-rich matrix
    - 1200°C, 3 Days, WQ: W-rich areas in Mo-rich matrix

- TaW
    - As-Cast: Single phase
    - Homogenized: Single phase
    - 800°C, 300 Days, WQ: Single phase
    - 1000°C, 30 Days, WQ: Single phase
    - 1200°C, 3 Days, WQ: Single phase

Appendix Two: Microstructural Images and Compiled XRD Patterns for Chapter One

The following is a compilation of representative SEM (backscattered electrons) images, as well as diffraction patterns, taken from five different conditions. On the diffraction patterns, the color scheme is: homogenized (purple, top), 1200°C/3 Days/WQ (green), 1000°C/30 Days/WQ (blue), 800°C/300 Days/WQ (red), as-cast (black, bottom). Due to the scale of information, these images are presented without scale bars for brevity.

For investigative purposes, images were taken at several magnifications ranging from relatively low-magnification (50-100x) to higher-magnification (1000-3000x). For speed, EDS line scans were used to quickly identify compositional differences.

Ti-Zr-Nb-Hf-Ta

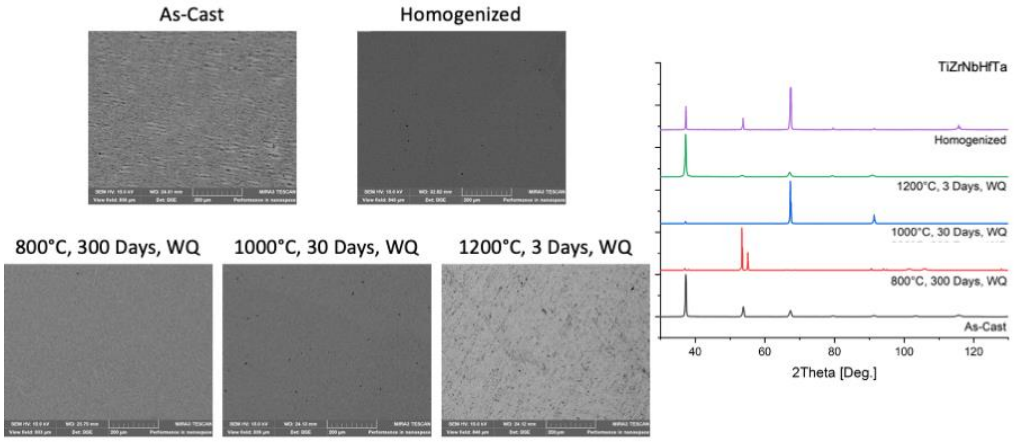

Ti-Zr-Nb-Hf

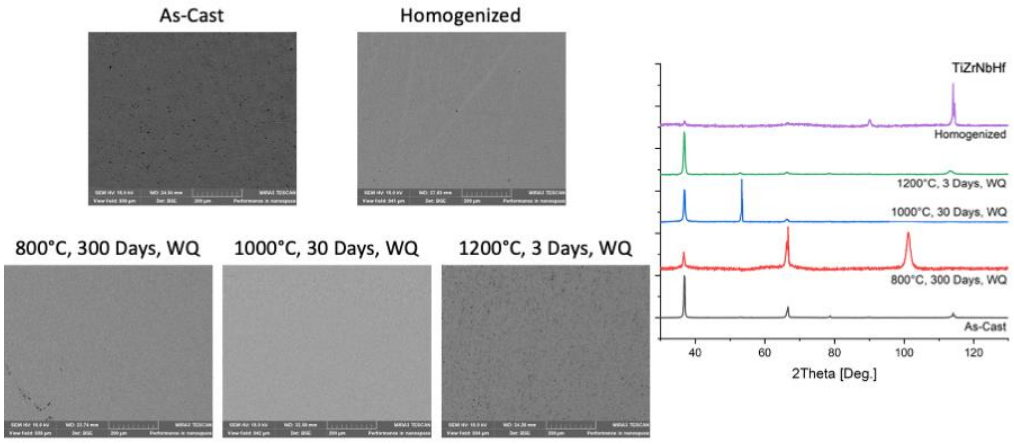

Ti-Zr-Hf-Ta

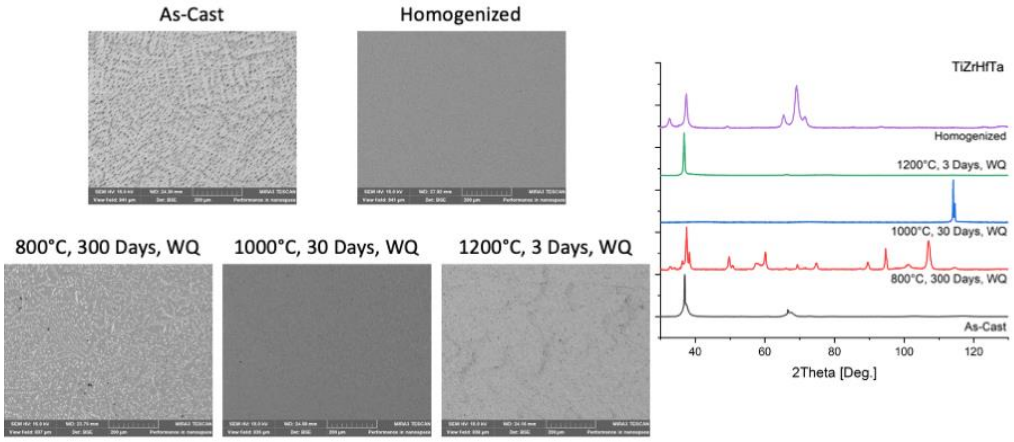

Ti-Zr-Nb-Ta

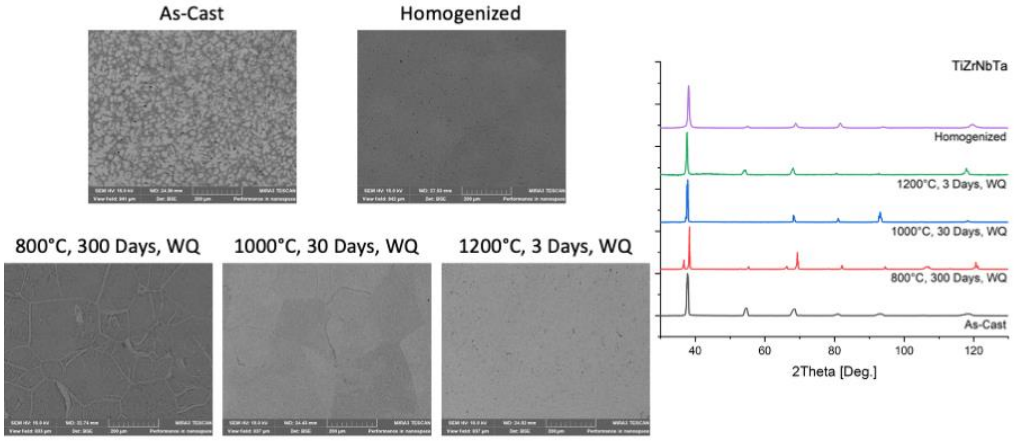

Ti-Nb-Hf-Ta

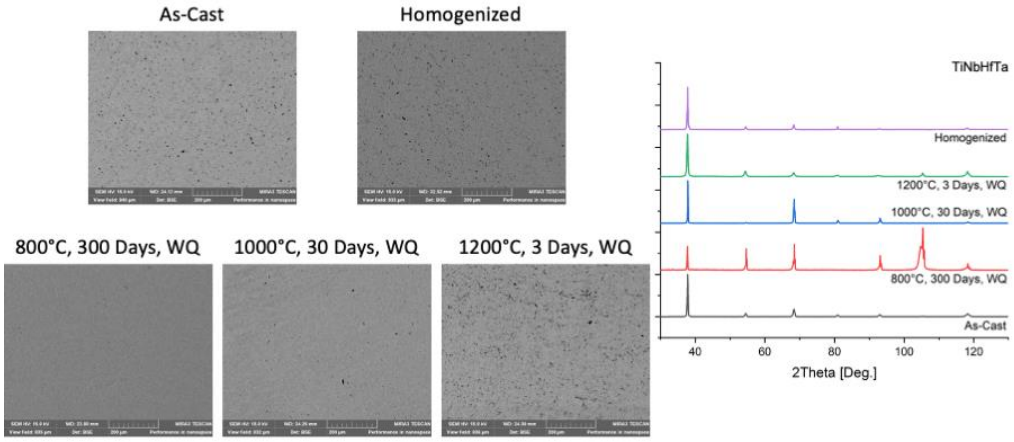

Zr-Nb-Hf-Ta

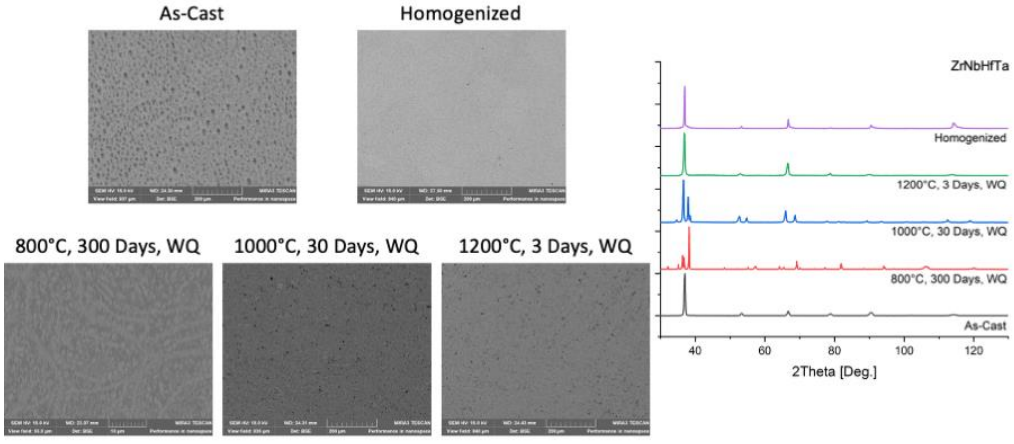

Ti-Zr-Hf

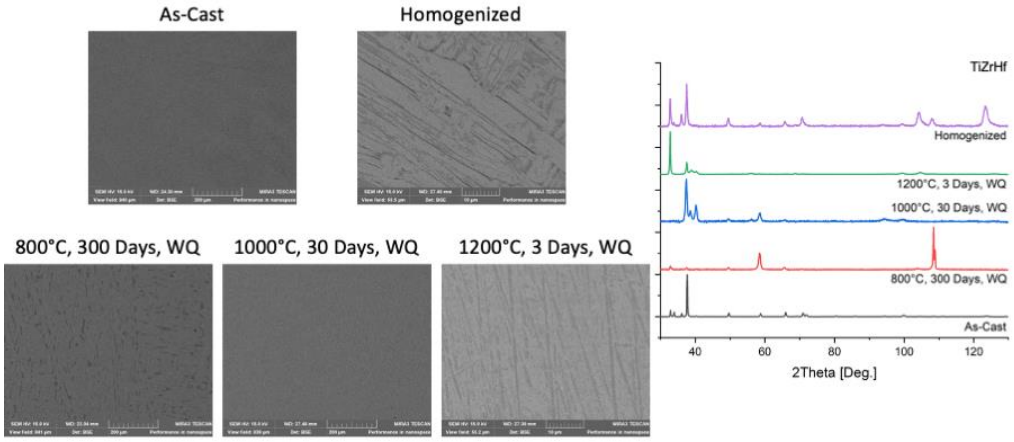

Ti-Zr-Nb

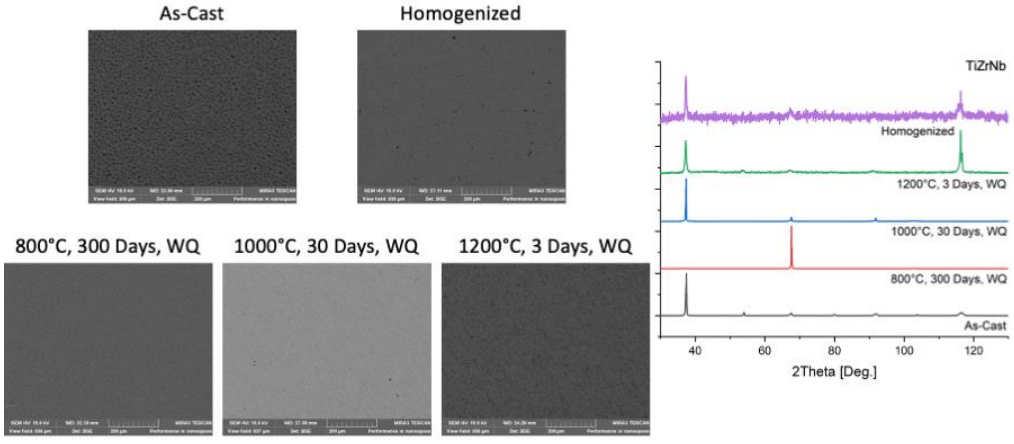

Ti-Zr-Ta

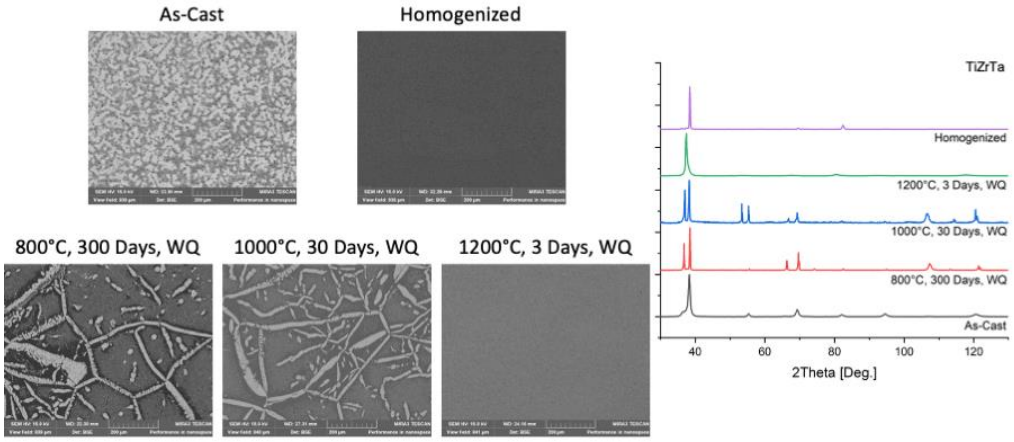

Ti-Hf-Nb

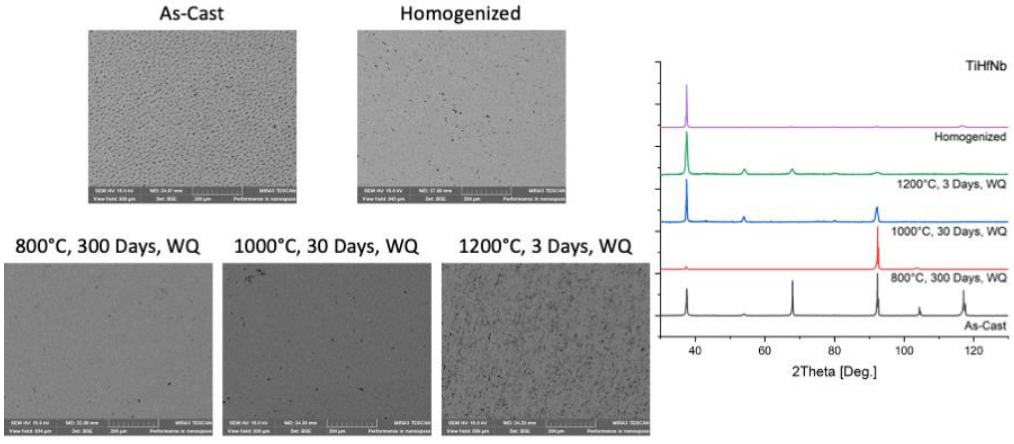

Ti-Hf-Ta

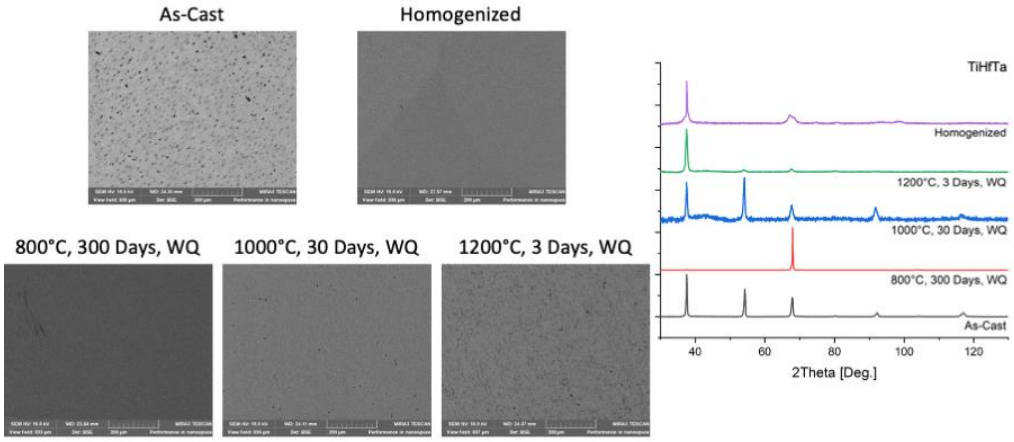

Ti-Nb-Ta

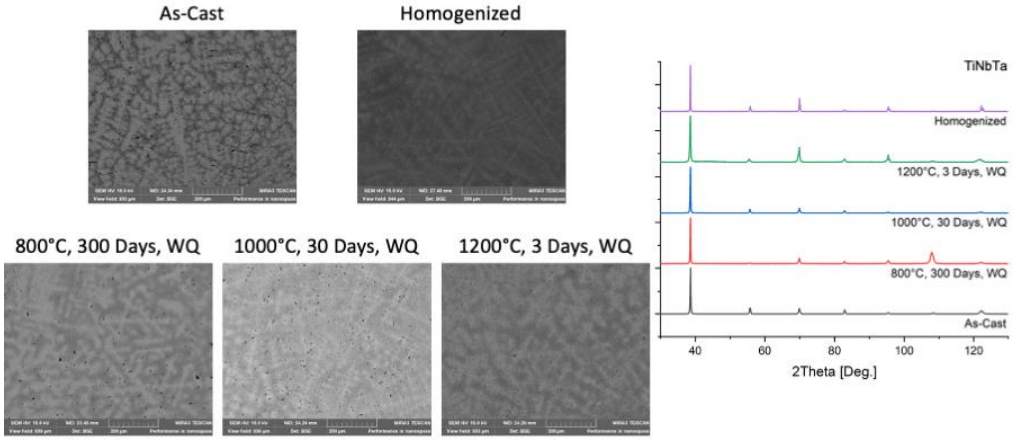

Zr-Hf-Nb

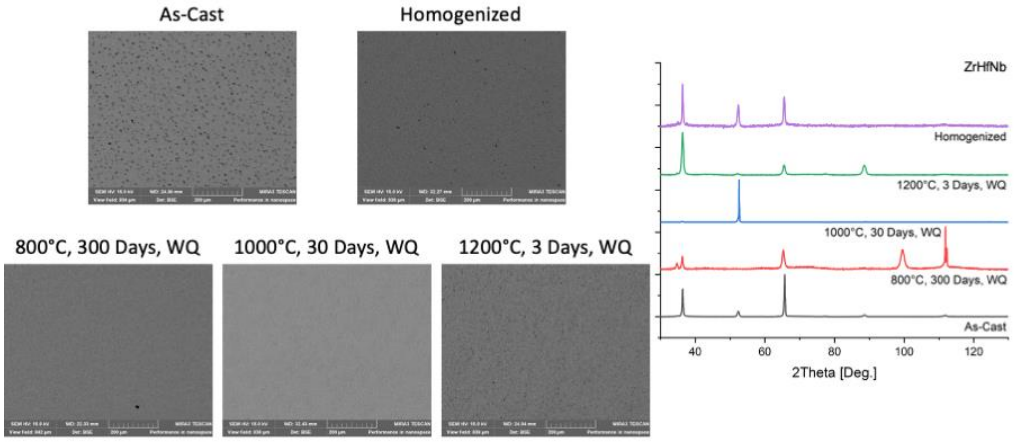

Zr-Hf-Ta

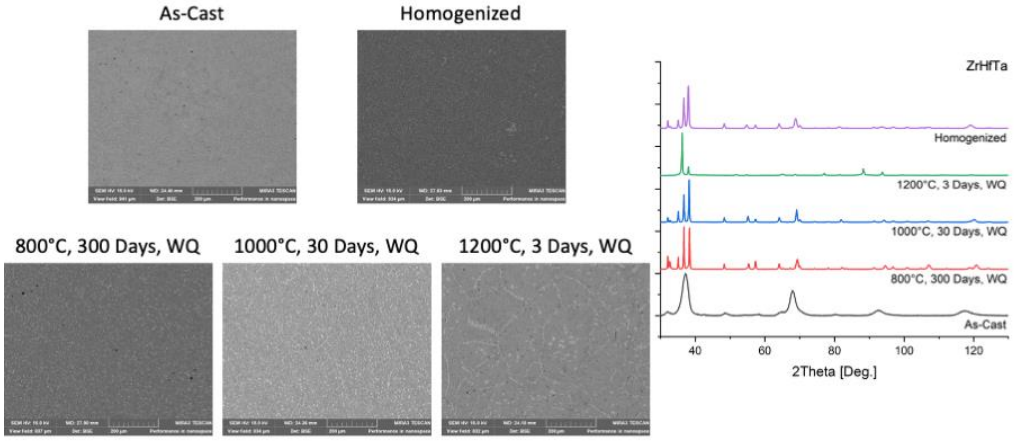

Zr-Nb-Ta

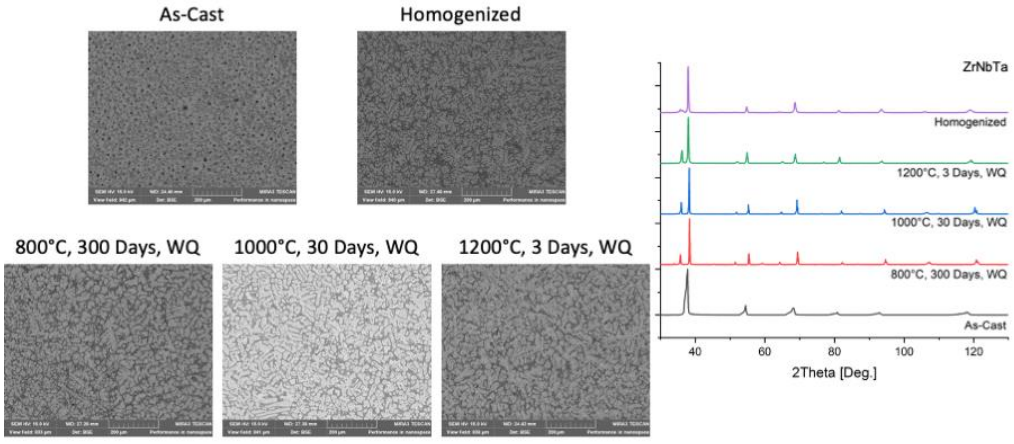

Hf-Nb-Ta

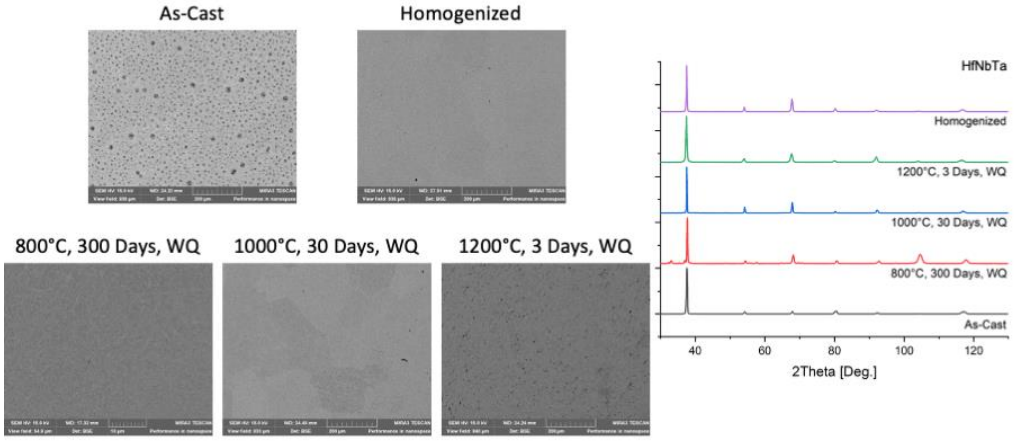

Ti-Zr

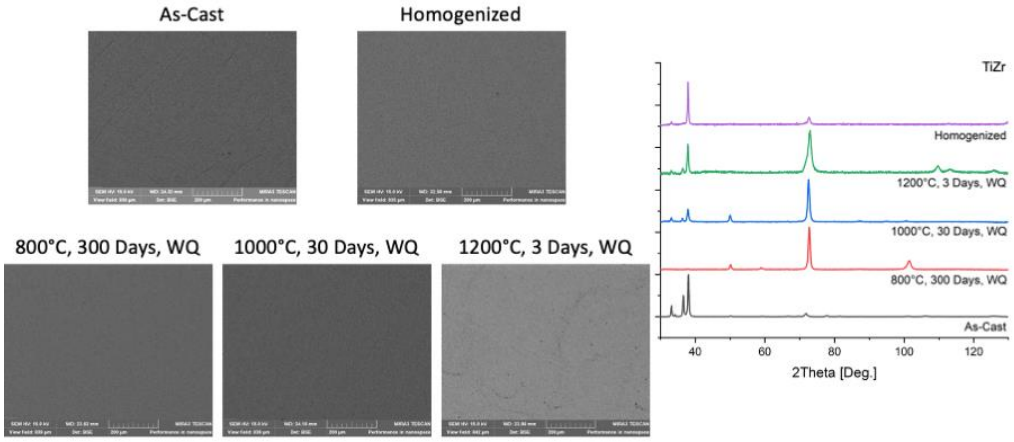
As-Cast
Homogenized
800°C, 300 Days, WQ
1000°C, 30 Days, WQ
1200°C, 3 Days, WQ
TiZr
Homogenized
1200°C, 3 Days, WQ
1000°C, 30 Days, WQ
800°C, 300 Days, WQ
As-Cast
40
60
80
100
120
2Theta [Deg.]

Ti-Hf

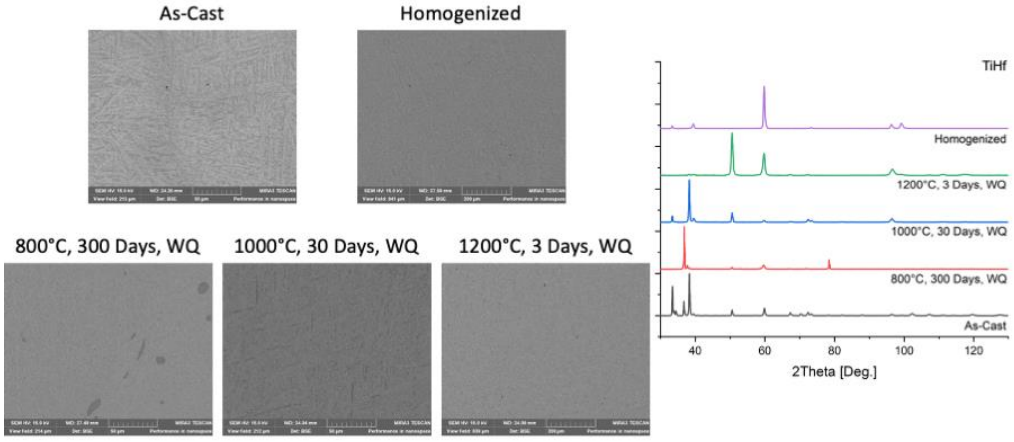
As-Cast
Homogenized
800°C, 300 Days, WQ
1000°C, 30 Days, WQ
1200°C, 3 Days, WQ
TiHf
Homogenized
1200°C, 3 Days, WQ
1000°C, 30 Days, WQ
800°C, 300 Days, WQ
As-Cast
40
60
80
100
120
2Theta [Deg.]

Ti-Nb

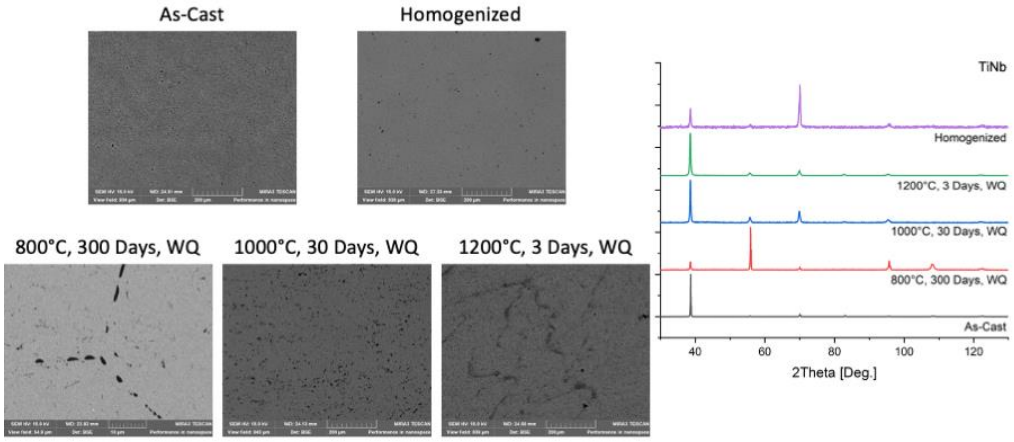
As-Cast
Homogenized
800°C, 300 Days, WQ
1000°C, 30 Days, WQ
1200°C, 3 Days, WQ
TiNb
Homogenized
1200°C, 3 Days, WQ
1000°C, 30 Days, WQ
800°C, 300 Days, WQ
As-Cast
40
60
80
100
120
2Theta [Deg.]

Ti-Ta

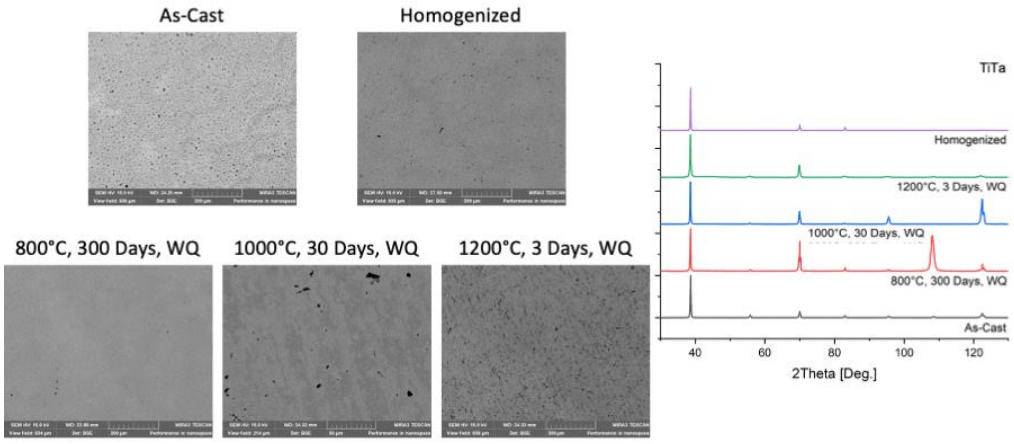
As-Cast
Homogenized
800°C, 300 Days, WQ
1000°C, 30 Days, WQ
1200°C, 3 Days, WQ
TiTa
Homogenized
1200°C, 3 Days, WQ
1000°C, 30 Days, WQ
800°C, 300 Days, WQ
As-Cast
40
60
80
100
120
2Theta [Deg.]

Zr-Hf

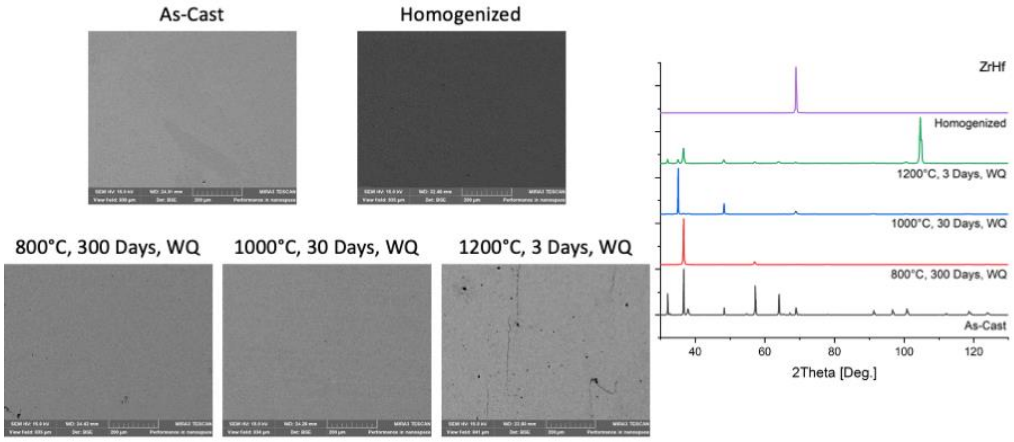
As-Cast
Homogenized
800°C, 300 Days, WQ
1000°C, 30 Days, WQ
1200°C, 3 Days, WQ
ZrHf
Homogenized
1200°C, 3 Days, WQ
1000°C, 30 Days, WQ
800°C, 300 Days, WQ
As-Cast
40
60
80
100
120
2Theta [Deg.]

Zr-Nb

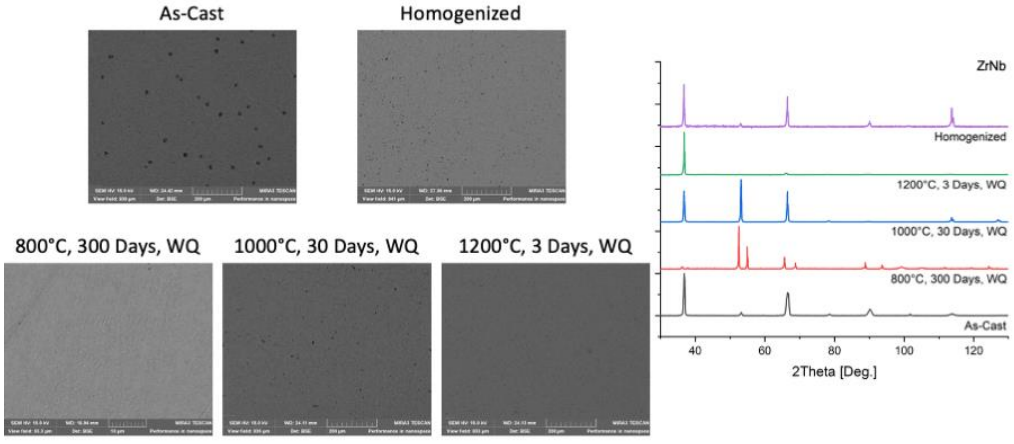
As-Cast
Homogenized
800°C, 300 Days, WQ
1000°C, 30 Days, WQ
1200°C, 3 Days, WQ
ZrNb
Homogenized
1200°C, 3 Days, WQ
1000°C, 30 Days, WQ
800°C, 300 Days, WQ
As-Cast
40
60
80
100
120
2Theta [Deg.]

Zr-Ta

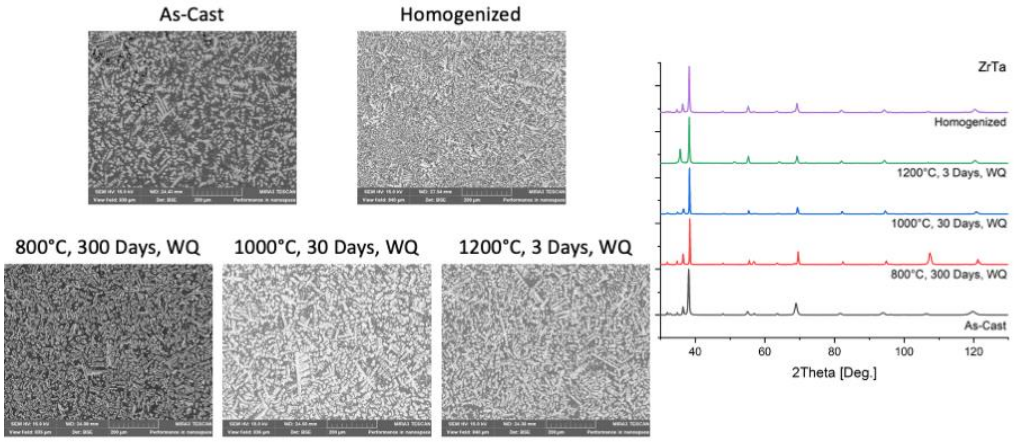
As-Cast
Homogenized
800°C, 300 Days, WQ
1000°C, 30 Days, WQ
1200°C, 3 Days, WQ
ZrTa
Homogenized
1200°C, 3 Days, WQ
1000°C, 30 Days, WQ
800°C, 300 Days, WQ
As-Cast
40
60
80
100
120
2Theta [Deg.]

Hf-Nb

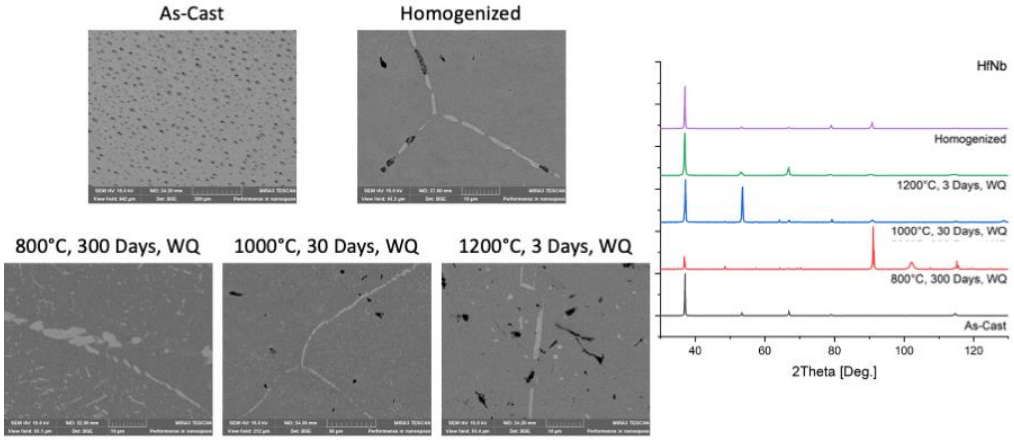
As-Cast
Homogenized
800°C, 300 Days, WQ
1000°C, 30 Days, WQ
1200°C, 3 Days, WQ
HfNb
Homogenized
1200°C, 3 Days, WQ
1000°C, 30 Days, WQ
800°C, 300 Days, WQ
As-Cast
40
60
80
100
120
2Theta [Deg.]

Hf-Ta

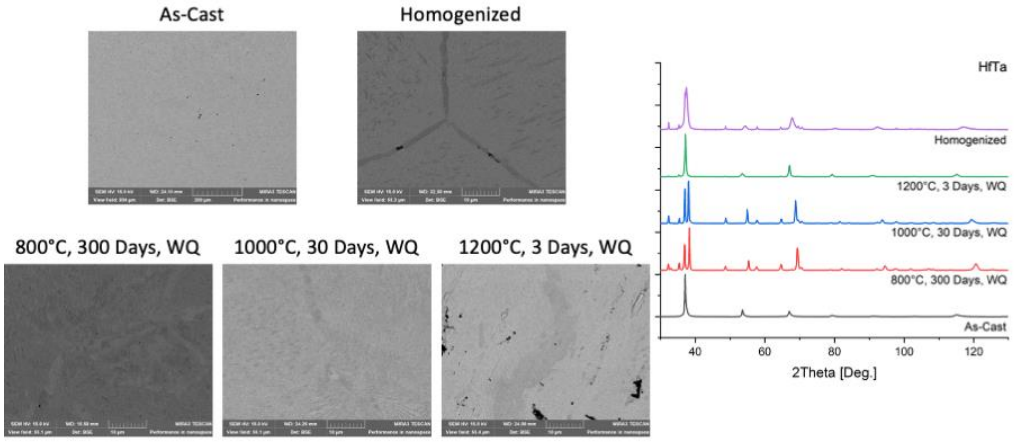
As-Cast
Homogenized
800°C, 300 Days, WQ
1000°C, 30 Days, WQ
1200°C, 3 Days, WQ
HfTa
Homogenized
1200°C, 3 Days, WQ
1000°C, 30 Days, WQ
800°C, 300 Days, WQ
As-Cast
40
60
80
100
120
2Theta [Deg.]

Nb-Ta

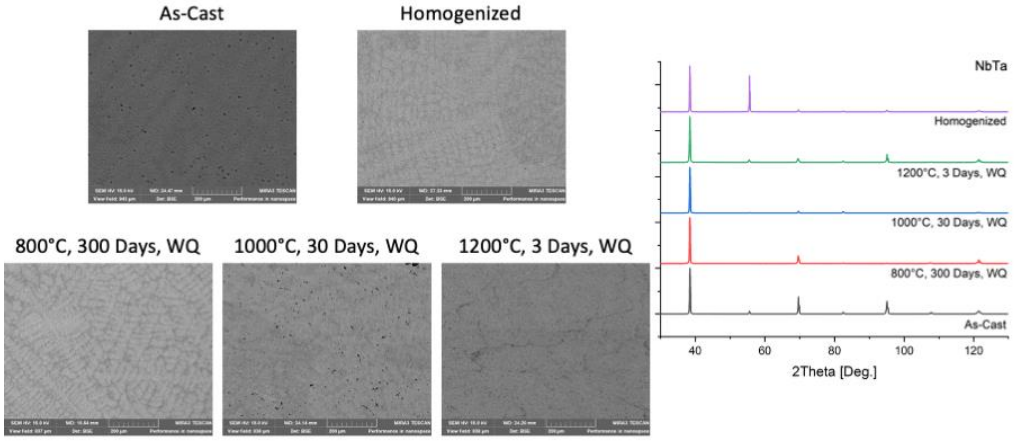
As-Cast
Homogenized
800°C, 300 Days, WQ
1000°C, 30 Days, WQ
1200°C, 3 Days, WQ
NbTa
Homogenized
1200°C, 3 Days, WQ
1000°C, 30 Days, WQ
800°C, 300 Days, WQ
As-Cast
40
60
80
100
120
2Theta [Deg.]

V-Nb-Mo-Ta-W

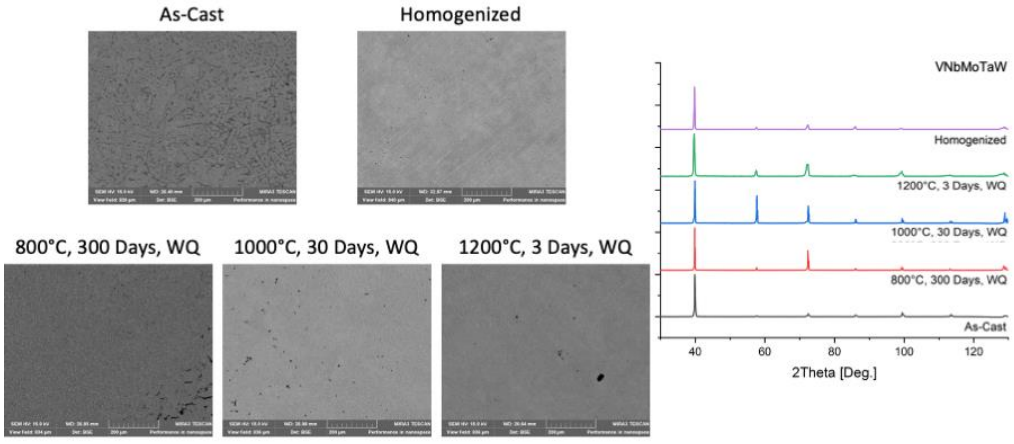

V-Nb-Mo-Ta

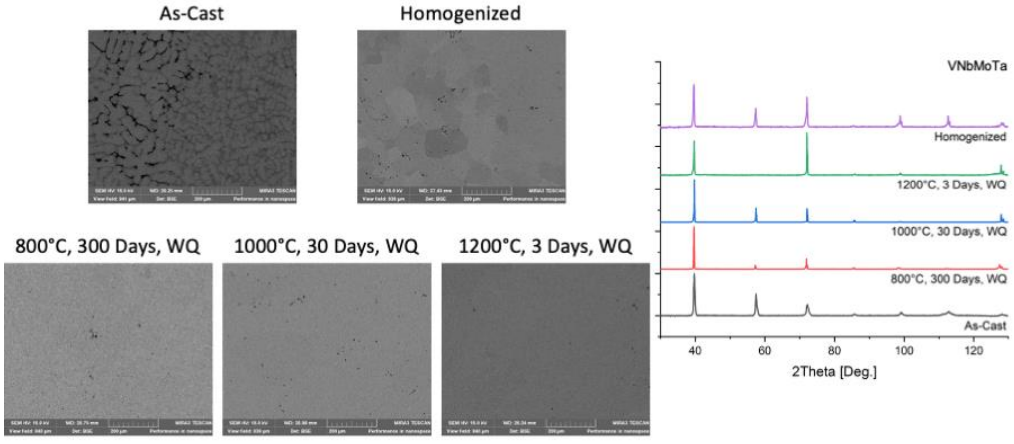

V-Nb-Mo-W

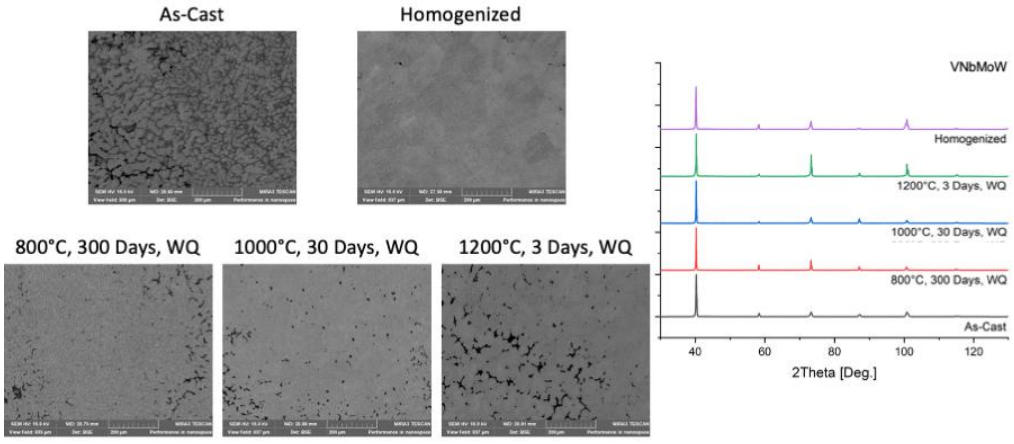

V-Nb-Ta-W

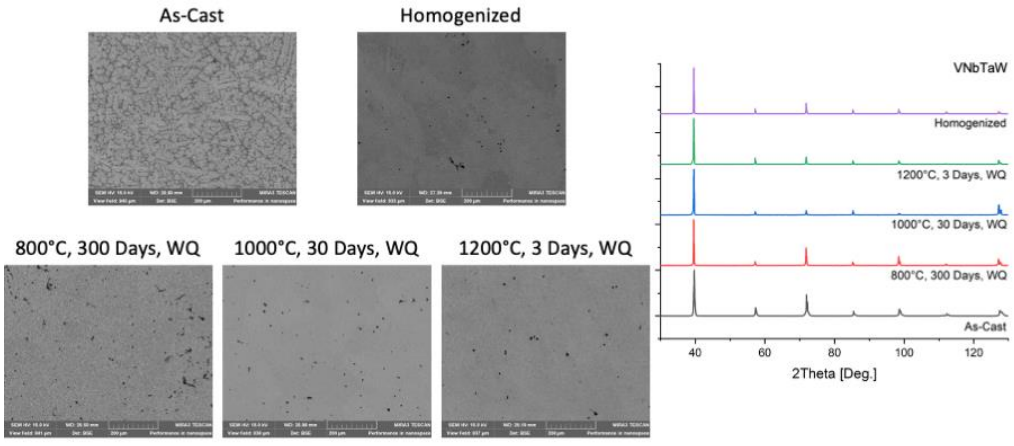

V-Mo-Ta-W

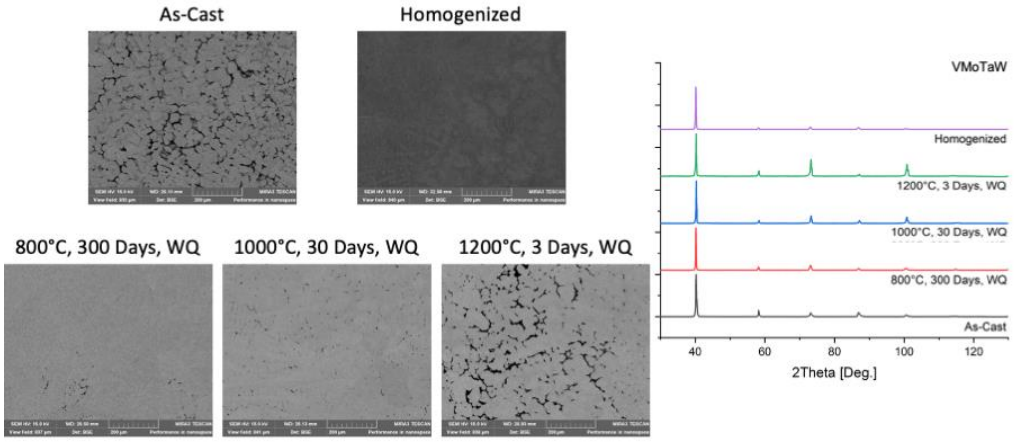

Nb-Mo-Ta-W

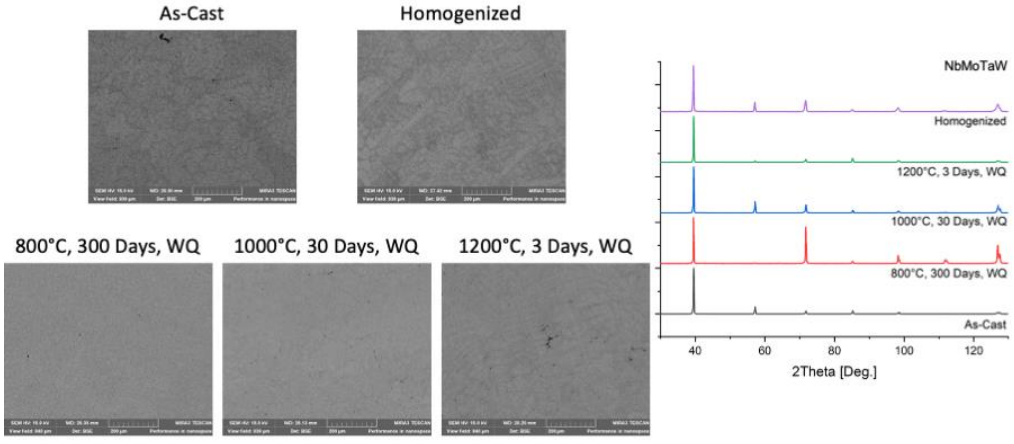

V-Nb-Mo

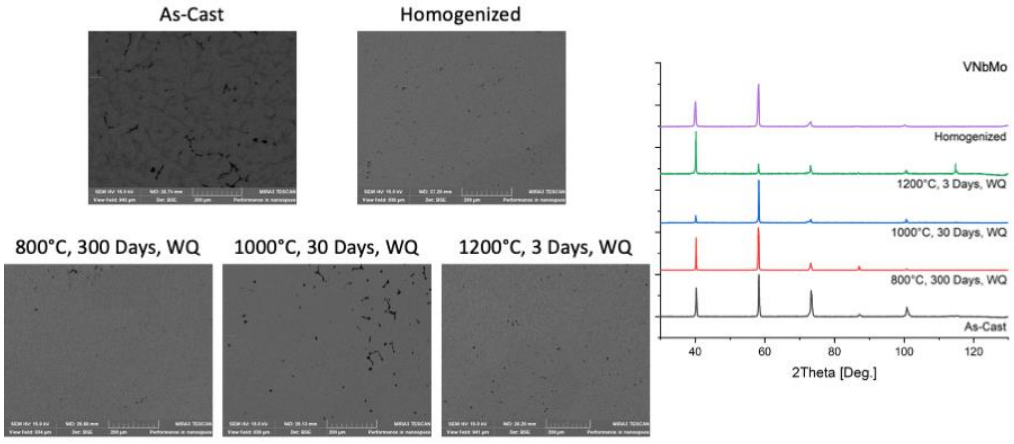
As-Cast
Homogenized
800°C, 300 Days, WQ
1000°C, 30 Days, WQ
1200°C, 3 Days, WQ
VNbMo
Homogenized
1200°C, 3 Days, WQ
1000°C, 30 Days, WQ
800°C, 300 Days, WQ
As-Cast
40
60
80
100
120
2Theta [Deg.]

V-Nb-Ta

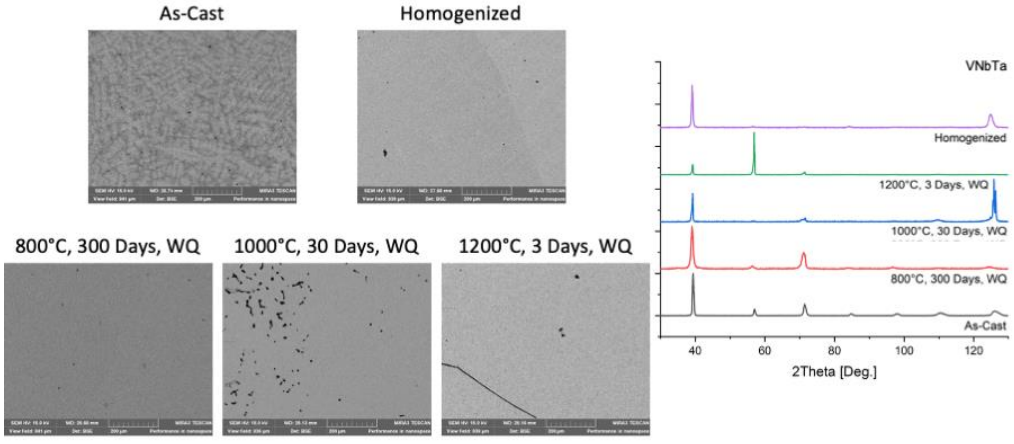
As-Cast
Homogenized
800°C, 300 Days, WQ
1000°C, 30 Days, WQ
1200°C, 3 Days, WQ
VNbTa
Homogenized
1200°C, 3 Days, WQ
1000°C, 30 Days, WQ
800°C, 300 Days, WQ
As-Cast
40
60
80
100
120
2Theta [Deg.]

V-Nb-W

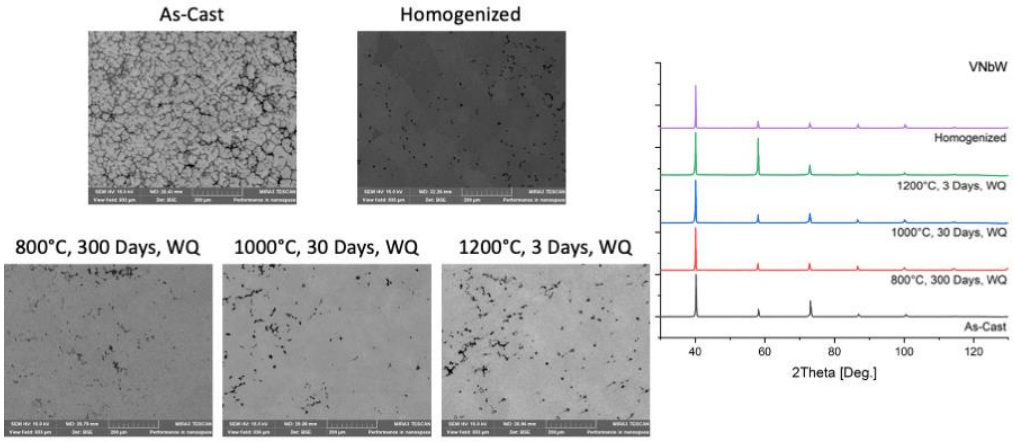
As-Cast
Homogenized
800°C, 300 Days, WQ
1000°C, 30 Days, WQ
1200°C, 3 Days, WQ
VNbW
Homogenized
1200°C, 3 Days, WQ
1000°C, 30 Days, WQ
800°C, 300 Days, WQ
As-Cast
40
60
80
100
120
2Theta [Deg.]

V-Mo-Ta

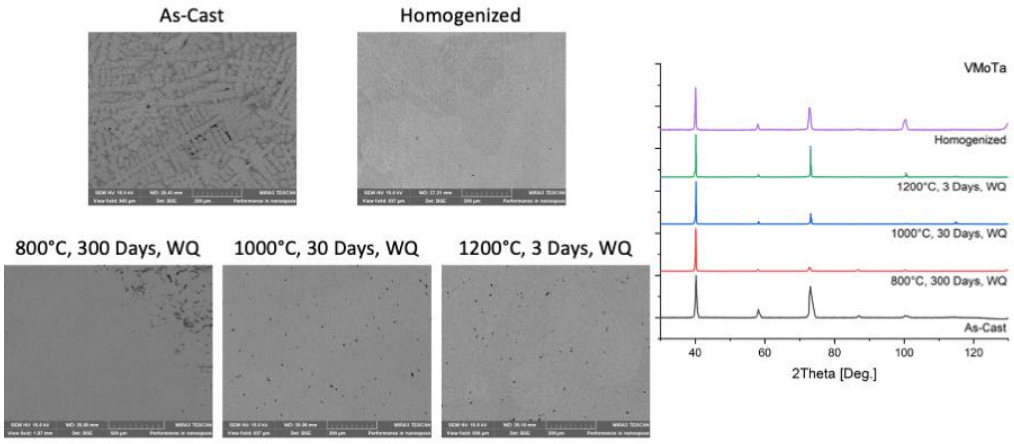
As-Cast
Homogenized
800°C, 300 Days, WQ
1000°C, 30 Days, WQ
1200°C, 3 Days, WQ
VMoTa
Homogenized
1200°C, 3 Days, WQ
1000°C, 30 Days, WQ
800°C, 300 Days, WQ
As-Cast
40
60
80
100
120
2Theta [Deg.]

V-Mo-W

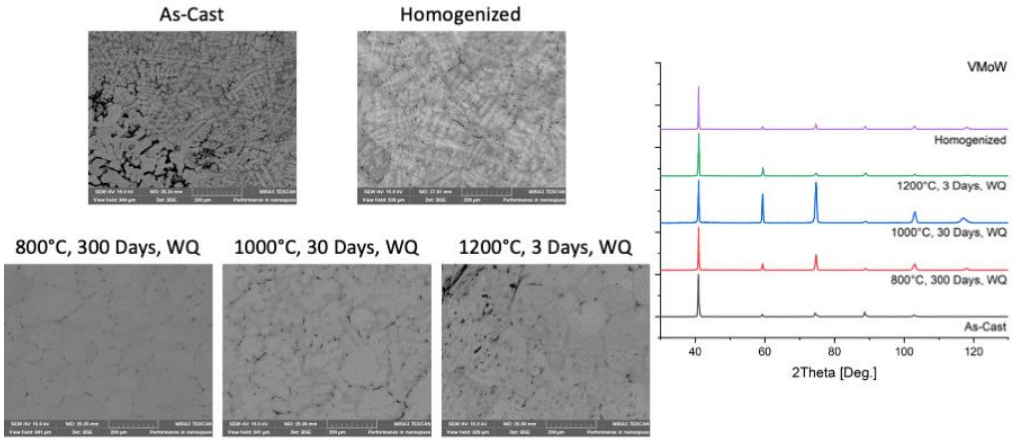
As-Cast
Homogenized
800°C, 300 Days, WQ
1000°C, 30 Days, WQ
1200°C, 3 Days, WQ
VMoW
Homogenized
1200°C, 3 Days, WQ
1000°C, 30 Days, WQ
800°C, 300 Days, WQ
As-Cast
40
60
80
100
120
2Theta [Deg.]

Nb-Mo-Ta

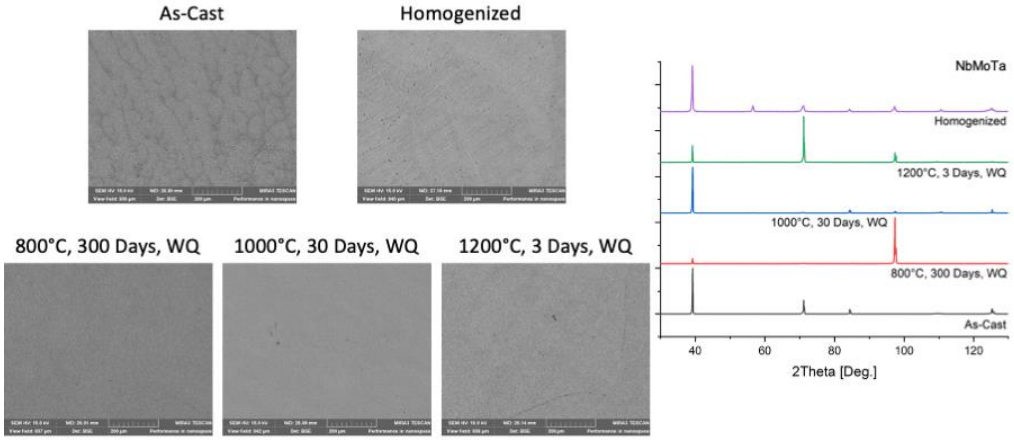
As-Cast
Homogenized
800°C, 300 Days, WQ
1000°C, 30 Days, WQ
1200°C, 3 Days, WQ
NbMoTa
Homogenized
1200°C, 3 Days, WQ
1000°C, 30 Days, WQ
800°C, 300 Days, WQ
As-Cast
40
60
80
100
120
2Theta [Deg.]

Nb-Mo-W

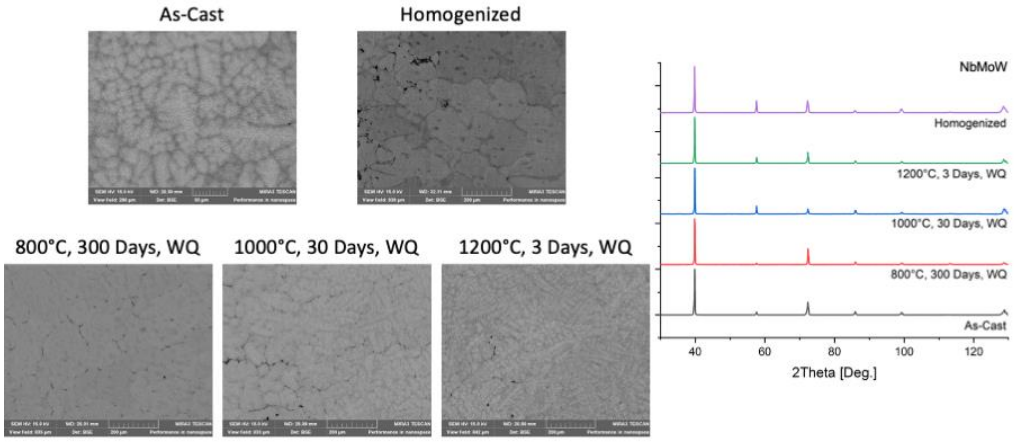
As-Cast
Homogenized
800°C, 300 Days, WQ
1000°C, 30 Days, WQ
1200°C, 3 Days, WQ
NbMoW
Homogenized
1200°C, 3 Days, WQ
1000°C, 30 Days, WQ
800°C, 300 Days, WQ
As-Cast
40
60
80
100
120
2Theta [Deg.]

Nb-Ta-W

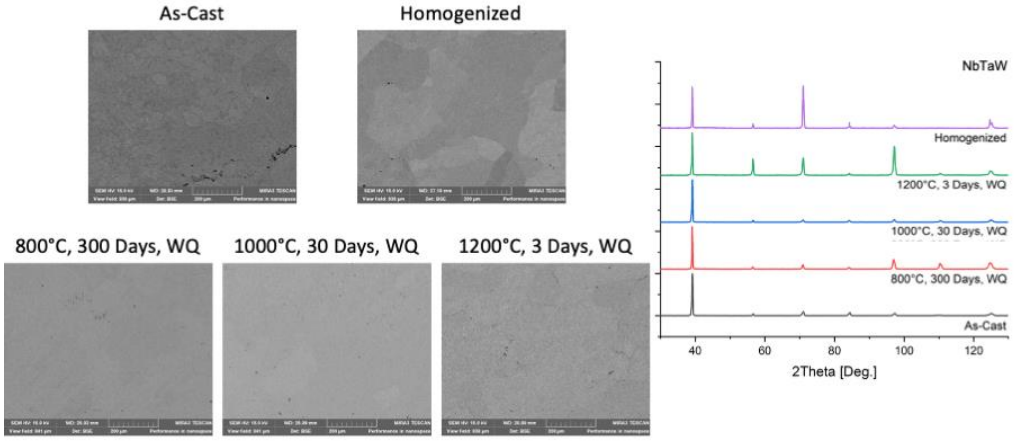
As-Cast
Homogenized
800°C, 300 Days, WQ
1000°C, 30 Days, WQ
1200°C, 3 Days, WQ
NbTaW
Homogenized
1200°C, 3 Days, WQ
1000°C, 30 Days, WQ
800°C, 300 Days, WQ
As-Cast
40
60
80
100
120
2Theta [Deg.]

Mo-Ta-W

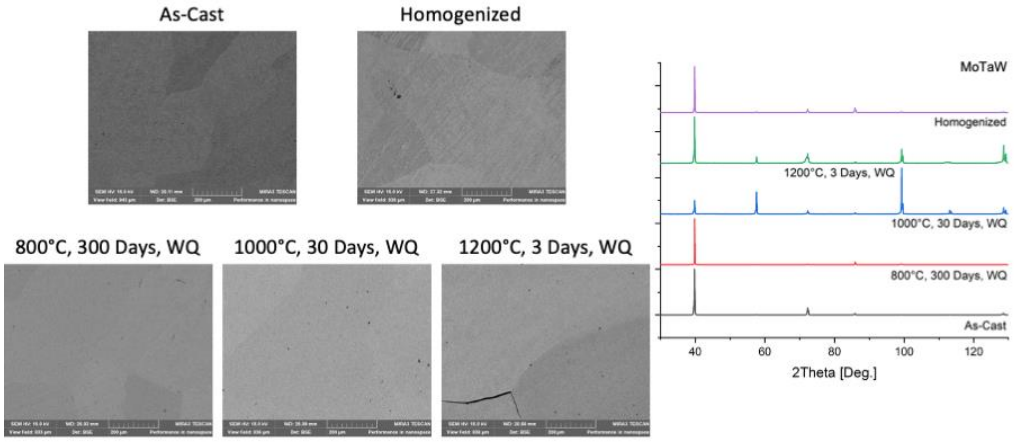
As-Cast
Homogenized
800°C, 300 Days, WQ
1000°C, 30 Days, WQ
1200°C, 3 Days, WQ
MoTaW
Homogenized
1200°C, 3 Days, WQ
1000°C, 30 Days, WQ
800°C, 300 Days, WQ
As-Cast
40
60
80
100
120
2Theta [Deg.]

V-Nb

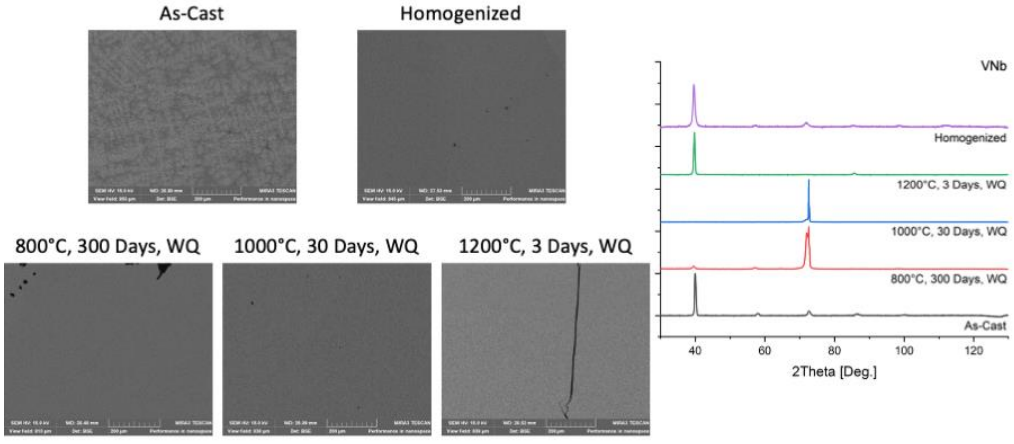
As-Cast
Homogenized
800°C, 300 Days, WQ
1000°C, 30 Days, WQ
1200°C, 3 Days, WQ
VNb
Homogenized
1200°C, 3 Days, WQ
1000°C, 30 Days, WQ
800°C, 300 Days, WQ
As-Cast
40
60
80
100
120
2Theta [Deg.]

V-Mo

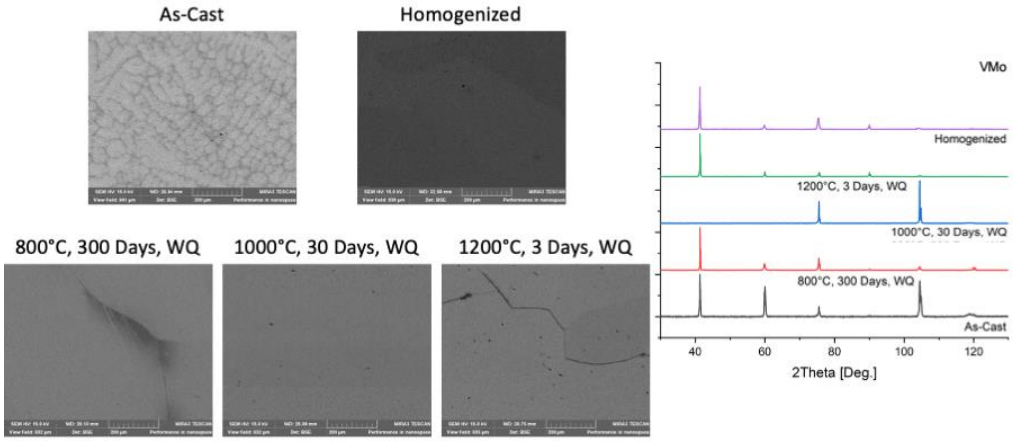
As-Cast
Homogenized
800°C, 300 Days, WQ
1000°C, 30 Days, WQ
1200°C, 3 Days, WQ
VMo
Homogenized
1200°C, 3 Days, WQ
1000°C, 30 Days, WQ
800°C, 300 Days, WQ
As-Cast
40
60
80
100
120
2Theta [Deg.]

V-Ta

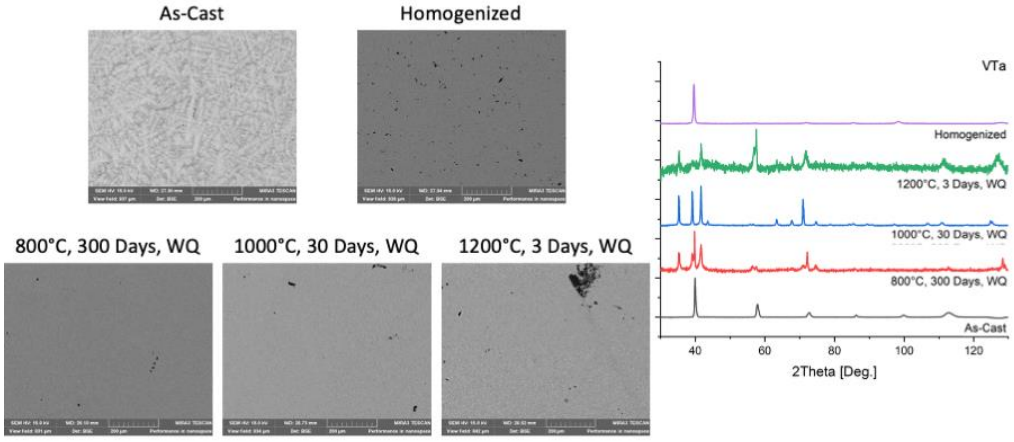
As-Cast
Homogenized
800°C, 300 Days, WQ
1000°C, 30 Days, WQ
1200°C, 3 Days, WQ
VTa
Homogenized
1200°C, 3 Days, WQ
1000°C, 30 Days, WQ
800°C, 300 Days, WQ
As-Cast
40
60
80
100
120
2Theta [Deg.]

V-W

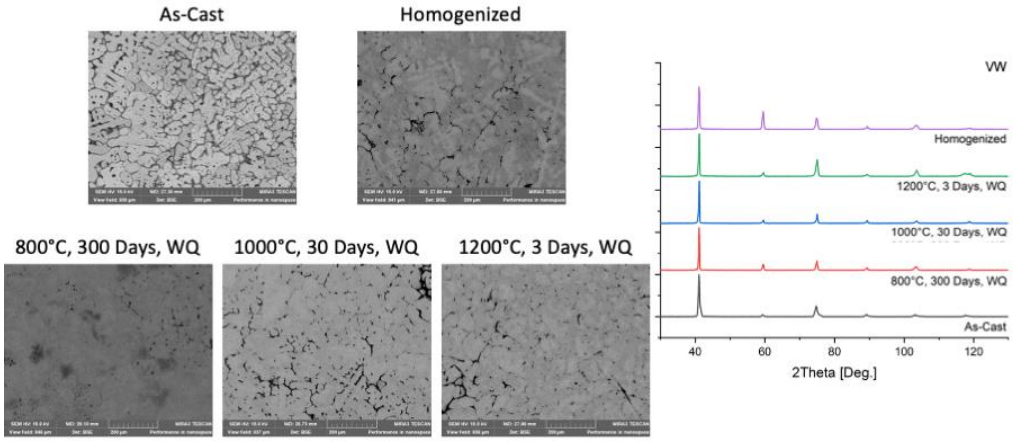
As-Cast
Homogenized
800°C, 300 Days, WQ
1000°C, 30 Days, WQ
1200°C, 3 Days, WQ
VW
Homogenized
1200°C, 3 Days, WQ
1000°C, 30 Days, WQ
800°C, 300 Days, WQ
As-Cast
40
60
80
100
120
2Theta [Deg.]

Nb-Mo

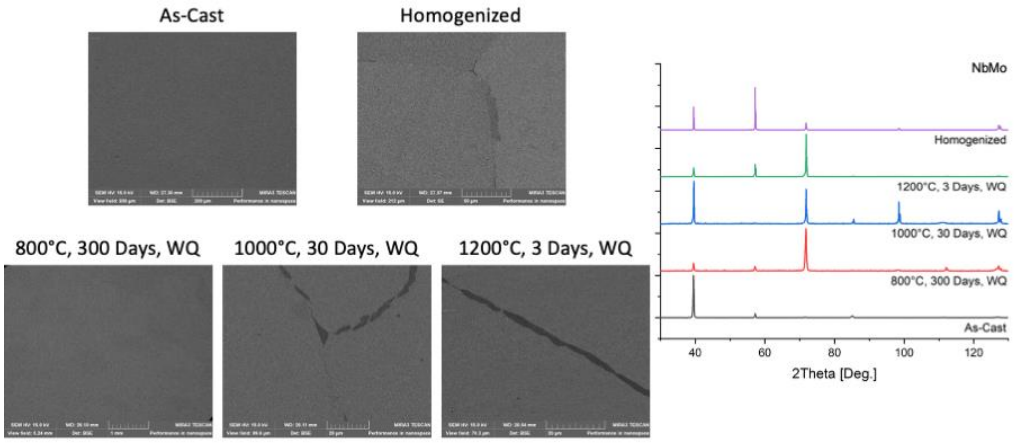
As-Cast
Homogenized
800°C, 300 Days, WQ
1000°C, 30 Days, WQ
1200°C, 3 Days, WQ
NbMo
Homogenized
1200°C, 3 Days, WQ
1000°C, 30 Days, WQ
800°C, 300 Days, WQ
As-Cast
40
60
80
100
120
2Theta [Deg.]

Nb-Ta

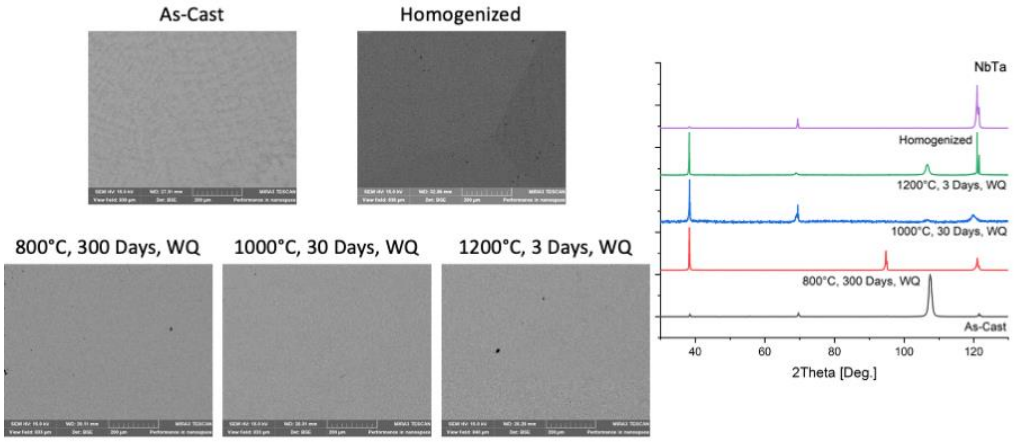
As-Cast
Homogenized
800°C, 300 Days, WQ
1000°C, 30 Days, WQ
1200°C, 3 Days, WQ
NbTa
Homogenized
1200°C, 3 Days, WQ
1000°C, 30 Days, WQ
800°C, 300 Days, WQ
As-Cast
40
60
80
100
120
2Theta [Deg.]

Nb-W

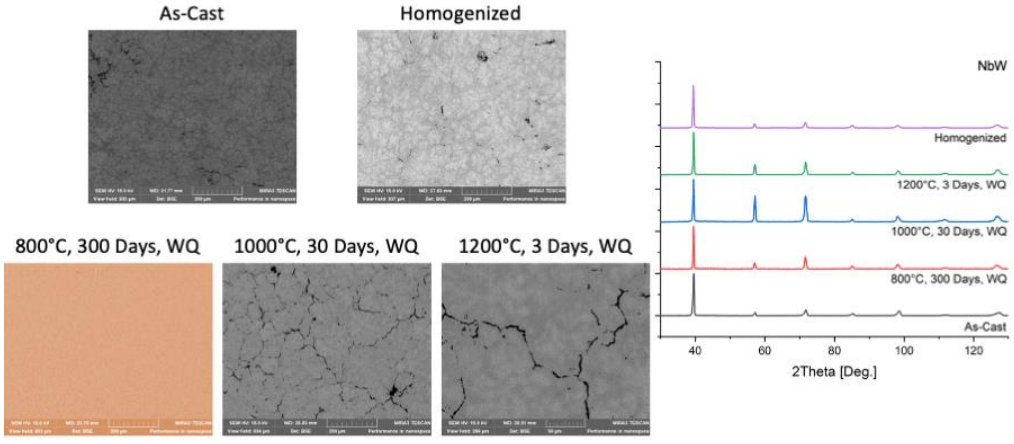
As-Cast
Homogenized
800°C, 300 Days, WQ
1000°C, 30 Days, WQ
1200°C, 3 Days, WQ
NbW
Homogenized
1200°C, 3 Days, WQ
1000°C, 30 Days, WQ
800°C, 300 Days, WQ
As-Cast
40
60
80
100
120
2Theta [Deg.]

Mo-Ta

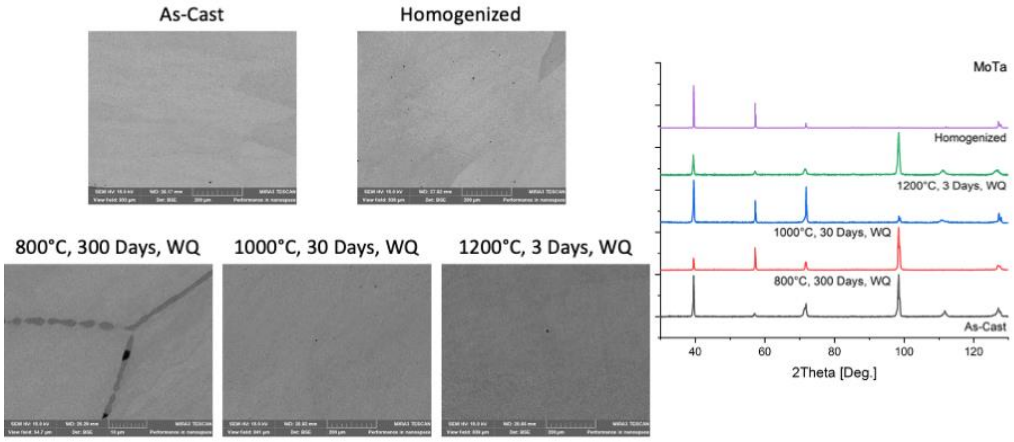
As-Cast
Homogenized
800°C, 300 Days, WQ
1000°C, 30 Days, WQ
1200°C, 3 Days, WQ
MoTa
Homogenized
1200°C, 3 Days, WQ
1000°C, 30 Days, WQ
800°C, 300 Days, WQ
As-Cast
40
60
80
100
120
2Theta [Deg.]

Mo-W

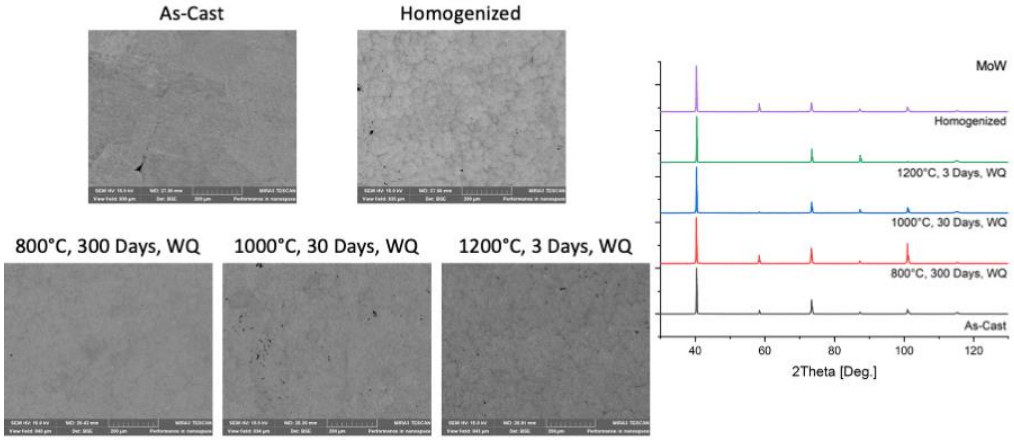
As-Cast
Homogenized
800°C, 300 Days, WQ
1000°C, 30 Days, WQ
1200°C, 3 Days, WQ
MoW
Homogenized
1200°C, 3 Days, WQ
1000°C, 30 Days, WQ
800°C, 300 Days, WQ
As-Cast
40
60
80
100
120
2Theta [Deg.]

Ta-W

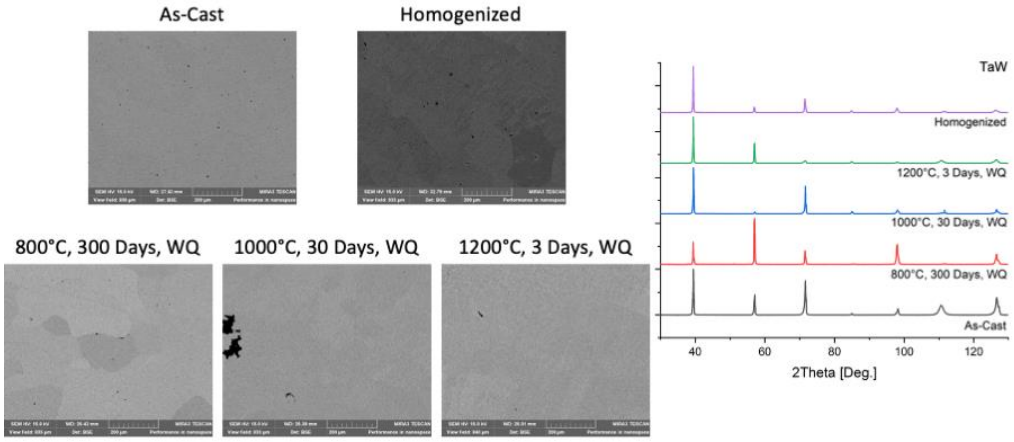
As-Cast
Homogenized
800°C, 300 Days, WQ
1000°C, 30 Days, WQ
1200°C, 3 Days, WQ
TaW
Homogenized
1200°C, 3 Days, WQ
1000°C, 30 Days, WQ
800°C, 300 Days, WQ
As-Cast
40
60
80
100
120
2Theta [Deg.]

Vita

Originally from the Midwest, Jeffrey M. Brookins grew up in Dearborn Heights, MI. After high school, he attended Michigan Technological University for two years before enlisting in the United States Marine Corps, from 2010 to 2013; deploying twice to Afghanistan. After returning to Michigan Technological University, he received a Bachelor of Science degree in Materials Science and Engineering in 2017 and was awarded a Master of Science degree in 2018 for a thesis focusing on the usage of zinc as a bioabsorable implant material. Following this, he moved south to the University of Tennessee, Knoxville, to purse a Doctor of Philosophy degree in Materials Science and Engineering. His research interests are focused on the fundamentals of physical metallurgy, using high entropy alloys as model systems, and the characterization of proposed alloys at non-ambient temperatures. After graduation, he intends to continue his research interests as a post-doctoral researcher, while continuing to mentor and guide other students, in an effort to pay back all the work that others have put into him.